

## N O T I C E

THIS DOCUMENT HAS BEEN REPRODUCED FROM  
MICROFICHE. ALTHOUGH IT IS RECOGNIZED THAT  
CERTAIN PORTIONS ARE ILLEGIBLE, IT IS BEING RELEASED  
IN THE INTEREST OF MAKING AVAILABLE AS MUCH  
INFORMATION AS POSSIBLE



The Ohio State University

GTD ANALYSIS OF AIRBORNE ANTENNAS  
RADIATING IN THE PRESENCE OF  
LOSSY DIELECTRIC LAYERS

R.G. Rojas-Teran  
and  
W.D. Burnside



The Ohio State University  
**ElectroScience Laboratory**

Department of Electrical Engineering  
Columbus, Ohio 43212

Semi-Annual Report 710964-8  
Contract NSG 1498  
August 1981

(NASA-CR-168770) GTD ANALYSIS OF AIRBORNE  
ANTENNAS RADIATING IN THE PRESENCE OF LOSSY  
DIELECTRIC LAYERS Semiannual Report (Ohio  
State Univ., Columbus.) 113 p HC A66/MF A01

N82-22398

Unclass  
CSCL 20N G3/32 09595

National Aeronautics and Space Administration  
Langley Research Center  
Hampton, Virginia 23665

<b>REPORT DOCUMENTATION PAGE</b>		1. REPORT NO.	2.	3. Recipient's Accession No.
4. Title and Subtitle GTD ANALYSIS OF AIRBORNE ANTENNAS RADIATING IN THE PRESENCE OF LOSSY DIELECTRIC LAYERS		5. Report Date August 1981		
7. Author(s) R.G. Rojas-Teran and W.D. Burnside		8. Performing Organization Rept. No. ESL 710964-8		
9. Performing Organization Name and Address The Ohio State University ElectroScience Laboratory Department of Electrical Engineering Columbus, Ohio 43212		10. Project/Task/Work Unit No.		
12. Sponsoring Organization Name and Address National Aeronautics and Space Administration Langley Research Center Hampton, Virginia 23665		11. Contract(G) or Grant(G) No. (C) NSG 1498 (G)		
15. Supplementary Notes		13. Type of Report & Period Covered Semi-Annual Report		
16. Abstract (Limit: 200 words) A method for computing the patterns of monopole or aperture antennas mounted on a perfectly conducting convex surface radiating in the presence of a dielectric or metal plate is presented. The Geometrical Theory of Diffraction (GTD) is used to analyze the radiating system and extended here to include diffraction by flat dielectric slabs. Modified edge diffraction coefficients valid for wedges whose walls are lossy or lossless thin dielectric or perfectly-conducting plates are developed. The width of the dielectric plates cannot exceed a quarter of a wavelength in free space, and the interior angle of the wedge is assumed to be close to 0° or 180°. Systematic methods for computing the individual components of the total high-frequency field are discussed. The accuracy of the solutions is demonstrated by comparisons with measured results, where a $2\lambda \times 4\lambda$ prolate spheroid is used as the convex surface. It is observed that a jump or kink appears in the calculated pattern when higher order terms that are important are not included in the final solution. The most immediate application of the results presented here is in the modelling of structures such as aircraft which are composed of non-metallic parts that play a significant role in the pattern.				
17. Document Analysis a. Descriptors				
b. Identifiers/Open-Ended Terms				
c. COSATI Field/Group				
18. Availability Statement		19. Security Class (This Report) Unclassified		21. No. of Pages 110
		20. Security Class (This Page) Unclassified		22. Price

PRECEDING PAGE BLANK NOT FILMED

TABLE OF CONTENTS

	Page
I. INTRODUCTION	1
II. GEOMETRICAL OPTICS FIELD	4
A. Reflection and Transmission	7
B. Reflection Coefficient of Dielectric Slab	11
C. Transmission Coefficient of Dielectric Slab	15
III. TWO DIMENSIONAL 'EDGE' DIFFRACTED FIELD	18
A. Scalar Diffraction Coefficients for a Perfectly-Conducting Wedge	24
B. Distance Parameters	25
C. Scalar Diffraction Coefficients for a Dielectric-Dielectric/Metal Junction	27
IV. THREE DIMENSIONAL SLAB SCATTERING	36
A. Ray-Fixed Coordinate System	36
B. Edge-Fixed Coordinate System	36
C. Dyadic Reflection Coefficient	38
D. Dyadic Transmission Coefficient	40
E. Dyadic Diffraction Coefficient	41
V. CURVED SURFACE DIFFRACTION	47
A. Lit Region	47
B. Shadow Region	54
VI. RADIATION PATTERN OF AN ANTENNA MOUNTED ON A CONVEX BODY IN THE PRESENCE OF A DIELECTRIC SLAB	60
A. Pattern Factors	62
B. Source Field	64
C. Reflected Field	65
D. Edge-Diffracted Field	65
VII. RESULTS	69
VIII. SUMMARY AND CONCLUSIONS	107
REFERENCES	109

## CHAPTER I

### INTRODUCTION

There exists a great deal of interest in calculating the radiation patterns of airborne antennas and other complicated radiating structures. One of the approaches that has found great success for analyzing these types of problems is the Geometrical Theory of Diffraction (GTD).

One of the biggest advantages of this method over others is that complex structures can be modelled using much simpler structures. These simpler structures can be analyzed using the results given in Chapters Two through Five. To be able to obtain an accurate radiation pattern, one must take into account the scattering structures. Thus, GTD also provides a means of identifying the significant contributions from the complex structures in the resulting antenna pattern.

The scattering and diffraction by objects which are large in terms of wavelengths is essentially a local phenomenon associated with specific parts of the object. GTD, which is a high-frequency approach, is applied and extended here to include diffraction by flat dielectric slabs.

The GTD method originally developed by Keller and his associates at the Courant Institute of Mathematical Sciences [1,2,3] fails in the transition regions adjacent to the shadow and reflection boundaries. For that reason, many people did not see the importance of this method for many years. The GTD is an extension of Geometrical Optics that can be justified by the generalized Fermat's principle, which is introduced in Chapter Three.

The Uniform (GTD), developed at The Ohio State University, provides expressions for the diffracted field such that the total high-frequency field is uniformly continuous across all transition boundaries. Expressions have been developed for electromagnetic fields diffracted from edges and vertices in perfectly conducting surfaces due to sources either on or off perfectly conducting convex surfaces.

The problem of interest in this thesis is the radiation of an antenna mounted on a perfectly conducting convex surface in the presence of a  $m$ -sided, finite dielectric plate, as illustrated in Figure 1, where  $m=4$ .

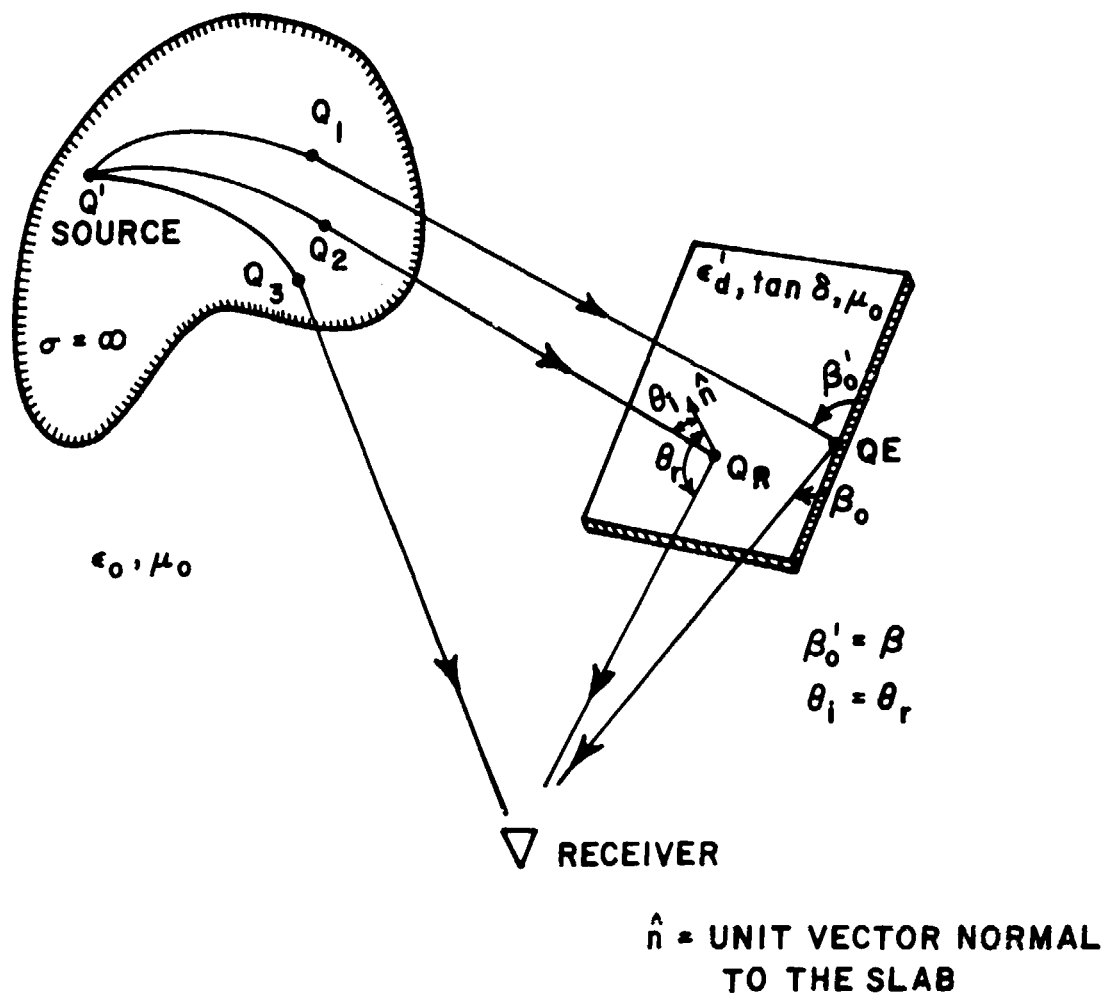


Figure 1. Curved surface mounted antenna radiating in the presence of a thin dielectric plate.

It is assumed here that the plate will not be attached to the convex surface. The total field at the point (p) may be expressed as

$$\bar{E}^{\text{tot}} = \bar{E}^i u^i + \bar{E}^r u^r + \bar{E}^t u^t + \bar{E}^d, \quad (1)$$

where  $\bar{E}^i$  is the source field,  $\bar{E}^r$  is the reflected field from the plate,  $\bar{E}^t$  is the transmitted field, and  $\bar{E}^d$  is the total edge diffracted field. The functions  $u^i$ ,  $u^r$ , and  $u^t$  are unit step functions included in Equation (1) to emphasize the discontinuities in the geometrical optics (G.O.) solution. Note that  $\bar{E}^i$  represents the direct source field or the curved surface diffracted field.

Chapter Six discusses a systematic way of computing the individual terms of Equation (1), and thus obtaining the total field by superimposing all the individual field components. The geometrical optics solutions, the transmission, and reflection coefficients for lossy dielectric slabs, which are needed in order to calculate the total field are discussed in Chapter Two. The modified edge diffraction coefficients valid for wedges whose walls are lossy or lossless dielectric or perfectly-conducting plates are presented in Chapters Three and Four. It is assumed that the interior angle of the wedge is either close to  $0^\circ$  or  $180^\circ$ , and the width of the dielectric plates is less than a quarter of a wavelength in free space. Chapter Five briefly discusses surface diffracted rays from arbitrary convex surfaces. Analytic and measured results for the radiation pattern of an antenna mounted on a spheroid are discussed in Chapter Seven. Finally, Chapter Eight is a summary of all the results presented here.

## CHAPTER II

### GEOMETRICAL OPTICS FIELD

The geometrical optics field is the leading term in the asymptotic high frequency solution of Maxwell's equations, and it is also the leading term in the GTD and UTD high-frequency approximations. The G.O. field is equal to the sum of the leading terms in the incident and reflected fields as shown in [4]. Their fields can be expanded in a Luneberg-Kline series for large  $\omega$  of the form [4]

$$\bar{E} \sim \exp(-jk\psi) \sum_{m=0}^{\infty} \frac{\bar{E}_m}{(j\omega)^m}, \quad (2)$$

where  $k$  is the wavenumber of the medium, and an  $\exp(j\omega t)$  time dependence is assumed and suppressed. The leading term of Equation (2) is given by [5]

$$\bar{E}(s) \sim \exp[-jk\psi(s)] \bar{E}_0(s) = \bar{E}_0(0) \exp[-jk\psi(0)] \sqrt{\frac{\rho_1 \rho_2}{(\rho_1+s)(\rho_2+s)}} \exp(-jks), \quad (3)$$

where  $s=0$  is the reference point on the ray path, and  $\rho_1, \rho_2$  are the principal radii of curvature of the wavefront at  $s=0$  as shown in Figure 2.

Equation (3) is known as the geometric-optics field. The leading term in the Luneberg-Kline asymptotic expansion takes into account the polarization and wave nature of the electromagnetic field, which is not the case in classical geometrical optics. At  $s=-\rho_1, -\rho_2$ , Equation (3) becomes infinite, so the solution fails at the caustics. As one passes through a caustic in the direction of propagation, the sign of  $\rho+s$  changes and the correct phase shift of  $\pi/2$  can be introduced.

From  $\nabla \cdot \bar{E} = 0$ , one obtains [4]

$$\hat{s} \cdot \bar{E}_0 = 0, \quad (4)$$



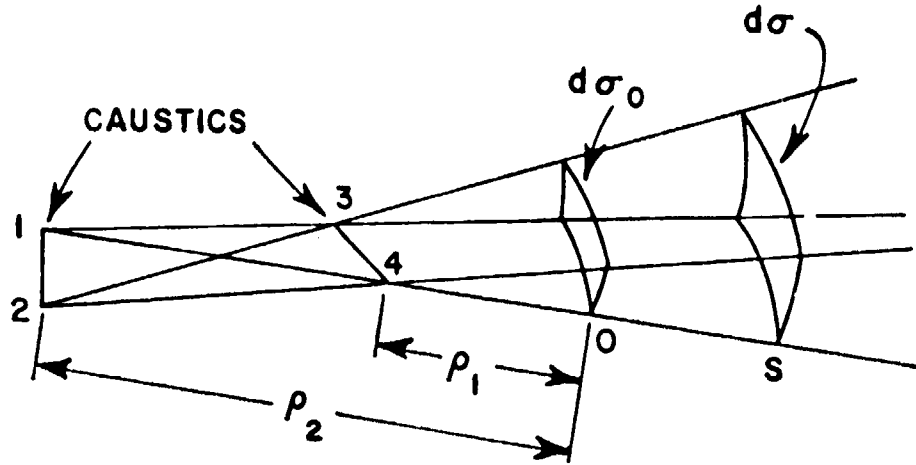


Figure 2. Astigmatic tube of rays.

where  $\hat{s}$  is the unit vector in the direction of the ray path. This equation indicates that the electric vector of the geometrical optics field is orthogonal to the direction of propagation. Using  $\nabla \times \vec{E} = -j\omega\mu\vec{H}$ , one obtains an expression for  $\vec{H}$  of the form

$$\vec{H} \sim Y_c \hat{s} \times \vec{E} \quad (5)$$

where  $Y_c = \sqrt{\frac{\epsilon}{\mu}}$ .

In order to calculate the reflected field, consider the geometry of Figure 3, where the incident field is a high-frequency electromagnetic field, and  $S$  a smooth curved perfectly conducting surface. Using the boundary conditions for the total electric field on  $S$ , the following expression for  $\vec{E}_r$  is obtained

$$\vec{E}^r(o) = \vec{E}_o^r(o) \exp[-jk\psi^r(o)] = \vec{E}^i(Q_R) \cdot \vec{R} = \vec{E}^i(Q_R) \cdot [\hat{e}_{||}^i \hat{e}_{||}^r - \hat{e}_{\perp}^i \hat{e}_{\perp}^r], \quad (6)$$

where  $Q_R$  is the reflecting point,  $\vec{R}$  the dyadic reflection coefficient and  $\vec{E}^i(Q_R)$  the incident electric field at  $Q_R$ . The unit vectors  $\hat{e}_{||}^i$ ,  $\hat{e}_{||}^r$ , and  $\hat{e}_{\perp}^i$  will be defined more carefully in Chapter Four. Combining Equations (3) and (6)

$$\vec{E}^r(s) = \vec{E}^i(Q_R) \cdot \vec{R} \sqrt{\frac{\rho_1^r \rho_2^r}{(\rho_1^r + s)(\rho_2^r + s)}} \exp(-jks), \quad (7)$$

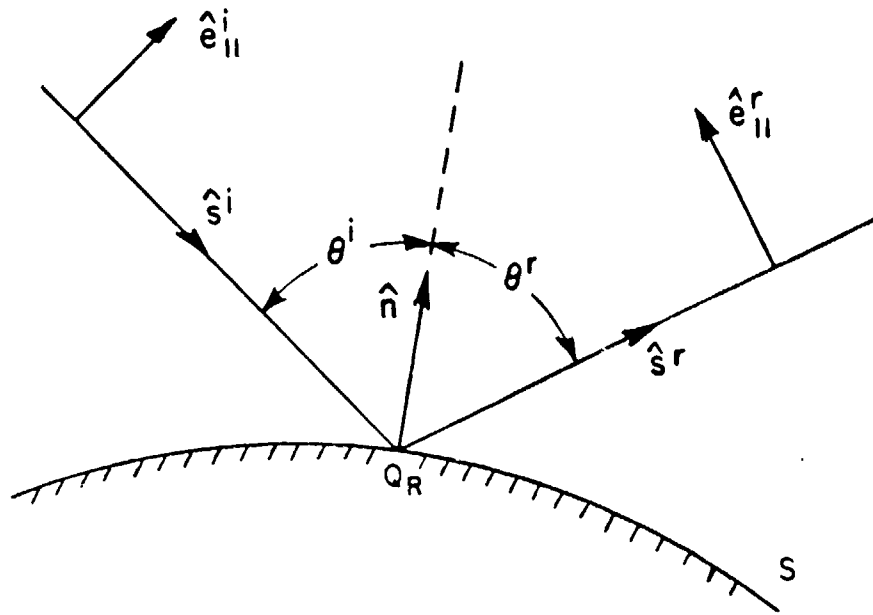


Figure 3. Geometry depicting the reflection by a curved surface S.

where  $\rho_1^r, \rho_2^r$  are the principal radii of curvature of the reflected wavefront at  $Q_R$ .

It can be shown that

$$\hat{s}^i \cdot \hat{n} = \hat{s}^r \cdot \hat{n} \quad (8)$$

This equation leads to the famous Law of Reflection. That is, the reflected ray lies on the plane of incidence, and the angle of reflection  $\theta_r$  is equal to the angle of incidence  $\theta_i$ , where both angles are measured from the unit normal  $\hat{n}$  as shown in Figure 3. The plane of incidence is the plane formed by the incident ray and the normal to the surface at the point of incidence. It is shown in [4] that:

$$\frac{1}{\rho_1^r} = \frac{1}{2} \left( \frac{1}{\rho_1^i} + \frac{1}{\rho_1^i} \right) + f_1 \quad (9)$$

$$\frac{1}{\rho_2^r} = \frac{1}{2} \left( \frac{1}{\rho_1^i} + \frac{1}{\rho_2^i} \right) + f_2 \quad (10)$$

Expressions for  $f_1$  and  $f_2$  are given in [6]. For the special case of an incident spherical wave

$$\frac{1}{f_2} = \frac{1}{\cos \theta_i} \left( \frac{\sin^2 \theta_2}{R_1} + \frac{\sin^2 \theta_1}{R_2} \right) + \sqrt{\frac{1}{\cos^2 \theta_i} \left( \frac{\sin^2 \theta_2}{R_1} + \frac{\sin^2 \theta_1}{R_2} \right)^2 - \frac{4}{R_1 R_2}} \quad (11)$$

where  $\theta_1, \theta_2$  are the angles between  $\hat{s}^i$  and the principal directions associated with the principal radii of curvature of the surface  $R_1, R_2$ , respectively. This is illustrated in Figure 4. Expressions for the principal directions and the principal radii of curvature of the reflected field for an arbitrary incident field are given in [7].

#### A. Reflection and Transmission

It is obvious that the reflection and transmission coefficients for the slab shown in Figure 1 have to be calculated in order to obtain the reflected, transmitted, and diffracted fields. The slab can be a lossy or lossless dielectric, or a perfectly-conducting plate. The two dimensional (2-D) case will be considered first, and later in Chapter Four the expressions for the 2-D case are generalized to the more general 3-D case, after a suitable coordinate system is defined.

Consider the 2-D geometry illustrated in Figure 5, where  $\bar{s}^i$  refers to the incident ray,  $\bar{s}^r$  to the reflected ray, and  $\bar{s}^t$  to the transmitted ray.

Medium #1 is assumed to be lossless, i.e.,  $\epsilon_1 = \epsilon'_1$ ,  $\mu_1 = \mu'_1$ ,  $\sigma_1 = 0$ , and  $\epsilon''_1 = \mu''_1 = 0$ , and medium #2 is a lossy medium, but it is assumed that this loss is due to  $\epsilon''_2$  and  $\sigma_2$  only. Thus  $\sigma_2 = \sigma + i\omega \epsilon''_2$  and  $\mu_2 = \mu'_2$ ,  $\mu''_2 = 0$ , and  $\epsilon_2 = \epsilon'_2$ .

In order to find the reflection and transmission coefficients for the boundary shown in Figure 5, the boundary conditions on  $\vec{H}$  and  $\vec{E}$  have to be satisfied. That is, assuming there are no sources at the boundary, one obtains

$$\left[ \vec{E}^{(1)} - \vec{E}^{(2)} \right] \times \hat{n} = 0 \quad \hat{n} \times \left[ \vec{H}^{(1)} - \vec{H}^{(2)} \right] = 0. \quad (12)$$

Applying the above equations to the case of perpendicular polarization (E-field perpendicular to the z-y plane) one can directly obtain the following expressions

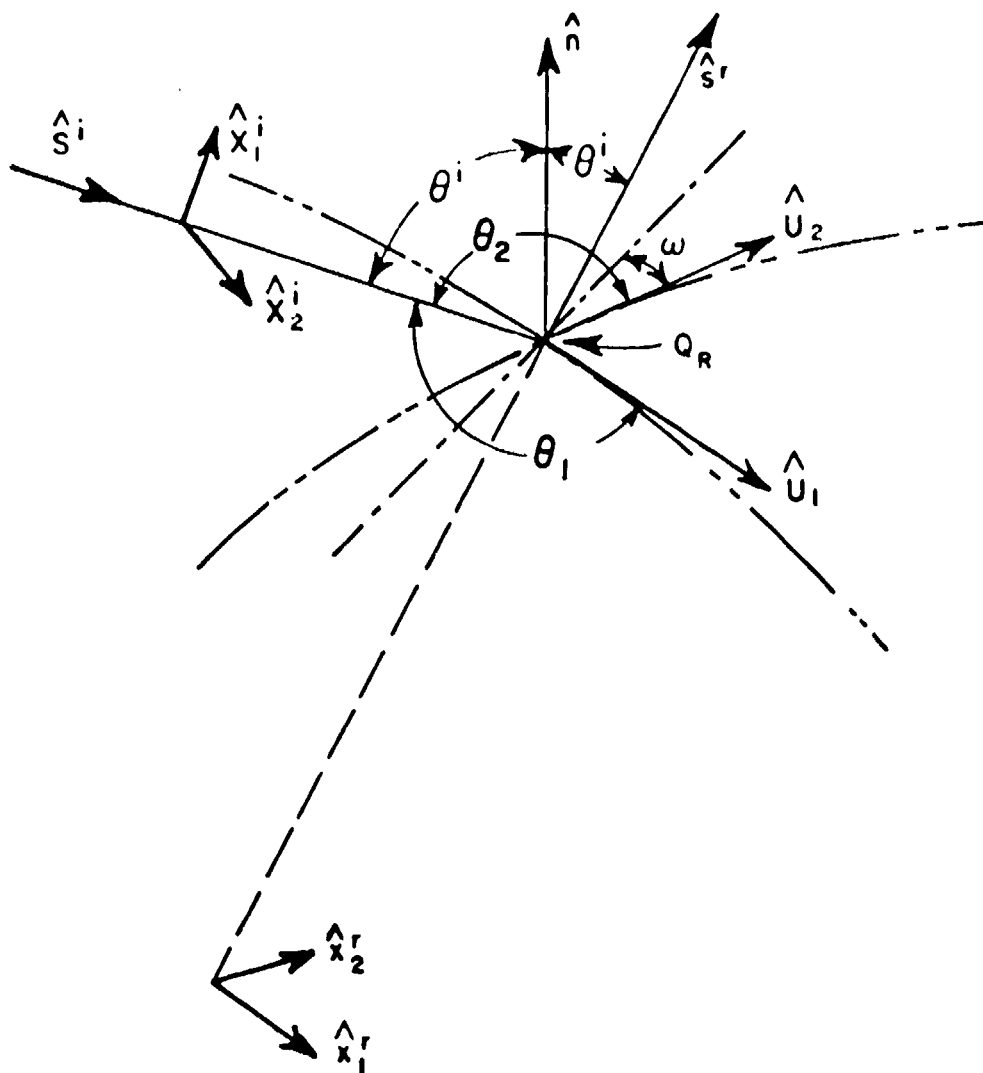


Figure 4. Geometry for the analysis of the reflected wavefront. The reflecting surface is S.

- — — — — Intersection of a principal plane of S at  $Q_R$  with S
- — — — — Intersection of the plane of incidence with the plane tangent to S at  $Q_R$
- — — — — Extension of the reflected ray below S.

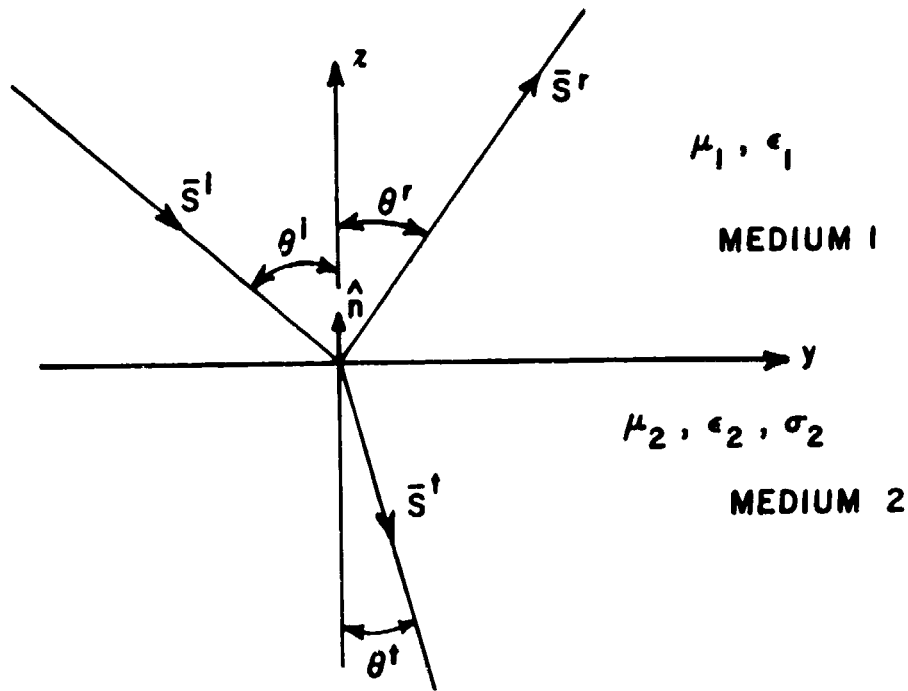


Figure 5. Geometry in the plane of incidence (z-y plane) for a wave at oblique incidence.

$$R_1 = \frac{\omega\mu_2 \cos\theta_i - (\beta \cos\theta_t - j\alpha)\eta_1}{\omega\mu_2 \cos\theta_i + (\beta \cos\theta_t - j\alpha)\eta_1} \quad (13)$$

and

$$T_1 = 1 + R_1 = \frac{2\omega\mu_2 \cos\theta_i}{\omega\mu_2 \cos\theta_i + (\beta \cos\theta_t - j\alpha)\eta_1} \quad (14)$$

where

$$k_1 = \omega\sqrt{\mu_1\epsilon_1} \quad k_2 = \omega\sqrt{\mu_2\epsilon_2} \quad (15)$$

$$\alpha = \frac{\omega\mu_2 \sigma_2}{2\sqrt{\beta^2 - k_1^2} \sin^2\theta_i} \quad \eta_1 = \sqrt{\frac{\mu_1}{\epsilon_1}} \quad (16)$$

$$\beta^2 = \frac{(k_2^2 + k_1^2 \sin^2 \theta^i) + \sqrt{(k_2^2 - k_1^2 \sin^2 \theta^i)^2 + (\omega \mu_2 \sigma_2)^2}}{2} \quad (17)$$

thus one can express  $E_1^r$  and  $E_1^t$  at the boundary ( $z=0$ ) as

$$E_1^r(z=0^+) = R_1 E_1^i(z=0^+) \quad E_1^t(z=0^-) = T_1 E_1^i(z=0^+) \quad (18)$$

For a lossless, nonmagnetic medium, i.e.,  $\sigma_2=0$ ,  $\beta=k_2$ , and  $\mu_1=\mu_2=\mu_0$  one obtains

$$R_1 = \frac{\cos \theta^i - (\epsilon_2/\epsilon_1 - \sin^2 \theta^i)^{1/2}}{\cos \theta^i + (\epsilon_2/\epsilon_1 - \sin^2 \theta^i)^{1/2}}, \text{ and} \quad (19)$$

$$T_1 = \frac{2 \cos \theta^i}{\cos \theta^i + (\epsilon_2/\epsilon_1 - \sin^2 \theta^i)^{1/2}} \quad (20)$$

In order to express  $\cos \theta^t$  in terms of  $\sin \theta^i$ , one has to use Snell's law for the lossless, nonmagnetic case

$$\sin \theta^t = \sqrt{\frac{\mu_1 \epsilon_1}{\mu_2 \epsilon_2}} \sin \theta^i = \sqrt{\frac{\epsilon_1}{\epsilon_2}} \sin \theta^i \quad (21)$$

The expressions for the other polarization (H-field perpendicular to the z-y plane) are

$$R_{\parallel} = \frac{\epsilon_2/\epsilon_1 \cos \theta^i (1 - j \tan \delta) - (\beta' \cos \theta^t - j\alpha/k_1)}{\epsilon_2/\epsilon_1 \cos \theta^i (1 - j \tan \delta) + (\beta' \cos \theta^t - j\alpha/k_1)}, \quad (22)$$

$$T_{\parallel} = 1 + R_{\parallel} = \frac{2\epsilon_2/\epsilon_1 \cos \theta^i (1 - j \tan \delta)}{\epsilon_2/\epsilon_1 \cos \theta^i (1 - j \tan \delta) + (\beta' \cos \theta^t - j\alpha/k_1)}, \quad (23)$$

where

$$\tan \delta = \frac{\sigma_2}{\omega \epsilon_2}, \text{ and } \beta' = \beta/k_1. \quad (24)$$

For a lossless, nonmagnetic medium, i.e.,  $\sigma_2=0$ ,  $\mu_1=\mu_2=\mu_0$ ,  $\beta^2=\epsilon_2/\epsilon_1$  one arrives once again to the familiar expressions

$$R_{\parallel} = \frac{\epsilon_2/\epsilon_1 \cos \theta^i - (\epsilon_2/\epsilon_1 - \sin^2 \theta^i)^{1/2}}{\epsilon_2/\epsilon_1 \cos \theta^i + (\epsilon_2/\epsilon_1 - \sin^2 \theta^i)^{1/2}}, \text{ and}$$

$$T_{\parallel} = \frac{2\epsilon_2/\epsilon_1 \cos \theta^i}{\epsilon_2/\epsilon_1 \cos \theta^i + (\epsilon_2/\epsilon_1 - \sin^2 \theta^i)^{1/2}}. \quad (25)$$

In this case, one can express  $H_1^r$  and  $H_1^t$  at the boundary ( $Z=0$ ) as

$$H_1^r(Z=0^+) = R_{\parallel} H_1^i(Z=0^+), \text{ and } H_1^t(Z=0^-) = T_{\parallel} H_1^i(Z=0^+). \quad (26)$$

The simplest case is when medium #2 is a perfect conductor ( $\sigma_2=\infty$ ). In that case

$$R_{\perp} = -1, \quad T_{\perp} = 0, \quad (27)$$

$$R_{\parallel} = 1, \quad \text{and } T_{\parallel} = 0. \quad (28)$$

#### B. Reflection Coefficient of Dielectric Slab

Now let us consider a more general problem, a dielectric layer of thickness  $d$  with dielectric constant  $\epsilon_d$  (real number), and "loss tangent"  $\tan \delta$ , as illustrated in Figure 6.

When an electromagnetic wave arrives at the front face, the wave is split into two waves, a portion of its energy will be reflected and the rest transmitted into the layer. At the opposite face of the slab the wave is split again, some of it being transmitted and the rest reflected back toward the front face. This process continues until the portion of the wave trapped inside the slab has completely left the layer through the front or back faces.

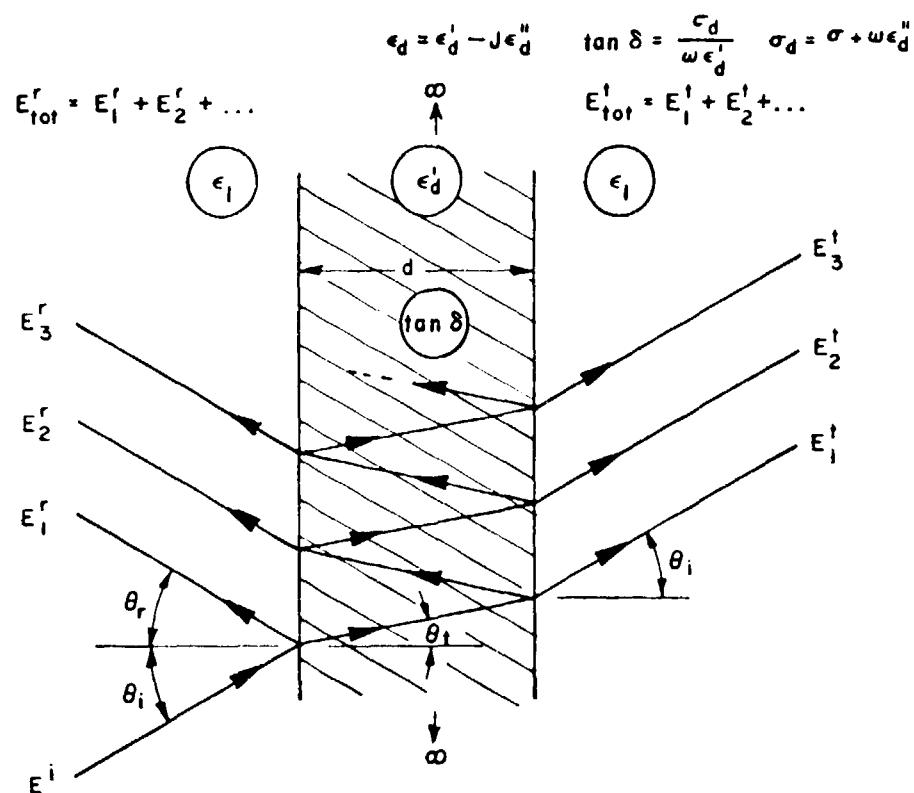


Figure 6. Reflection and transmission for a wave incident on a dielectric slab. The dielectric slab may have some loss.



The total reflected and transmitted fields will be equal to an infinite sum of waves, each of which can be related back to the original incident wave, provided that a plane wave propagation approximation inside the layer may be assumed. Before deriving the expressions for the transmission (T) and reflection (R) coefficients, it will be helpful to define the following variables:

- $R_1$  = reflection coefficient for the initial external reflection
- $R_2$  = reflection coefficient for the internal reflection
- $T_1$  = transmission coefficient into the dielectric layer
- $T_2$  = transmission coefficient out of the dielectric layer
- $P_a$  = phase term to account for the difference in path length to the observer for different rays leaving the layer, as illustrated in Figure 7
- $P_d$  = phase delay associated with the field in a single crossing of the slab.

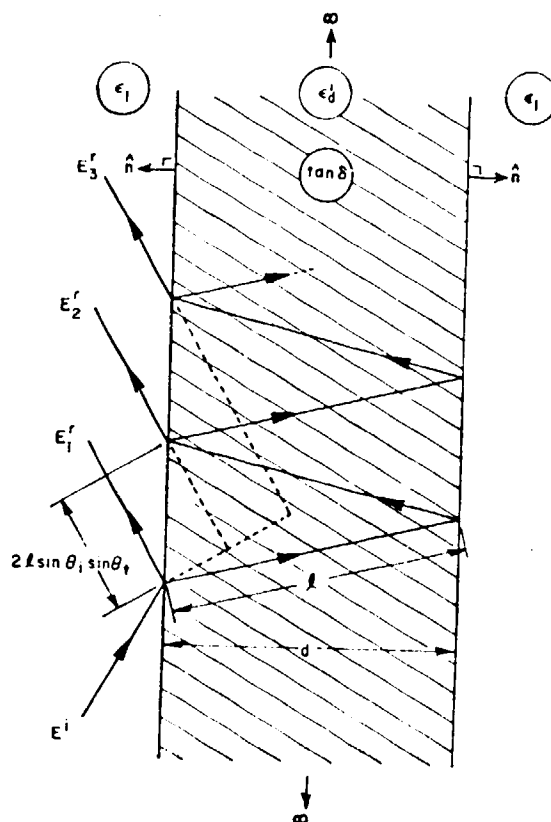


Figure 7. Difference in path length to observer for different rays emerging from slab.

Thus, assuming there is plane wave propagation within the layer, and the rays between the slab and observation point are parallel, the total reflected field for either polarization (" or 1) can be expressed as:

$$E_{\text{tot}}^r = \left\{ R_1 + T_1 T_2 R_2^2 P_d^2 P_a + T_1 T_2 R_2^3 P_d^4 P_a^2 + \dots \right\} E^i \quad (29)$$

or in a more compact notation

$$E_{\text{tot}}^r = \left\{ R_1 + T_1 T_2 \sum_{n=2}^{\infty} (R_2)^{2n-3} (P_d)^{2n-2} (P_a)^{n-1} \right\} E^i \quad (30)$$

The above assumptions will be satisfied, provided that neither the source nor receiver are too close to the dielectric slab.

From the definitions given above, it follows that:

$$P_d = e^{-\alpha d} e^{-j\beta l}, \quad P_a = e^{j2lk_1 \sin\theta_t \sin\theta_i}, \quad \text{and} \quad P_d^2 P_a = e^{-(\alpha/k_1 + j\beta' \cos\theta_t)2dk_1} \quad (31)$$

For the lossless case,

$$P_d = e^{-jk_d l} \quad (32)$$

where

$$k_d = \omega \sqrt{\epsilon_d \mu_d} = \omega \sqrt{\epsilon_d \mu_0}, \quad l = \frac{d}{\cos\theta_t} \quad (33)$$

It can be shown that  $R_2 = -R_1$ , where both coefficients have been defined earlier. Recall that  $T_1 = R_1 + 1$  and  $T_2 = R_2 + 1 = 1 - R_1$ . Substituting these into Equation (30), and making use of the geometric series relation

$$\sum_{n=0}^{\infty} a^n = \frac{1}{1-a} \quad \text{for } |a| < 1, \quad (34)$$

one obtains

$$E_{\text{tot}}^r = \frac{R_1 (1 - P_d^2 P_a)}{1 - R_1^2 P_d^2 P_a} E^i \quad (35)$$

or

$$E_{\text{tot}}^r(\mu, 1) = R(\mu, 1) E(\mu, 1)^i \quad (36)$$

where

$$R(\mu, 1) = \frac{R_1(\mu, 1)(1 - P_d^2 P_a)}{1 - R_1^2(\mu, 1) P_d^2 P_a} \quad (37)$$

Note that for the case of parallel polarization, the reflected and transmitted  $\vec{E}$ -field, in general will not have the same direction as the incident  $\vec{E}^i$ -field.

### C. Transmission Coefficient of Dielectric Slab

By the same argument as in the reflected field, the total transmitted field is also equal to an infinite sum, which can be expressed by

$$E_{\text{tot}}^t = \left\{ T_1 T_2 P_t \left[ P_d + P_d^3 P_a R_2^2 + P_d^5 P_a^2 R_2^4 + \dots \right] \right\} E^i, \quad (38)$$

or

$$E_{\text{tot}}^t = \left[ T_1 T_2 P_t \sum_{n=1}^{\infty} (P_d)^{2n-1} (P_a)^{n-1} (R_2)^{2n-2} \right] E^i, \quad (39)$$

where  $E^i$  is the incident field at the front face of the slab, and  $P_t$  is the term used in order to refer the phase of the transmitted field to the point of reference A, as illustrated in Figure 8.

Note that  $P_t$  is given by

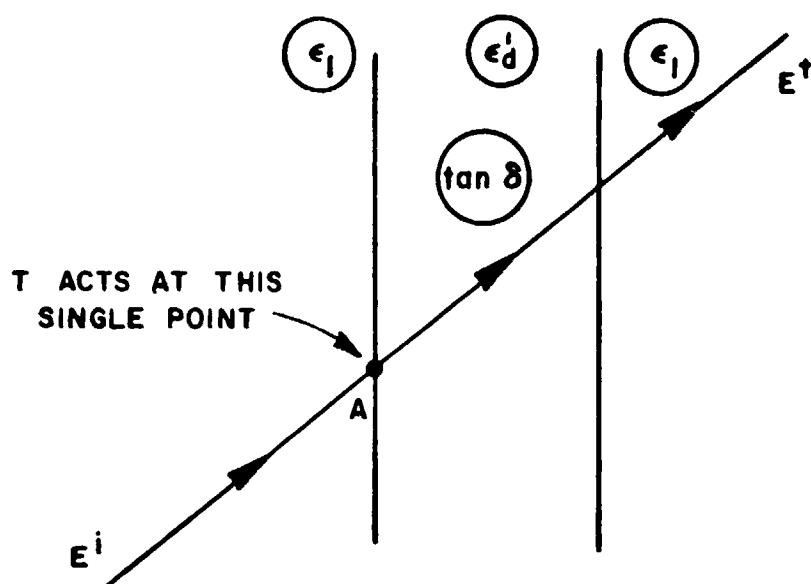
$$P_t = e^{jk_1 l \cos(\theta^i - \theta^t)} \quad (40)$$

Following the same procedure for the transmission problem one obtains

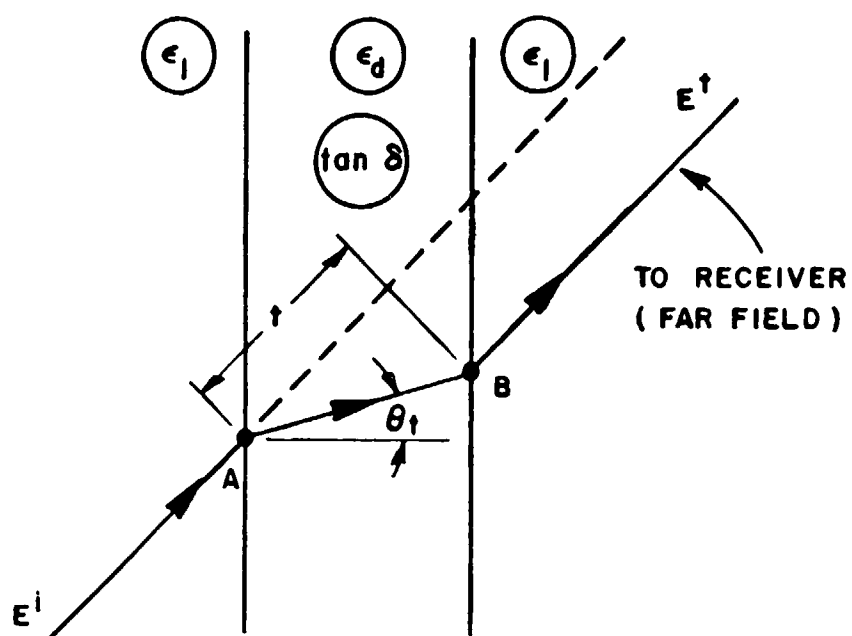
$$E_{\text{tot}}^t = \frac{(1 - R_1^2) P_d P_t E^i}{1 - R_1^2 P_d^2 P_a} \quad (41)$$

or

$$E_{\text{tot}}^t(\mu, 1) = T(\mu, 1) E(\mu, 1)^i \quad (42)$$



a) Assumed path.



b) An actual path.

Figure 8. Transmitted ray paths.

where

$$T_{(\parallel, \perp)} = \frac{(1 - R_{1(\parallel, \perp)}^2) P_d P_t}{1 - R_{1(\parallel, \perp)}^2 P_d^2 P_a}. \quad (43)$$

The coefficients  $T_{(\parallel, \perp)}$  and  $R_{(\parallel, \perp)}$  just derived, are valid, for flat layers of constant thickness, where the incident field is approximated by a plane wave.

### CHAPTER III

#### TWO DIMENSIONAL EDGE DIFFRACTED FIELD

The geometrical optics fields have two very serious defects, which makes them marginally useful in solving the problem mentioned at the introduction. These two defects are

- (1) G.O. fields are equal to zero in the shadow region, and
- (2) there is a discontinuity in the field at the shadow and reflection boundaries.

The shadow and reflection boundaries are shown in Figure 9.

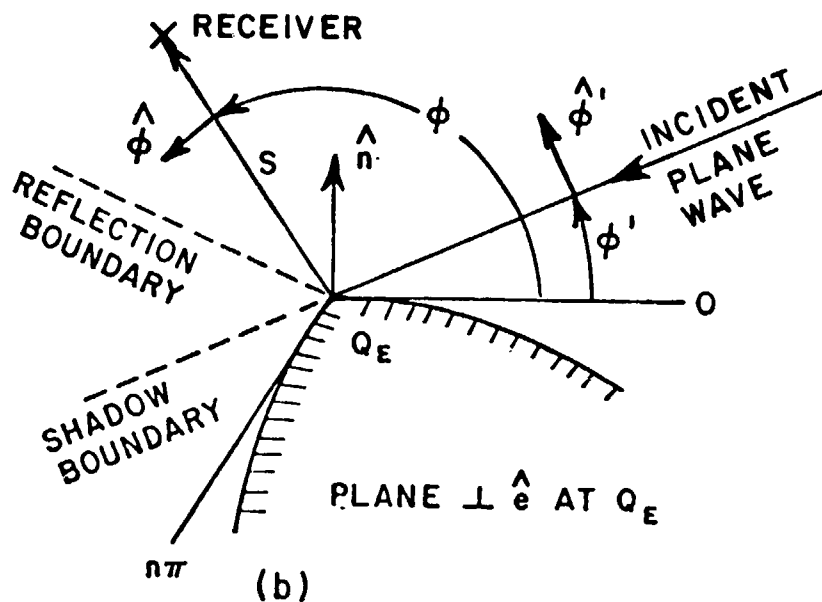


Figure 9. Geometry for 2-D edge diffraction.

To overcome these limitations an additional field, known as the diffracted field is added. Keller, who was the first to introduce this idea has shown in [1,2,3] how it can be added in the high frequency solution as an extension of geometrical optics. The postulates of Keller's theory, known as the Geometrical Theory of Diffraction (GTD) given in [4] are:

- (1) The diffracted field propagates along rays which are determined by a generalization of Fermat's principle to include points on the boundary surface in the ray trajectory.
- (2) Diffraction like reflection and transmission is a local phenomenon at high frequencies, which means that it depends only on the nature of the boundary surface and the incident field in the immediate neighborhood of the point of diffraction.
- (3) The diffracted wave propagates along its ray so that
  - a) power is conserved in a tube (or strip of rays),
  - b) the phase delay along the ray path equals the product of the wave number of the medium times the distance.

Diffracted rays are initiated at points on the boundary surface where the incident geometrical optics field is discontinuous, i.e., at points on the surface where there is a shadow or reflection boundary. These rays, like the geometrical optics rays travel along paths which make the optical distance between the source point and the field point an extremum, usually a minimum. For example, a ray path which transverses a homogeneous medium is a straight line, and if the ray path lies on a smooth curved surface, it is a surface extremum or geodesic.

The total high-frequency field at an observation point is obtained from the fields of all the rays passing through that point. The uniform GTD (UTD) requires that the diffracted field compensate the discontinuity in the geometrical optics field at the shadow and reflection boundaries so that the total high-frequency field is everywhere continuous away from the radiating body. This implies that the diffracted fields assume their largest values near these boundaries, where their magnitude is comparable to those of the G.O. field.

A general expression for the high-frequency edge diffracted field given in [4] is

$$E^d(s) \sim E^d(o) \sqrt{\frac{\rho_1 \rho_2}{(\rho_1 + s)(\rho_2 + s)}} e^{-jks} \quad (44)$$

where  $o$  is an arbitrary reference point. It is common practice to choose the point of diffraction on the boundary surface from which it emanates as the reference point. This point or line of diffraction happens to be one of the caustics of the diffracted field, and since  $E^d(s)$  is independent of the reference point the limit as  $\rho_1$  or  $\rho_2$  approach zero exists. The diffracted field for the case where the caustic is at an edge assumes the form

$$E^d(s) = \bar{A} \sqrt{\frac{\rho}{s(\rho+s)}} e^{-jks} \quad (45)$$

where  $\rho$  is the distance between the caustic on the point of diffraction and the second caustic of the diffracted ray away from this surface. The edge diffracted rays also form an astigmatic tube of rays as shown in Figure 2 with either the caustic 1-2 or 3-4 at the point of diffraction. Note that an expression for  $\rho$  which can determine from differential geometry will be given later. The edge may be an ordinary edge formed by a discontinuity in the unit normal vector, an edge formed by a discontinuity in surface curvature, or an edge formed by a discontinuity in some higher order derivative of the surface as shown in Figure 10.

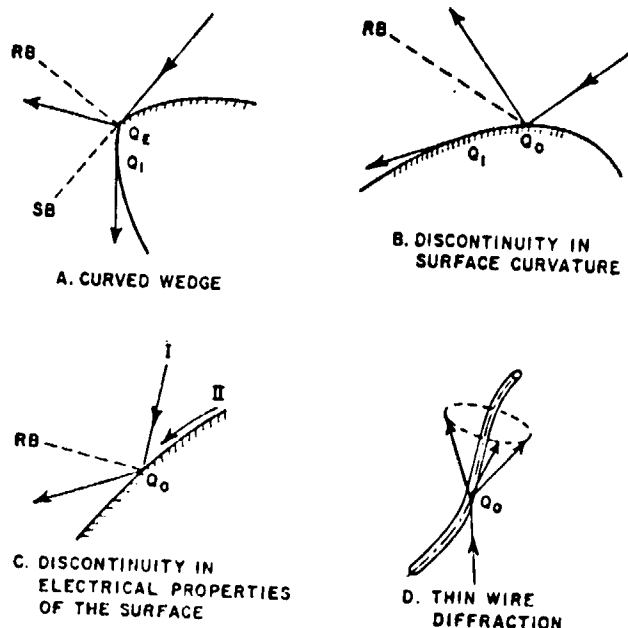


Figure 10. Diffraction from lines of discontinuity.



According to Keller's 2nd postulate, diffraction is a local phenomenon, and since one is dealing with a linear phenomenon,  $\bar{A}$  is proportional to the incident field at the point where diffraction is initiated.

Assuming that the magnitude of the incident field is not varying rapidly near the point of diffraction,  $\bar{A}$  has the form:

$$\bar{A} = \bar{E}^i(Q_E) \cdot \bar{D} \quad (46)$$

where  $Q_E$  is the point of diffraction, and  $\bar{D}$  the dyadic diffraction coefficient. The edge diffracted field can be rewritten as

$$\bar{E}^d(s) = \bar{E}^i(Q_E) \cdot \bar{D} \sqrt{\frac{\rho}{s(\rho+s)}} e^{-jks} \quad (47)$$

Applying the generalized Fermat's principle one arrives as shown in [8] to the equation

$$\hat{e} \cdot \hat{s}' = \hat{e} \cdot \hat{s}^r = \hat{e} \cdot \hat{s} \quad (48)$$

The unit vectors  $\hat{e}$ ,  $\hat{s}'$ ,  $\hat{s}$  are illustrated in Figure 11. It follows from Figure 11 where the angles  $\beta'_0$  and  $\beta_0$  are defined that

$$\cos \beta'_0 = \hat{e} \cdot \hat{s}' \quad 0 \leq \beta'_0 \leq \pi/2 \quad (49)$$

$$\cos \beta_0 = \hat{e} \cdot \hat{s} \quad 0 \leq \beta_0 \leq \pi/2 \quad (50)$$

For the 2-D case

$$\cos \beta'_0 = \cos \beta_0 = 0 \text{ or } \beta'_0 = \beta_0 = \pi/2 \quad (51)$$

Note that  $\beta'_0$  is the angle of incidence, and  $\beta_0$  the angle of diffraction. From Equation (48) Keller's Law of diffraction follows:

The angle of incidence  $\beta'_0$  is equal to the angle of diffraction  $\beta_0$ . This means that the diffracted rays emanating from  $Q_E$  form a cone whose half angle is  $\beta_0$  and whose axis is the tangent to the edge. The incident and reflected rays from  $Q_E$  also lie in this cone.

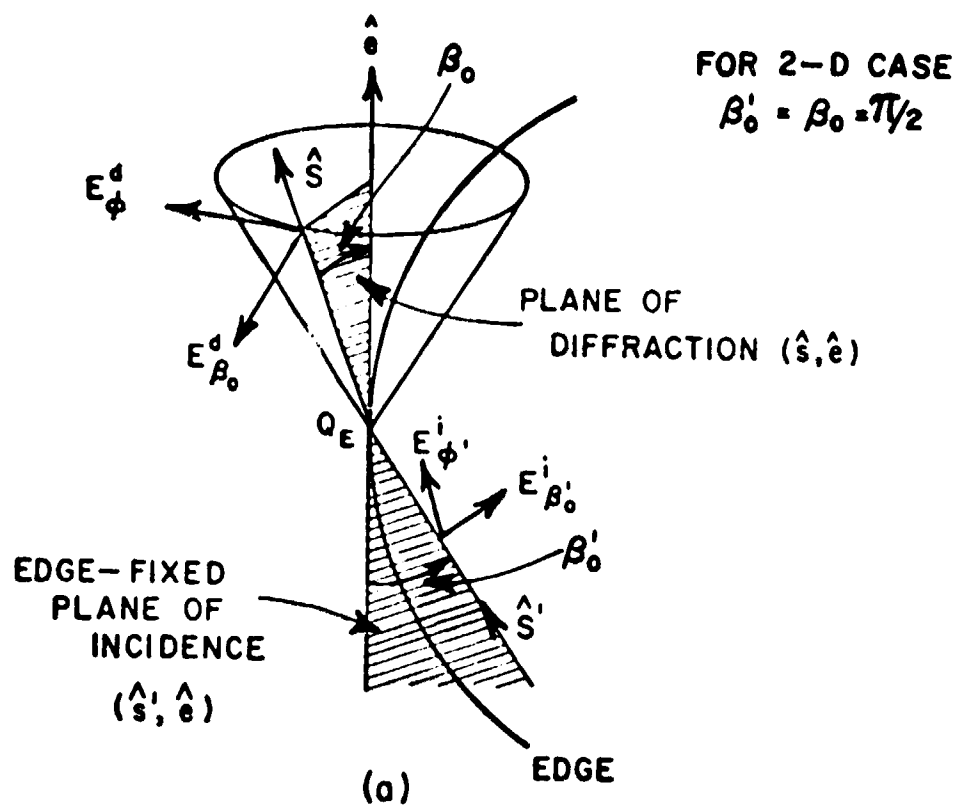


Figure 11. Diffraction at an edge.

The expression for  $\rho$  given in [8] is

$$\frac{1}{\rho} = \frac{1}{\rho_e} - \frac{\hat{n}_e \cdot (\hat{s}' - \hat{s})}{a \sin^2 \beta_0}, \quad (52)$$

where

$\rho_e^i$  = radius of curvature of incident wavefront at  $Q_E$  in the plane which contains  $\hat{s}'$  and  $\hat{e}$ .

$\hat{e}$  = unit vector tangent to the edge at  $Q_E$ .

$\hat{n}_e$  = unit vector normal to the edge at  $Q_E$  and directed away from the center of curvature of the edge.

$a$  = radius of curvature of the edge at  $Q_E$ .  $a > 0$ .

A special case, is the straight edge where  $a \rightarrow \infty$  and the expression for  $\rho$  simplifies to

$$\frac{1}{\rho} = \frac{1}{\rho_e}. \quad (53)$$

A general expression for the dyadic diffraction coefficient for a perfectly conducting wedge expressed in terms of the coordinate systems  $(\hat{s}, \hat{\beta}_0, \hat{\phi})$  and  $(\hat{s}', \hat{\beta}'_0, \hat{\phi}')$  (which will be defined in Chapter Four where the 3-D case is treated) is

$$\bar{D}(\phi, \phi'; \beta'_0) = -\hat{\beta}'_0 \hat{\beta}_0 D_s(\phi, \phi'; \beta'_0) - \hat{\phi}' \hat{\phi} D_h(\phi, \phi'; \beta'_0) \quad (54)$$

where  $D_s$  is the scalar diffraction coefficient for the acoustically soft (Dirichlet) boundary condition at the surface of the wedge, and  $D_h$  is the scalar diffraction coefficient for the acoustically hard (Neumann) boundary condition.

The region close to the reflection and shadow boundaries are known as transition regions. In these regions the total field changes rapidly, and the magnitude of the diffracted field as indicated before is comparable with the incident and reflected fields, which are discontinuous in these regions. The diffracted field must be discontinuous at shadow and reflection boundaries to yield a continuous total field everywhere as prescribed by UTD.

### A. Scalar Diffraction Coefficients for a Perfectly-Conducting Wedge

Expressions for the diffraction coefficients of a perfectly-conducting wedge which are valid both, within and outside the transition regions, but away from the edge and  $\phi'=0$ ,  $\phi=n\pi$  surfaces, are given by [8]

$$D_{sh}(\phi, \phi'; \beta_0') = \frac{-e^{-j\pi/4}}{2n\sqrt{2\pi k} \sin \beta_0} \times \left[ \cot\left(\frac{\pi+(\phi-\phi')}{2n}\right) F[kL^i a^+(\phi-\phi')] \right. \\ \left. + \cot\left(\frac{\pi-(\phi-\phi')}{2n}\right) F[kL^i a^-(\phi-\phi')] \right] + \left\{ \cot\left(\frac{\pi+(\phi+\phi')}{2n}\right) F[kL^{rn} a^+(\phi+\phi')] \right. \\ \left. + \cot\left(\frac{\pi-(\phi+\phi')}{2n}\right) F[kL^{ro} a^-(\phi+\phi')] \right\} \quad (55)$$

where  $F(x)$  is known as the transition function. The variable  $a^+(\phi, \phi')$  is a measure of the angular separation between the field point and a shadow or reflection boundary. The additional superscripts  $o, n$  denote that the radii of curvature are calculated at the reflection boundaries  $\pi-\phi'$  and  $(2n-1)\pi-\phi'$ , respectively. These boundaries are illustrated in Figure 13.

The transition function is defined as follows:

$$F(x) = 2j\sqrt{x} e^{jx} \int_{\sqrt{x}}^{\infty} \frac{e^{-j\tau^2}}{\sqrt{\tau}} d\tau, \quad x = kLa(\phi, \phi') \quad (56)$$

in which one takes the principal (positive) branch of the square root. When  $x$  is small,

$$F(x) \sim \left\{ \sqrt{\pi x} - 2xe^{j\pi/4} - \frac{2}{3} x^2 e^{-j\pi/4} \right\} e^{j(\pi/4+x)} \quad (57)$$

and when  $x$  is large

$$F(x) \sim 1 + j \frac{1}{2x} - \frac{3}{4} \frac{1}{x^2} - j \frac{15}{8} \frac{1}{x^3} + \frac{75}{76} \frac{1}{x^4} \quad (58)$$

if  $x > 10$

$$F(x) \approx 1 \quad (59)$$

and for all  $x$

$$|F(x)| \leq 1 \quad 0 \leq \text{phase of } F(x) \leq \pi/4. \quad (60)$$

A plot of  $|F(x)|$  and phase of  $F(x)$  is given in Figure 12.

Let  $\beta = \phi \pm \phi'$ , then

$$a^{\pm}(\beta) = 2 \cos^2 \left( \frac{2\pi n N^{\pm} - \beta}{2} \right), \quad (61)$$

where  $N^{\pm}$  are integers which most nearly satisfy

$$2\pi n N^{+} - \beta = \pi, \text{ and} \quad (62)$$

$$2\pi n N^{-} - \beta = -\pi. \quad (63)$$

#### B. Distance Parameters

The distance parameters are defined as [8]

$$L^i = \frac{s(\rho_e^i + s)\rho_1^i \rho_2^i \sin^2 \beta_0}{\rho_e^i (\rho_1^i + s)(\rho_2^i + s)}, \text{ and} \quad (64)$$

$$L^r = \frac{s(\rho_e^r + s)\rho_1^r \rho_2^r \sin^2 \beta_0}{\rho_e^r (\rho_1^r + s)(\rho_2^r + s)}, \quad (65)$$

where  $\rho_1^i, \rho_2^i$  are the principal radii of curvature of the incident wavefront at  $Q_E$ . Further,  $\rho_1^r, \rho_2^r$  are the principal radii of curvature of the reflected wavefront at  $Q_E$ , and  $\rho_e^r$  is the distance between the caustics of the diffracted ray in the direction of specular reflection [8]. Note that  $\rho_e^r$  is given by

$$\frac{1}{\rho_e^r} = \frac{1}{\rho_e^i} - \frac{2(\hat{n} \cdot \hat{n}_e)(\hat{s}' \cdot \hat{n})}{a \sin^2 \beta_0}, \quad (66)$$

where  $\hat{n}$  is the unit outward vector normal to the surface near the edge.

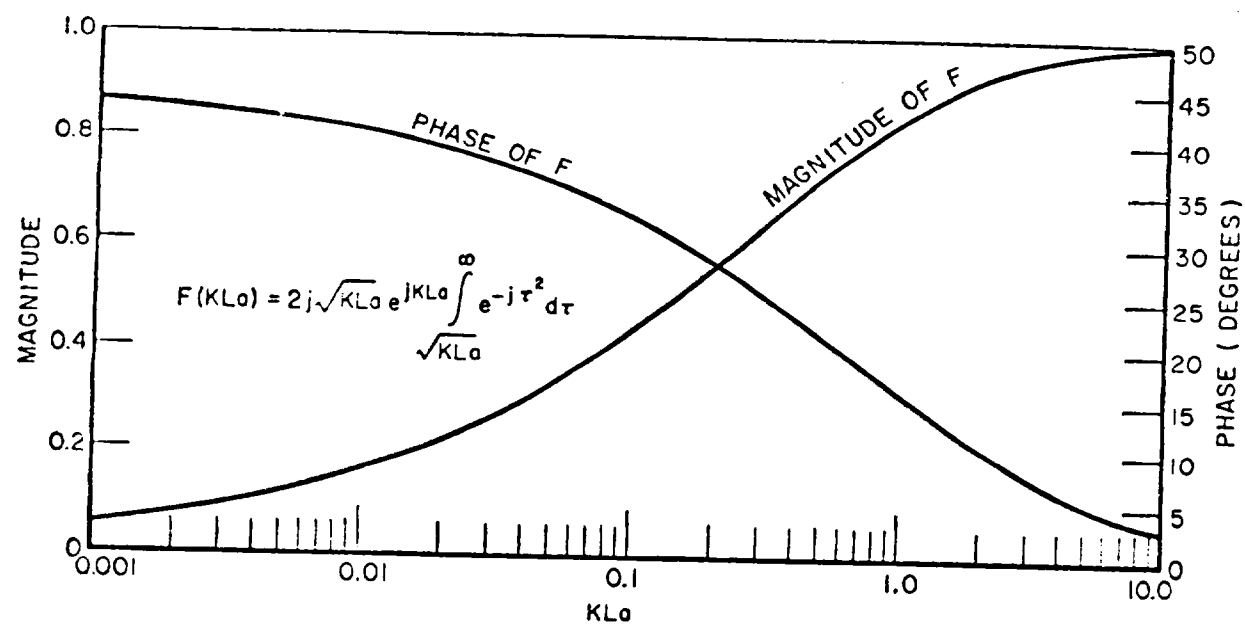


Figure 12. Transition function.

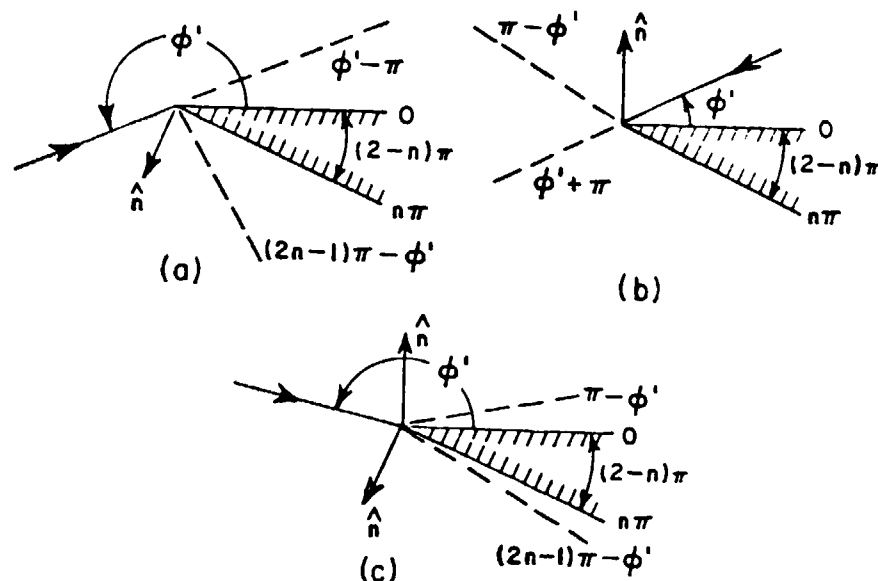


Figure 13. Shadow and reflection boundaries for different angles of incidence  $\phi'$ .

When the edge is formed by intersecting planar surfaces, one finds that  $L^{ro} = L^{rn} = L^i$ . But when the surfaces forming the wedge are curved, the spreading of the reflected wave is different from that of the incident wave. This means that the radii of curvature of the reflected and diffracted wavefronts at the reflection shadow boundary are different from the radii of curvature of the incident and diffracted wavefronts at the incident shadow boundary. Thus, the parameters  $L^i$ ,  $L^{ro}$ , and  $L^{rn}$  are needed to obtain a continuous total field.

#### C. Scalar Diffraction Coefficients for a Dielectric-Dielectric/Metal Junction

To generalize the edge diffraction coefficients for the perfectly-conducting case to include diffraction due to a junction of two dielectric plates, or a dielectric-metal junction as illustrated in Figure 14, the following assumptions are made

- (a)  $n \neq 1$ , or  $n = 2$
- (b) the width of the dielectric plates is a small fraction of a wavelength.

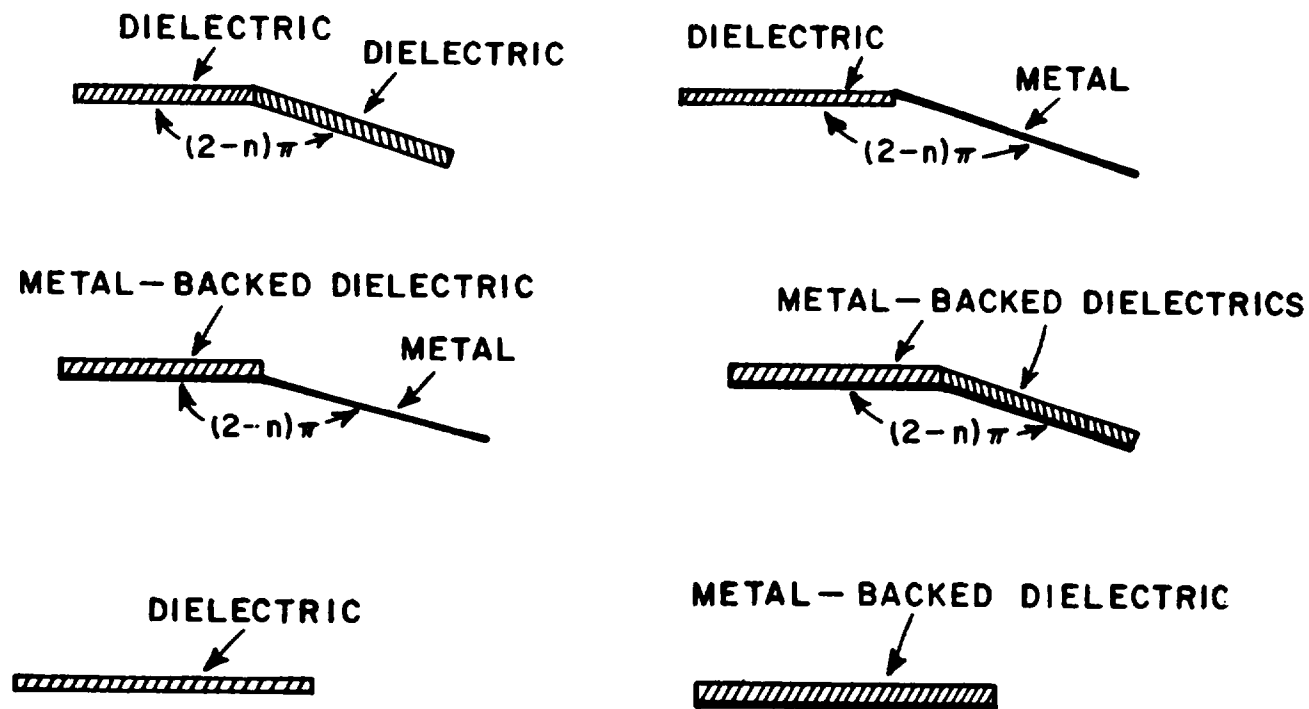


Figure 14. Various geometries for which the junction diffraction coefficient is valid.



Let us assume that  $D_s$  is given by

$$D_s(\phi, \phi'; \beta_0) = L_0^s D_0^h(\phi - \phi') + L_n^s D_n^h(\phi - \phi') + A_0^s D_0^h(\phi + \phi') + A_n^s D_n^h(\phi + \phi') \quad (67)$$

where  $L_0^s$ ,  $L_n^s$ ,  $A_0^s$  and  $A_n^s$  are constants, and

$$D_n^h(\phi - \phi') = \frac{-e^{-j\pi/4}}{2n\sqrt{2\pi k} \sin\beta_0} \cot\left(\frac{\pi(\phi - \phi')}{2n}\right) F\left[kL^{\text{rn}} i^+ a^+(\phi - \phi')\right], \text{ and} \quad (68)$$

$$D_0^h(\phi - \phi') = \frac{-e^{-jn/4}}{2n\sqrt{2\pi k} \sin\beta_0} \cot\left(\frac{\pi(\phi - \phi')}{2n}\right) F\left[kL^{\text{ro}} i^+ a^-(\phi - \phi')\right], \quad (69)$$

where again the subscript o refers to the 0 surface and n to the  $n\pi$  surface as illustrated in Figure 13.

It follows from Table I, and Equations (68)-(69) that  $D_0(\phi - \phi')$  is associated with the incident shadow boundary discontinuity due to the 0-side of the wedge, and  $D_0(\phi + \phi')$  takes care of the reflection boundary discontinuity associated with the same face. Likewise, the  $D_n(\phi - \phi')$  terms play the same role, but for the  $n\pi$ -face of the wedge.

For the perfectly-conducting case, the reflection coefficient is  $R^h = \mp 1$ . Thus, for the special case ( $\sigma = \infty$ )  $L_0 = L_n = 1$  and  $A_0 = A_n = R^h = \mp 1$ .

Since the coefficients  $A_0$ ,  $A_n$ ,  $L_0$  and  $L_n$  multiplying the  $D_0$ , and  $D_n$  terms in Equation (67) are all constants, the  $L^i$  and  $L^r$  parameters do not change. This adds a restriction to the surfaces (dielectric) making up the wedge; they will have to be flat, so the radii of curvature of the transmitted field is the same as the incident field at the incident shadow boundary. This is a necessary condition in order to obtain a continuous total field as will be shown below.

Near the shadow or reflection boundaries, i.e.,  $\beta = 2\pi n N^{\pm} + (\pi - \epsilon)$

$$\cot\left(\frac{\pi - \beta}{2n}\right) F(kLa^{\pm}(\beta)) \sim n \left[ \sqrt{2\pi kL} \operatorname{sgn} \epsilon - 2kL \epsilon e^{j\pi/4} \right] e^{j\pi/4} \quad (70)$$

where

$$\epsilon > 0 \text{ (Lit region)} \quad \epsilon < 0 \text{ (Shadow region)}. \quad (71)$$

Near the shadow boundary due to the 0-face of the wedge, i.e.,  $\phi' + \pi$  boundary as shown in Figure 13.

TABLE I

	The cotangent is singular when	value of N at the boundary
$\cot\left(\frac{\pi + (\phi - \phi')}{2n}\right)$	$\phi = \phi' - \pi$ , a SB surface $\phi=0$ is shadowed	$N^+ = 0$
$\cot\left(\frac{\pi - (\phi - \phi')}{2n}\right)$	$\phi = \phi' + \pi$ , a SB surface $\phi=n\pi$ is shadowed	$N^- = 0$
$\cot\left(\frac{\pi + (\phi + \phi')}{2n}\right)$	$\phi = (2n-1)\pi - \phi'$ , a RB reflection from surface $\phi=n\pi$	$N^+ = 1$
$\cot\left(\frac{\pi - (\phi + \phi')}{2n}\right)$	$\phi = \pi - \phi'$ , a RB reflection from surface $\phi=0$	$N^- = 0$

$$D_0(\phi - \phi') \sim \frac{-e^{-j\pi/4}}{2n\sqrt{2\pi k} \sin \beta_0} n \left[ \sqrt{2\pi kL} \operatorname{sgn} \epsilon - 2kL \epsilon e^{j\pi/4} \right] e^{j\pi/4} \quad (72)$$

and

$$E^d(\text{SB}) \sim e^{-jks} \sqrt{\frac{\rho}{s(\rho+s)}} E^i(\text{QE}) \left[ -\frac{\sqrt{L} \operatorname{sgn} \epsilon}{2 \sin \beta_0} \right] L_0 + \text{small continuous terms}$$

where the term containing  $\epsilon$  has been neglected because  $\epsilon \rightarrow 0$ . Recall that

$$\frac{\sqrt{L}}{\sin \beta_0} = \left[ \frac{s(\rho_e^i + s) \rho_1^i \rho_2^i}{\rho_e^i (\rho_1^i + s) (\rho_2^i + s)} \right]^{1/2}, \text{ and} \quad (73)$$

$$\frac{1}{\rho} = \frac{1}{\rho_e^i} - \frac{\hat{n}_e \cdot (\hat{s}' - \hat{s})}{a \sin \beta_0} \quad (74)$$

Further at the shadow boundary  $\hat{s}' = \hat{s} = \frac{1}{\rho} = \frac{1}{\rho_e}$ , thus

$$E^d(SB) \sim -L_0 \frac{E^i(QE)}{2} \sqrt{\frac{\rho_e^i}{s(\rho_e^i + s)}} \sqrt{\frac{s(\rho_e^i + s)\rho_1^i \rho_2^i}{\rho_e^i(\rho_1^i + s)(\rho_2^i + s)}} \operatorname{sgn} \epsilon e^{-jks} \\ + \text{small continuous terms. (75)}$$

Equation (75) simplifies to

$$E^d(SB) \sim -\frac{L_0}{2} E^i(QE) \sqrt{\frac{\rho_1^i \rho_2^i}{(\rho_1^i + s)(\rho_2^i + s)}} e^{-jks} \operatorname{sgn} \epsilon \\ + \text{small continuous terms. (76)}$$

The incident field at a distance  $s$  from the edge in the lit side of the  $\phi' + \pi$  boundary is

$$E^i(s) = E^i(QE) \sqrt{\frac{\rho_1^i \rho_2^i}{(s + \rho_1^i)(s + \rho_2^i)}} e^{-jks} \quad (77)$$

On the shadow side of the  $\phi' + \pi$  boundary

$$E^{\text{trans}}(s) = T_0 E^i(QE) \sqrt{\frac{\rho_1^i \rho_2^i}{(\rho_1^i + s)(\rho_2^i + s)}} e^{-jks}, \quad (78)$$

where  $T_0$  is the transmission coefficient for the 0-face of the wedge. Recall that  $T_0$  is valid for a flat slab only. The total field on the lit side of the  $\phi' + \pi$  boundary ( $\epsilon > 0$ ) is

$$E^{\text{tot}}(s) = E^i(s) + E^d(s), \quad (79)$$

and in the limit as  $\epsilon \rightarrow 0$  from the  $0^+$  side

$$E^{\text{total}}(s) = E^i(QE) \sqrt{\frac{\rho_1^i \rho_2^i}{(s + \rho_1^i)(s + \rho_2^i)}} e^{-jks} \left( \frac{-L_0}{2} + 1 \right) \\ + \text{small continuous terms (80)}$$

in the shadow side of the same boundary ( $\epsilon < 0$ ), and in the limit as  $\epsilon \rightarrow 0$  from the  $0^-$  side

$$E^{\text{tot}}(s) = E^i(\text{QE}) \sqrt{\frac{\rho_1^i \rho_2^i}{(s+\rho_1^i)(s+\rho_2^i)}} e^{-jks(\frac{L_0}{2} + T_0)} + \text{small continuous terms} \quad (81)$$

but

$$E^{\text{tot}}(\epsilon > 0) = E^{\text{tot}}(\epsilon < 0) \quad (82)$$

therefore

$$-\frac{L_0}{2} + 1 = \frac{L_0}{2} + T_0 \quad (83)$$

or

$$L_0 = 1 - T_0 \quad (84)$$

The same procedure is used at the  $\phi' - \pi$  shadow boundary due to the  $n\pi$ -face of the wedge (see Figure 13) to obtain an expression for  $L_n$ ,

$$L_n = 1 - T_n \quad (85)$$

where  $T_n$  is the transmission coefficient of the  $n\pi$ -face of the wedge.

Near the  $\pi - \phi'$  reflection boundary

$$D_0(\phi + \phi') \sim -\frac{e^{-j\pi/4}}{2n\sqrt{2\pi k} \sin\beta_0} n \left[ \sqrt{2\pi k L}^{ro} \text{sgn}\epsilon - 2kL^{ro} \epsilon e^{j\pi/4} \right] e^{j\pi/4} \quad (86)$$

and

$$E^d(\text{RB}) \sim A_0 e^{-jks} \sqrt{\frac{\rho}{s(\rho+s)}} E^i(\text{QE}) \left[ \frac{\sqrt{L}^{ro} \text{sgn}\epsilon}{2s \sin\beta_0} \right] + \text{small continuous terms} \quad (87)$$

where again, the term containing  $\epsilon$  has been neglected. Recall that

$$\frac{\sqrt{L^{ro}}}{\sin \beta_0} = \sqrt{\frac{s(\rho_e^r + s)(\rho_1^{ro} \rho_2^{ro})}{\rho_e^r (s + \rho_2^{ro})(s + \rho_1^{ro})}} \quad (88)$$

where

$$\frac{1}{\rho_e^r} = \frac{1}{\rho_e^i} - \frac{2(\hat{n} \cdot \hat{n}_e)(\hat{s}' \cdot \hat{n})}{a \sin^2 \beta_0} \quad (89)$$

and  $\hat{n}$  is the unit vector normal to the o-face of the wedge near the reflection boundary  $\pi - \phi'$ . In addition,

$$\hat{s}' \cdot \hat{n} = -\cos \theta_i \quad (90)$$

and

$$\frac{1}{\rho_e^r} = \frac{1}{\rho_e^i} + \frac{2\hat{n} \cdot \hat{n}_e \cos \theta_i}{a \sin^2 \beta_0} \quad (91)$$

Letting  $\hat{n} \cdot \hat{n}_e = \cos \alpha$  where  $\alpha$  is the angle between  $\hat{n}$  and  $\hat{n}_e$ , one finds that

$$\frac{1}{\rho_e^r} = \frac{1}{\rho_e^i} + \frac{2\cos \alpha \cos \theta_i}{a \sin^2 \beta_0} \quad (92)$$

It can be shown that

$$\hat{n}_e \cdot \hat{s}' = -\cos(\theta_i \mp \alpha) \quad (93)$$

and

$$\hat{n}_e \cdot \hat{s} = \cos(\theta_i \pm \alpha) \quad (94)$$

at the  $\pi - \phi'$  boundary. It follows that

$$\frac{1}{\rho} = \frac{1}{\rho_e^i} + \frac{\cos(\theta_i \mp \alpha) + \cos(\theta_i \pm \alpha)}{a \sin^2 \beta_0} = \frac{1}{\rho_e^i} + \frac{2\cos \theta_i \cos \alpha}{a \sin^2 \beta_0} \quad (95)$$

therefore  $\frac{1}{\rho} = \frac{1}{\rho_r}$  at the reflection boundary such that

$$E^d(RB) \sim -e^{-jks} \frac{A_0}{2} E^i(QE) \left[ \frac{\rho_1^{ro} \rho_2^{ro}}{(s+\rho_1^{ro})(s+\rho_2^{ro})} \right]^{1/2} \operatorname{sgn} \epsilon + \text{small continuous terms.} \quad (96)$$

The reflected field at a distance  $s$  from the edge in the lit side of the reflection boundary  $\pi-\phi'$  is

$$E^r(s) = E^i(QE) R_0 \left[ \frac{\rho_1^{ro} \rho_2^{ro}}{(s+\rho_1^{ro})(s+\rho_2^{ro})} \right]^{1/2} e^{-jks}, \quad (97)$$

where  $R_0$  is the reflection coefficient of the o-face of the wedge.

The total field in the lit side of the  $\pi-\phi'$  boundary ( $\epsilon > 0$ ) is

$$E^{\text{tot}}(s) = E^r(s) + E^d(s) + E^i(s) \quad (98)$$

and in the limit as  $\epsilon \rightarrow 0$  from the  $0^+$  side

$$E^{\text{tot}}(s) = E^i(QE) \left[ \frac{\rho_1^{ro} \rho_2^{ro}}{(s+\rho_1^{ro})(s+\rho_2^{ro})} \right]^{1/2} e^{-jks} \left( R_0 - \frac{A_0}{2} \right) + E^i(s) + \text{small continuous terms.} \quad (99)$$

For  $\epsilon < 0$ , i.e., the shadow side of the reflection boundary, and taking the limit  $\epsilon \rightarrow 0$

$$E^{\text{tot}}(s) = \frac{E^i(QE)}{2} \left[ \frac{\rho_1^{ro} \rho_2^{ro}}{(s+\rho_1^{ro})(s+\rho_2^{ro})} \right]^{1/2} e^{-jks} A_0 + E^i(s) + \text{small continuous terms.} \quad (100)$$

Since the total field has to be continuous, it follows that

$$R_0 - \frac{A_0}{2} = \frac{A_0}{2} \quad \text{or} \quad A_0 = R_0. \quad (101)$$

Following the same procedure at the  $(2n-1)\pi-\phi'$  reflection boundary due to the  $n\pi$ -face of the wedge, one finds that

$$A_n = R_n \quad (102)$$

where  $R_n$  is the reflection coefficient of the n-face.

Therefore  $D_h^S$  in the 2-D case can be written in the following way

$$D_h^S(\phi, \phi', \beta'_0) = (1 - T_0^{\hat{H}}) D_0(\phi - \phi') + (1 - T_n^{\hat{H}}) D_n(\phi - \phi') + R_0^{\hat{H}} D_0(\phi + \phi') + R_n^{\hat{H}} D_n(\phi + \phi') \quad (103)$$

Equation (103) reduces to the more familiar expression for  $D_h^S$  where  $T_0 = T_n = 0$ , and  $R_0^{\hat{H}} = R_n^{\hat{H}} = \bar{1}$  for the perfect conductor,

$$D_h^S(\phi, \phi', \beta'_0) = D_0(\phi - \phi') + D_n(\phi - \phi') + [D_0(\phi + \phi') + D_n(\phi + \phi')] \quad (104)$$

Since the transmission and reflection coefficients for the dielectric material were calculated for flat layers only, Equation (103) is valid for wedges whose faces are flat dielectric layers. Note that for the

2-D case  $R^{\hat{H}} = R^{\perp}$ , and  $T^{\hat{H}} = T^{\perp}$ .

The thickness of the dielectric slabs are not arbitrary either, because the diffracted field is calculated assuming that there is one line of diffraction on the various edges of the slabs, instead of two, which would be the case for thick layers. That is to say if the slabs were electrically thick, then one would obtain a diffracted field from both edges making up the thick edges of the slabs.

It is possible to obtain a diffraction coefficient for the curved surface dielectric-wedge case by adding two additional terms similar to the  $D_0$  and  $D_n$  expressions. That is necessary because the transmitted field wavefront may have different radii of curvature from that of the incident field. The transmitted field can be expressed as the sum of two fields; one of them having the same radii of curvature as the incident field, and the other obviously will have a different wavefront. The two additional terms in the diffraction coefficient will have the transition functions necessary to extend the latter field (transmitted field with different wavefront from that of the incident field) into the lit region across the  $\phi' + \pi$  and  $\phi' - \pi$  shadow boundaries. In other words, they contain the two additional  $L^{10}$  and  $L^{1n}$  parameters, and the transition function  $F(x)$  needed to obtain a continuous total field everywhere. To complete the solution one would have to obtain expressions for the reflection and transmission coefficients valid for curved dielectric layers.

## CHAPTER IV

### THREE-DIMENSIONAL SLAB SCATTERING

In order to express the geometrical optics and diffracted fields in three-dimensions (3-D), it is necessary to define a suitable set of coordinate systems. Obviously there is an infinite number of coordinate systems that one can choose, but certain ones will be more convenient than others. Thus, one must pick the coordinate system within which the expressions for the fields are the simplest.

#### A. Ray-Fixed Coordinate System

In the case of the geometrical optics fields, the natural coordinate system is referred to as the "ray-fixed" coordinate system and is defined by

$$\hat{u}_{\perp} = \frac{\hat{n} \times \hat{s}'}{|\hat{n} \times \hat{s}'|}, \quad (105)$$

$$\hat{u}_{\parallel}^i = \hat{s}' \times \hat{u}_{\perp}, \text{ and} \quad (106)$$

$$\hat{u}_{\parallel}^r = \hat{s} \times \hat{u}_{\perp}, \quad (107)$$

where  $\hat{n}$  is the unit vector normal to the surface at the point of incidence as shown in Figure 15. Note  $\hat{s}'$  is the incident unit vector in the direction from the source to the surface, and  $\hat{s}$  is the reflection unit vector from the point of reflection to the observation point.

The plane of incidence is the plane containing  $\hat{s}'$  and  $\hat{n}$ , and the plane of reflection is the plane containing  $\hat{s}$  and  $\hat{n}$ . It follows from the law of reflection that both planes are the same. Note that ( $\perp$ ) and ( $\parallel$ ) indicate vectors perpendicular and parallel to the plane of incidence, respectively. The unit vectors  $(\hat{s}', \hat{u}_{\perp}, \hat{u}_{\parallel}^i)$  form an orthonormal basis set of coordinates for the incident and transmitted fields. Likewise the unit vectors  $(\hat{s}, \hat{u}_{\perp}, \hat{u}_{\parallel}^r)$  form an orthonormal basis set for the reflected field.

#### B. Edge-Fixed Coordinate System

The coordinate system defined above, although ideal for the G.O. fields, it is not the natural system for the diffracted fields. The coordinate system used to define the dyadic diffraction coefficient is referred to as the "edge-fixed" coordinate system.



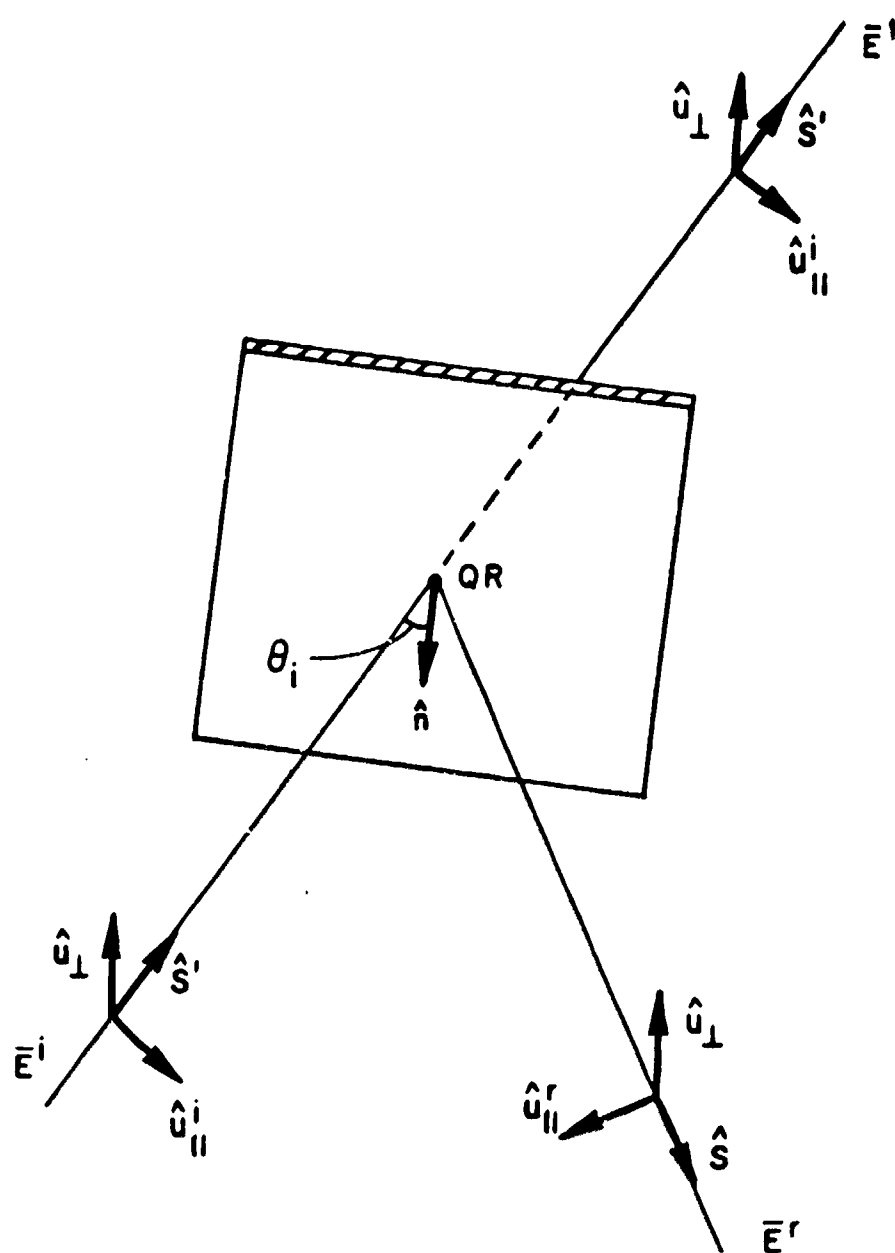


Figure 15. Ray fixed coordinate system used for 3D reflection and transmission.

First of all, two new planes need to be defined: the edge-fixed plane of incidence, which contains the incident ray and the unit vector  $\hat{e}$  tangent to the edge at the point of incidence  $Q_E$ , and the plane of diffraction, which contains the diffracted ray and  $\hat{e}$ . Both planes are illustrated in Figure 16.

The unit vectors  $\hat{\phi}'$  and  $\hat{\phi}$  are perpendicular to the edge-fixed plane of incidence and the plane of diffraction, respectively. The unit vectors  $\hat{\beta}'$  and  $\hat{\beta}$  lie in the edge-fixed plane of incidence and the plane of diffraction, respectively as illustrated in Figure 16.

Again, let  $\hat{S}'$  be the incident unit vector from the source to the diffraction point  $Q_E$ , and  $\hat{S}$  the unit vector from  $Q_E$  to the observation point. From the above definitions it follows that:

$$\hat{\phi}' = \frac{-\hat{e} \times \hat{S}'}{|\hat{e} \times \hat{S}'|} \quad (108)$$

$$\hat{\beta}'_0 = \hat{\phi}' \times \hat{S}' \quad (109)$$

$$\hat{\phi} = \frac{\hat{e} \times \hat{S}}{|\hat{e} \times \hat{S}|} \quad , \text{ and} \quad (110)$$

$$\hat{\beta}'_0 = \hat{\phi} \times \hat{S} \quad (111)$$

These vectors form the two orthonormal basis of the "edge-fixed" coordinate system. Thus, the coordinates of the diffracted ray  $(s, \beta, \phi)$  are spherical coordinates, and so are the coordinates of the incident ray  $(s', \beta', \phi')$ , except that the incident (radial) unit vector  $\hat{S}'$  points toward the origin  $Q_E$ .

### C. Dyadic Reflection Coefficient

The reflected field in the "ray-fixed" coordinate system can be expressed as

$$\vec{E}^r(s) = \vec{E}^i(QR) \cdot \bar{R} f_r(s) \quad (112)$$

where

$$\bar{R} = \hat{e}_\parallel^i \hat{e}_\parallel^r R_\parallel + \hat{e}_\perp^i \hat{e}_\perp^r R_\perp \quad (113)$$

which is the dyadic reflection coefficient. Note that  $R_\parallel$  and  $R_\perp$  are the scalar reflection coefficients for the parallel and perpendicular polarizations, respectively.

$$\text{Further, } f_r(s) = \left[ \frac{\rho_1^r \rho_2^r}{(\rho_1^r + s)(\rho_2^r + s)} \right]^{1/2} e^{-jks} \quad (114)$$

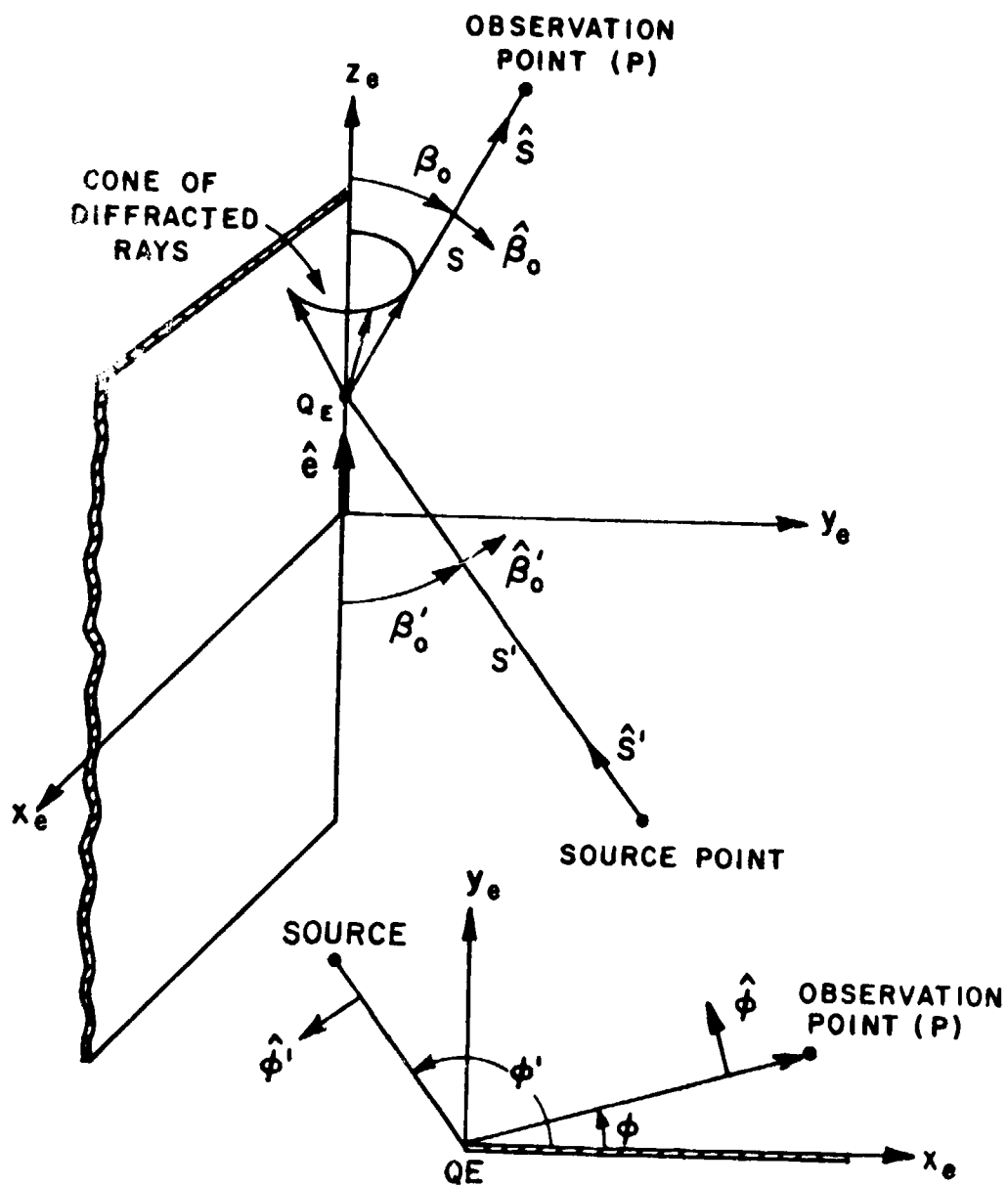


Figure 16. Edge fixed coordinate system used for 3D diffraction.

In matrix notation, the dyadic reflection coefficient has the form:

$$R = \begin{bmatrix} R_{\parallel} & 0 \\ 0 & R_{\perp} \end{bmatrix}, \quad (115)$$

and the reflected field is given by

$$\begin{bmatrix} E_{\parallel}^r(s) \\ E_{\perp}^r(s) \end{bmatrix} = \begin{bmatrix} R_{\parallel} & 0 \\ 0 & R_{\perp} \end{bmatrix} \begin{bmatrix} E_{\parallel}^i(QR) \\ E_{\perp}^i(QR) \end{bmatrix} f_r(s). \quad (116)$$

#### D. Dyadic Transmission Coefficient

Similarly, the transmitted field can be expressed in the following way:

$$\vec{E}^{\text{trans}}(s) = \vec{E}^i(QR) \cdot \bar{T} f_t(s) \quad (117)$$

where  $\bar{T}$  is the dyadic transmission coefficient

$$\bar{T} = \hat{e}_{\parallel}^i \hat{e}_{\parallel}^i T_{\parallel} + \hat{e}_{\perp}^i \hat{e}_{\perp}^i T_{\perp}. \quad (118)$$

Note that  $T_{\parallel}$  and  $T_{\perp}$  are the transmission coefficients for the parallel and perpendicular polarizations, respectively.

Further,

$$f_t(s) = \left[ \frac{\rho_1^t \rho_2^t}{(s + \rho_1^t)(s + \rho_2^t)} \right]^{1/2} e^{-jks}, \quad (119)$$

where the superscript  $t$  refers to the radii of curvature of the transmitted field wavefront. Since the expressions for  $T_{\parallel}$  and  $T_{\perp}$  given earlier are valid for flat plates only,  $\rho_1^t$  and  $\rho_2^t$  are equal to the two radii of curvature of the incident field wavefront.

In matrix notation  $\vec{E}^{\text{trans}}$  can be expressed as

$$\begin{bmatrix} E_{\parallel}^{\text{trans}}(s) \\ E_{\perp}^{\text{trans}}(s) \end{bmatrix} = \begin{bmatrix} T_{\parallel} & 0 \\ 0 & T_{\perp} \end{bmatrix} \begin{bmatrix} E_{\parallel}^i(QR) \\ E_{\perp}^i(QR) \end{bmatrix} f_t(s). \quad (120)$$

The angle of incidence to be used in computing the reflection and transmission coefficients is given by

$$\theta_i = \cos^{-1} (-\hat{S}' \cdot \hat{n}) \quad 40 \quad (121)$$

Note that only two components perpendicular to the direction of propagation are needed to specify the geometrical optics fields, because of the nature of the G.O. fields, i.e., they are always perpendicular to the direction of propagation.

#### E. Dyadic Diffraction Coefficient

The ordinary plane of incidence which contains the unit vectors  $\hat{s}'$  and  $\hat{n}$ , intersects the edge-fixed plane of incidence along the incident ray, and the edge-fixed plane of reflection, which contains the vectors  $\hat{e}$  and  $\hat{s}'$  along the reflected ray. This is depicted in Figure 17.

Let the angle between the edge-fixed plane of incidence and the ordinary plane of incidence be  $-\alpha$ . It is shown in [8] that the angle between the edge-fixed plane of reflection and the ordinary plane of incidence is  $\alpha$ .

It follows from Figure (16) that the components of the incident electric field, parallel, and perpendicular to the edge-fixed plane of incidence can be expressed in the following way:

$$E_{\beta_0}^i = E_{\parallel}^i \cos \alpha - E_{\perp}^i \sin \alpha \quad (122)$$

$$E_{\phi}^i = E_{\parallel}^i \sin \alpha + E_{\perp}^i \cos \alpha \quad (123)$$

or in the more compact matrix notation

$$\bar{E}_{e.f.}^i = \bar{T}(-\alpha) \bar{E}^i \quad (124)$$

where

$$\bar{T}(-\alpha) = \begin{bmatrix} \cos \alpha & -\sin \alpha \\ \sin \alpha & \cos \alpha \end{bmatrix}. \quad (125)$$

Likewise, the components of the reflected field in the edge-fixed coordinate system can be expressed as

$$E_{\beta_0}^r = E_{\parallel}^r \cos \alpha + E_{\perp}^r \sin \alpha \quad (126)$$

$$E_{\phi}^r = -E_{\parallel}^r \sin \alpha + E_{\perp}^r \cos \alpha \quad (127)$$

or in matrix notation

$$\bar{E}_{e.f.}^r = T(\alpha) \bar{E}^r \quad (128)$$

where

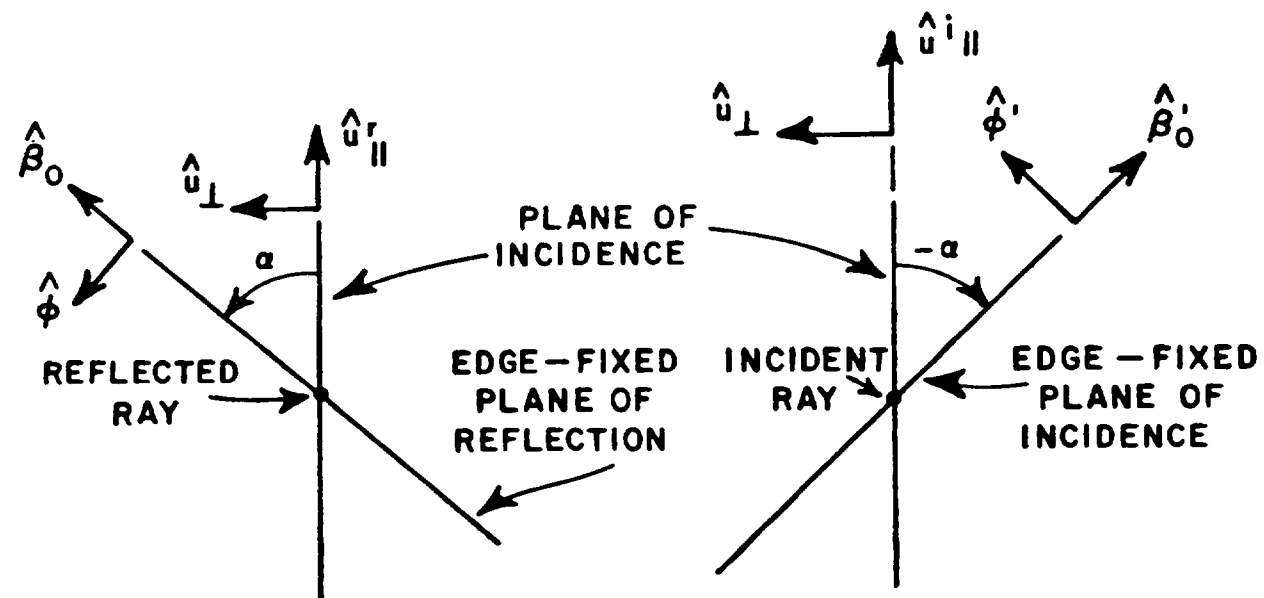


Figure 17. Comparison of the edge-fixed coordinate system and the ray fixed coordinate system. The incident and reflected rays are perpendicular to the page and directed outward.

$$T(\alpha) = \begin{bmatrix} \cos \alpha & \sin \alpha \\ -\sin \alpha & \cos \alpha \end{bmatrix} \quad (129)$$

In a manner analogous to the 2-D case, the diffracted field, which is valid for dielectric materials also can be expressed as

$$\begin{bmatrix} E_{\beta_0}^d \\ E_{\phi}^d \end{bmatrix} = \begin{bmatrix} \bar{A} D_0(\phi - \phi') + \bar{B} D_n(\phi - \phi') + \bar{C} D_0(\phi + \phi') \\ + \bar{D} D_n(\phi + \phi') \end{bmatrix} \begin{bmatrix} E_{\beta_0}^i \\ E_{\phi}^i \end{bmatrix} f_d(s), \text{ where } f_d(s) = \sqrt{\frac{\rho}{s(\rho+s)}} e^{-jks} \quad (130)$$

(131)

It has already been shown in Chapter III for the 2-D case, that the coefficients multiplying the D terms are proportional to the discontinuities of the geometrical optics field at the shadow and reflection boundaries. The same is true for the 3-D case, except that the coefficients are 2x2 matrices, which can be obtained by following the same procedure as in the 2-D case.

To find  $\bar{A}$ , one has to examine the  $\phi' + \pi$  shadow boundary (see Figure 13), where  $D_0(\phi - \phi')$  is the only term that is discontinuous. From Figure 16, it is easy to see that on the lit side of the  $\phi' + \pi$  boundary

$$\begin{bmatrix} E_{\beta_0}^i \\ E_{\phi}^i \end{bmatrix} = - \begin{bmatrix} E_{\beta_0'}^i \\ E_{\phi'}^i \end{bmatrix} \quad (132)$$

On the shadow side of the same boundary, the transmitted field is present. It follows that

$$\begin{bmatrix} E_{\beta_0}^t \\ E_{\phi}^t \end{bmatrix} = -\bar{T}(-\alpha) \begin{bmatrix} E_{\parallel}^t \\ E_{\perp}^t \end{bmatrix}, \quad (133)$$

but the transmitted field in the "ray-fixed" coordinate system can be expressed in terms of  $(E_{\beta_0}^i, E_{\phi}^i)$  as

$$\begin{bmatrix} E_{\parallel}^t \\ E_{\perp}^t \end{bmatrix} = \begin{bmatrix} T_{\parallel}^0 & 0 \\ 0 & T_{\perp}^0 \end{bmatrix} T^{-1}(-\alpha) \begin{bmatrix} E_{\beta_0}^i \\ E_{\phi}^i \end{bmatrix}. \quad (134)$$

Therefore  $(E_{\beta_0}^t, E_{\phi}^t)$  in terms of  $(E_{\beta_0}^i, E_{\phi}^i)$  is given by

$$\begin{bmatrix} E_{\beta_0}^t \\ E_{\phi}^t \end{bmatrix} = -T(-\alpha) \begin{bmatrix} T_{11} & 0 \\ 0 & T_{\perp} \end{bmatrix} T^{-1}(-\alpha) \begin{bmatrix} E_{\beta_0}^i \\ E_{\phi}^i \end{bmatrix}, \quad (135)$$

so the discontinuity at the  $\phi' + \pi$  boundary is equal to

$$\left\{ \begin{bmatrix} -1 & 0 \\ 0 & -1 \end{bmatrix} + \begin{bmatrix} \cos \alpha & -\sin \alpha \\ \sin \alpha & \cos \alpha \end{bmatrix} \begin{bmatrix} T_{11} & 0 \\ 0 & T_{\perp} \end{bmatrix} \begin{bmatrix} \cos \alpha & \sin \alpha \\ -\sin \alpha & \cos \alpha \end{bmatrix} \right\} \cdot \begin{bmatrix} E_{\beta_0}^i \\ E_{\phi}^i \end{bmatrix}, \quad (136)$$

thus,  $\bar{A}$  is given by

$$\bar{A} = \begin{bmatrix} -1 + T_{11}^0 \cos^2 \alpha + T_{\perp}^0 \sin^2 \alpha & (T_{11}^0 - T_{\perp}^0) \sin \alpha \cos \alpha \\ (T_{11}^0 - T_{\perp}^0) \sin \alpha \cos \alpha & -1 + T_{11}^0 \sin^2 \alpha + T_{\perp}^0 \cos^2 \alpha \end{bmatrix} \quad (137)$$

where the "o" superscript refers to the o-face of the wedge.

To find  $\bar{C}$ , one has to find the discontinuity at the  $(\pi - \phi')$  boundary, where  $D_{\phi}(\phi + \phi')$  is the only term that is discontinuous. On the lit side of the  $(\pi - \phi')$  boundary, the reflected field is expressed in the edge-fixed coordinate system by

$$\begin{bmatrix} E_{\beta_0}^r \\ E_{\phi}^r \end{bmatrix} = T(\alpha) \begin{bmatrix} R_{11}^0 & 0 \\ 0 & R_{\perp}^0 \end{bmatrix} T^{-1}(-\alpha) \begin{bmatrix} E_{\beta_0}^i \\ E_{\phi}^i \end{bmatrix}. \quad (138)$$

Therefore, the discontinuity is given by

$$\left\{ \begin{bmatrix} \cos \alpha & \sin \alpha \\ -\sin \alpha & \cos \alpha \end{bmatrix} \begin{bmatrix} R_{11}^0 & 0 \\ 0 & R_{\perp}^0 \end{bmatrix} \begin{bmatrix} \cos \alpha & \sin \alpha \\ -\sin \alpha & \cos \alpha \end{bmatrix} \right\} \begin{bmatrix} E_{\beta_0}^i \\ E_{\phi}^i \end{bmatrix} \quad (139)$$

which implies that



$$\bar{C} = \begin{bmatrix} R_{||}^0 \cos^2 \alpha - R_{\perp}^0 \sin^2 \alpha & (R_{||}^0 + R_{\perp}^0) \sin \alpha \cos \alpha \\ -(R_{||}^0 + R_{\perp}^0) \sin \alpha \cos \alpha & -R_{||}^0 \sin^2 \alpha + R_{\perp}^0 \cos^2 \alpha \end{bmatrix} \quad (140)$$

Exactly the same procedure must be followed to find  $\bar{B}$  and  $\bar{D}$ . That is, finding the discontinuities at the  $(\psi' - \pi)$  and  $(2n-1)\pi - \psi'$  boundaries, where  $D_n(\phi - \phi')$  and  $D_n(\phi + \phi')$  happen to be discontinuous, respectively. It follows that

$$\bar{B} = \begin{bmatrix} -1 + T_{||}^n \cos^2 \alpha + T_{\perp}^n \sin^2 \alpha & (T_{||}^n - T_{\perp}^n) \sin \alpha \cos \alpha \\ (T_{||}^n - T_{\perp}^n) \sin \alpha \cos \alpha & -1 + T_{||}^n \sin^2 \alpha + T_{\perp}^n \cos^2 \alpha \end{bmatrix} \quad (141)$$

and

$$\bar{D} = \begin{bmatrix} R_{||}^n \cos^2 \alpha - R_{\perp}^n \sin^2 \alpha & (R_{||}^n + R_{\perp}^n) \sin \alpha \cos \alpha \\ -(R_{||}^n + R_{\perp}^n) \sin \alpha \cos \alpha & -R_{||}^n \sin^2 \alpha + R_{\perp}^n \cos^2 \alpha \end{bmatrix}, \quad (142)$$

where the superscript "n" refers to the  $n\pi$ -face of the wedge.

The 3-D diffracted field can be written in matrix form as

$$\begin{bmatrix} E_{\beta 0}^d \\ E_{\phi}^d \end{bmatrix} = \begin{bmatrix} -D_a & -D_b \\ -D_c & -D_d \end{bmatrix} \begin{bmatrix} E_{\beta 0}^i \\ E_{\phi}^i \end{bmatrix} \sqrt{\frac{\rho}{s(\rho+s)}} e^{-jks} \quad (143)$$

where

$$D_a = [1 - T_{||}^0 \cos^2 \alpha - T_{\perp}^0 \sin^2 \alpha] D_0(\phi - \phi') + [1 - T_{||}^n \cos^2 \alpha - T_{\perp}^n \sin^2 \alpha] \times \\ D_n(\phi - \phi') + [-R_{||}^0 \cos^2 \alpha + R_{\perp}^0 \sin^2 \alpha] D_0(\phi + \phi') + [-R_{||}^n \cos^2 \alpha + \\ R_{\perp}^n \sin^2 \alpha] D_n(\phi + \phi') \quad (144)$$

$$D_b = [T_{\perp}^0 - T_{||}^0] \sin \alpha \cos \alpha D_0(\phi - \phi') + [T_{\perp}^n - T_{||}^n] \sin \alpha \cos \alpha D_n(\phi - \phi') \\ + [-R_{||}^0 - R_{\perp}^0] \sin \alpha \cos \alpha D_0(\phi + \phi') + [-R_{||}^n - R_{\perp}^n] \sin \alpha \cos \alpha \times \\ D_n(\phi + \phi') \quad (145)$$

$$D_c = [-T_{||}^0 + T_{\perp}^0] \sin \alpha \cos \alpha D_o(\phi - \phi') + [-T_{||}^n + T_{\perp}^n] \sin \alpha \cos \alpha D_n(\phi - \phi') \\ + [R_{||}^0 + R_{\perp}^0] \sin \alpha \cos \alpha D_o(\phi + \phi') + [R_{||}^n + R_{\perp}^n] \sin \alpha \cos \alpha D_n(\phi + \phi') \quad (146)$$

$$D_d = [1 - T_{||}^0 \sin^2 \alpha - T_{\perp}^0 \cos^2 \alpha] D_o(\phi - \phi') + [1 - T_{||}^n \sin^2 \alpha - T_{\perp}^n \cos^2 \alpha] \times \\ D_n(\phi - \phi') + [R_{||}^0 \sin^2 \alpha - R_{\perp}^0 \cos^2 \alpha] D_o(\phi + \phi') + [R_{||}^n \sin^2 \alpha - \\ R_{\perp}^n \cos^2 \alpha] D_n(\phi + \phi') \quad (147)$$

The diffracted field can, also, be expressed in a more compact notation as

$$\bar{E}_{(s)}^d = \bar{E}^i(Q \cdot E) \cdot \bar{D}(\phi', \phi; \beta'_0) \sqrt{\frac{\rho}{s(\rho + s)}} e^{-jks} \quad (148)$$

where

$$\bar{D}(\phi', \phi; \beta'_0) = -\hat{\beta}'_0 \hat{\beta}_0 D_a - \hat{\phi}' \hat{\beta}_0 D_b - \hat{\beta}'_0 \hat{\phi} D_c - \hat{\phi}' \hat{\phi} D_d \quad (149)$$

Note that for the dielectric case, the dyadic diffraction coefficient is equal to the sum of four dyads, but it reduces to dyadic form for the perfectly-conducting wedge. That is, for the perfectly-conducting case

$$D_b = D_c = 0 \quad (150)$$

## CHAPTER V

### CURVED SURFACE DIFFRACTION

It has been mentioned before that in certain cases surface rays are excited along the surface of convex bodies as depicted in Figure 18.

These rays can be determined using the generalized Fermat's principle. According to this principle, a ray emanating from a point source makes the optical distance between the source and observation points an extremum. Thus, if the ray path lies on a smooth surface, it follows a geodesic path on the surface and continually sheds energy into the shadow region.

Surface rays, which are also referred to as creeping waves, can be excited by sources which are located either on or off a smooth convex surface, or by the illumination of an edge or other geometrical or electrical discontinuity in an otherwise smooth convex surface.

Because of its many applications in practical problems, such as the radiation of antennas mounted on convex surfaces, the case when the source lies on the surface of a convex body is a very important problem. The surface is assumed to be perfectly conducting, as shown in Figure 19.

A plane tangent to the surface at the source point divides the region in two parts; the lit region and shadow regions. This plane is referred to as the shadow boundary. The field in the deep lit region is essentially obtained from geometrical optics, and the field in the deep shadow region is relatively weak, leaving the fields in the region adjacent to the shadow boundary a most interesting case.

#### A. Lit Region

From Fermat's principle, the source  $d\vec{P}_m(Q')$  excites waves which propagate along straight line ray paths from the source to field point in the lit region as depicted in Figure 20.  $d\vec{P}_m(Q')$  is an infinitesimal magnetic moment, and  $d\vec{P}_e(Q')$  an infinitesimal current moment, where

$$d\vec{P}_m(Q') = \vec{E}(Q') \times \hat{n}' da' \quad (151)$$

$$d\vec{P}_e(Q') = I(\ell') d\ell' \hat{n}' \quad (152)$$

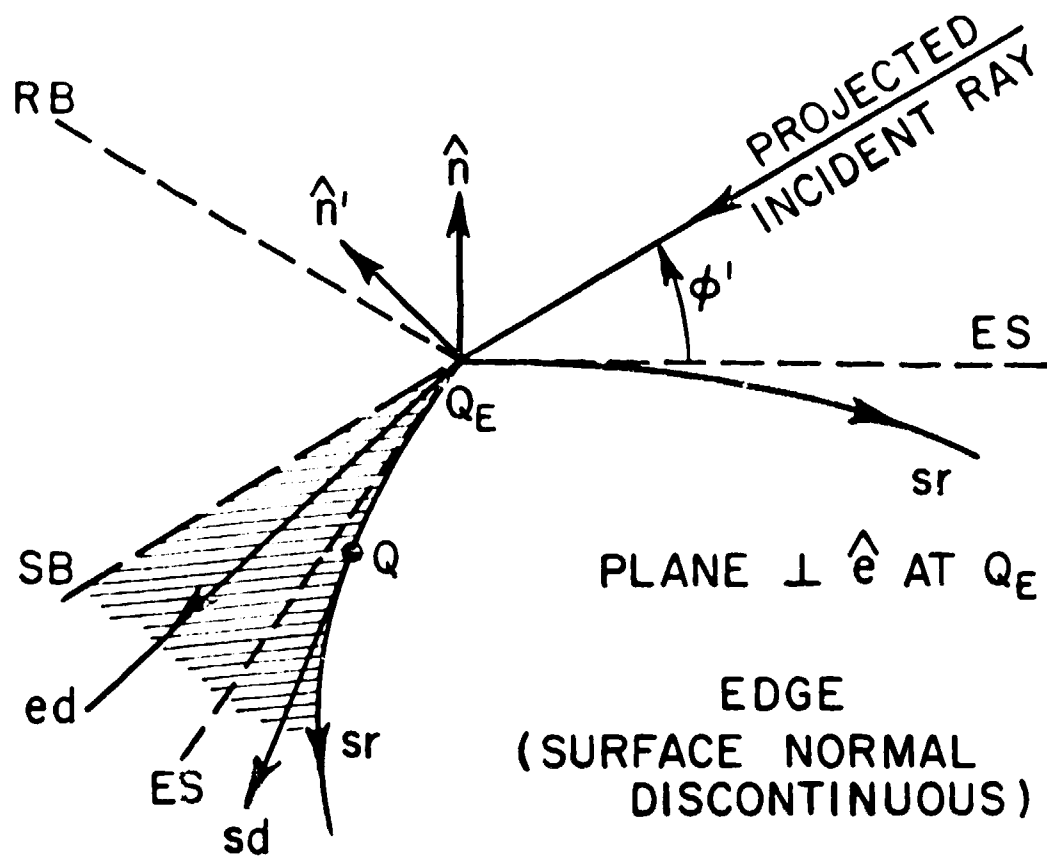


Figure 18. Surface diffracted field SD. ES refers to the surface of the wedge.

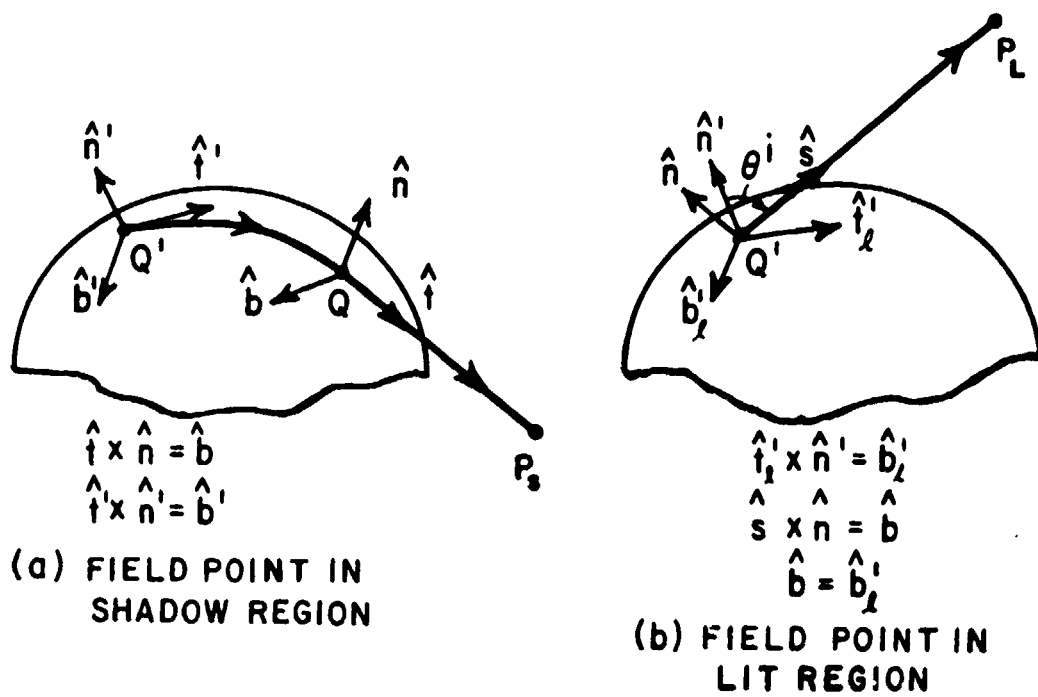
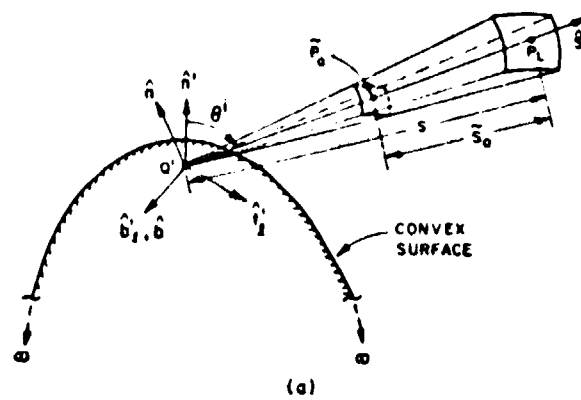


Figure 19. Ray paths in the lit and shadow regions.



$$\begin{aligned}
 \hat{n}' \cdot \hat{s} &= \cos \theta^i \\
 \hat{s} &= \hat{n}' \cos \theta^i + \hat{t}'_i \sin \theta^i \\
 \hat{b}'_i &= \hat{t}'_i \times \hat{n}' = \hat{b} = \hat{s} \times \hat{n}
 \end{aligned}$$

(b)

Figure 20. Ray path and coordinate system for lit region.

$\vec{E}(Q')$  is the electric field at  $Q'$ ,  $\hat{n}$  the outward unit surface normal at  $Q'$ , and  $da'$  the area element at  $Q'$ .  $I(\ell')$  represents the electric current distribution on the monopole, and  $\ell'$  is the distance parameter along the monopole.

The field due to this source ( $d\vec{P}_m(Q')$ ) at point  $P_L$  is [9]

$$d\vec{E}_m(P_L) = d\vec{E}_m(\tilde{P}_0) \left[ \frac{\rho_1^i \rho_2^i}{(\tilde{s}_0 + \rho_1^i)(\tilde{s}_0 + \rho_2^i)} \right]^{1/2} e^{-jk\tilde{s}_0} + O[m_\ell^{-2}, m_\ell^{-3}] \quad (153)$$

Note that  $Q'$  is the only caustic of the incident rays, so  $\rho_1^i$  and  $\rho_2^i$  (the principal radii of curvature of the incident field wave-front) are identical, i.e.,  $\rho_1^i = \rho_2^i = \rho^i$ .  $O[m_\ell^{-2}, m_\ell^{-3}, \dots]$  are higher order terms which may be neglected in most cases.

Since  $d\vec{E}_m(P_L)$  is independent of the reference point  $\tilde{P}_0$ ,  $\tilde{P}_0$  can be chosen to be at  $Q'$ , and it follows that

$$\lim_{\substack{\tilde{P}_0 \rightarrow Q' \\ \rho_i \rightarrow 0 \\ \tilde{s}_0 \sim s}} \rho^i d\vec{E}_m(\tilde{P}_0) = \vec{L}_m^\ell \text{ should exist} \quad (154)$$

It is shown in [9] that  $\vec{L}_m^\ell$  can be related to  $d\vec{P}_m(Q')$  by

$$\vec{L}_m^\ell = d\vec{P}_m(Q') \cdot \vec{T}_m^\ell \quad (155)$$

Combining equations (153), (154), and (155)

$$d\vec{E}_m(P_L) = d\vec{P}_m(Q') \cdot \vec{T}_m^\ell \frac{e^{-jks}}{s} + O[m_\ell^{-2}, m_\ell^{-3}, \dots], \quad (156)$$

where

$$\vec{T}_m = -\frac{jk}{4\pi} [\hat{b}_\ell' \hat{n} A + \hat{t}_\ell' \hat{b} B + \hat{b}_\ell' \hat{b} C + \hat{t}_\ell' \hat{n} D], \quad (157)$$

and

$$\vec{T}_e = -\frac{jkZ_0}{4\pi} [\hat{n}' \hat{n} M + \hat{n}' \hat{b} N]. \quad (158)$$

The coefficients A, B, C, D, M and N are defined in Table II, and  $Z_0$  is the free space wave impedance.

The  $\hat{n}$  component of the  $d\vec{E}$  field for the magnetic source case ( $d\vec{P}_m(Q')$ ) is

TABLE II  
Lit Region

Slot or $dP_m$ case				Monopole or $dP_e$ case		$T_0$	F
A	B	C	D	M	N		
$H^2 + T_0^2 F \cos^2 \theta^i$	$s^2 - T_0^2 F \cos^2 \theta^i$	$T_0 F$	$T_0 F \cos \theta^i$	$\sin \theta^i [H^2 + T_0^2 F \cos^2 \theta^i]$	$\sin \theta^i T_0 F$	$T(Q') \rho_g(Q')$	$\frac{s^2 - H^2 \cos^2 \theta^i}{1 + T_0^2 \cos^2 \theta^i}$



$$dE_m^n(P_L) = \frac{-jk}{4\pi} [ (d\vec{P}_m(Q') \cdot \hat{b}') (H^\ell + T_0^2 F \cos \theta^i) + (d\vec{P}_m(Q') \cdot \hat{t}') T_0 F \cos \theta^i ] \cdot \frac{e^{-jks}}{s} + O[m_\ell^{-2}, m_\ell^{-3}, \dots] \quad (159)$$

and for the electric source case ( $d\vec{P}_e(Q')$ )

$$dE_e^n(P_L) = \frac{-jkZ_0}{4\pi} dP_e(Q') \sin \theta^i [ H^\ell + T_0^2 F \cos \theta^i ] \frac{e^{-jks}}{s} + O[m^{-2}, m^{-3}, \dots] \quad (160)$$

Likewise, the  $\hat{b}$  component of  $d\vec{E}$  for the magnetic source  $d\vec{P}_m(Q')$  case is

$$dE_m^b(P_L) = \frac{-jk}{4\pi} [ (d\vec{P}_m(Q') \cdot \hat{b}') T_0 F + (d\vec{P}_m(Q') \cdot \hat{t}') \times (s^\ell - T_0^2 F \cos^2 \theta^i) ] \times \frac{e^{-jks}}{s} + O[m_\ell^{-2}, m_\ell^{-3}, \dots] \quad (161)$$

and for the electric source  $d\vec{P}_e(Q')$

$$dE_e^b(P_L) = \frac{-jkZ_0}{4\pi} dP_e(Q') \sin \theta^i T_0 F \frac{e^{-jks}}{s} + O[m_\ell^{-2}, m_\ell^{-3}, \dots] \quad (162)$$

where

$$H^\ell = g(\xi_\ell) e^{-jk\xi_\ell^3/3} \quad (163)$$

$$S^\ell = \frac{-j}{m_\ell(Q')} \hat{g}(\xi_\ell) e^{-j\xi_\ell^3/3} \quad (164)$$

and

$$F = \frac{S^\ell - H^\ell \cos \theta^i}{1 + T_0^2 \cos^2 \theta^i} \quad (165)$$

The angle  $\theta^i$  is defined by  $\hat{n} \cdot \hat{s} = \cos \theta^i$  as shown in Figure 20. Further,

$$g(\xi) = \frac{1}{\sqrt{\pi}} \int_{-\infty}^{\infty} \exp[-j\frac{2\pi}{3}\tau] d\tau \cdot \frac{\exp(-j\tau\xi)}{w_2'(\tau)} \quad (166)$$

and

$$\hat{g}(\xi) = \frac{1}{\sqrt{\pi}} \int_{-\infty}^{\infty} d\tau \frac{\exp(-j\tau\xi)}{\exp[-j\frac{2\pi}{3}w'(\tau)]}, \quad (167)$$

where  $g(\xi)$  and  $\hat{g}(\xi)$  are known as the acoustic hard and soft Fock functions, respectively. The Fock type Airy function is given by

$$w_2(\tau) = \frac{1}{\sqrt{\pi}} \int_{-\infty}^{\infty} d\tau e^{[\tau\tau - t^3/3]} \exp[j\frac{2\pi}{3}] \quad (168)$$

and  $w'_2(\tau)$  is the derivative of  $w_2(\tau)$  with respect to  $\tau$ . The Fock parameter for the lit region is

$$\xi_\ell = -m_\ell(Q') \cos \theta^i \quad (169)$$

with

$$m_\ell(Q') = \frac{m(Q')}{(1 + T_0^2 \cos^2 \theta^i)^{1/3}}, \quad (170)$$

and

$$m(t') = \left[ \frac{k \rho_g(t')}{2} \right]^{1/3}, \quad (171)$$

where  $m(Q')$  is equal to  $m(t')$  evaluated at  $t'=Q'$ . Here  $\rho_g(t')$  is the surface radius of curvature along the ray path at  $t'$ .

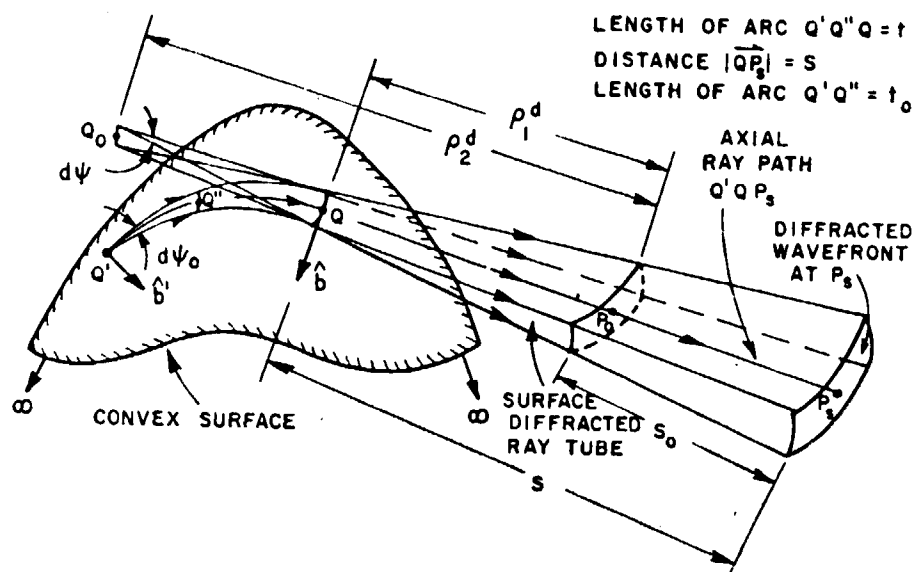
### B. Shadow Region

Surface rays in the shadow region are illustrated in Figure 21. According to the generalized Fermat's principle, a ray emanating from the source  $dP_m(Q')$  at  $Q'$  propagates along a geodesic path  $Q'Q$  on the surface and toward the observation point along the geodesic tangent at  $Q$ .

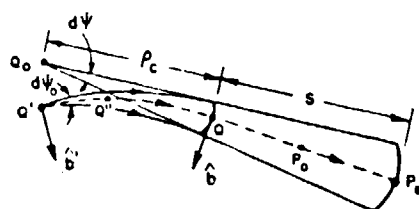
The field  $d\bar{E}_m$  at  $P_s$  is [9]

$$d\bar{E}_m(P_s) = d\bar{E}_m(P_0) \left[ \frac{\rho_1 d\rho_1 d\rho_2}{(s_0 + \rho_1)(s_0 + \rho_2)} \right]^{1/2} e^{-jks_0} + O[m^{-2}, m^{-3}, \dots] \quad (172)$$

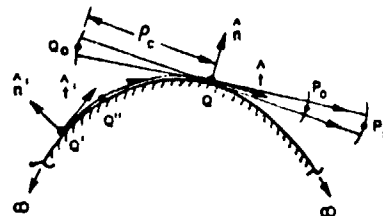
where  $P_0$  is the reference point, and  $\rho_1, \rho_2$  are the principal radii of curvature of the wavefront.



(a) Perspective view of a surface diffracted ray tube.



(b) Top view of a diffracted ray tube indicating the divergence of the rays and the unit binormal vectors at  $Q'$  and  $Q$ .



(c) Side view of a surface diffracted ray tube and the unit normal and tangent vectors at  $Q'$  and  $Q$ .

Figure 21. Surface diffracted ray tube and ray coordinates for the shadow region.

Again, as in the lit region,  $d\bar{E}_m(P_s)$  is independent of the reference point  $P_0$ , where  $P_0$  is an arbitrary point. It is common to let  $P_0$  be at the diffraction point  $Q$ , then  $\rho_1 \rightarrow 0$ ,  $\rho_2 \rightarrow \rho_c$  and  $s_0 \rightarrow 0$ .

It follows that

$$\lim_{\substack{P_0 \rightarrow Q \\ \rho_1 \rightarrow 0 \\ \rho_2 \rightarrow \rho_c}} \sqrt{\frac{d}{\rho_1}} d\bar{E}_m(P_0) = \bar{L}_m(Q', Q) \quad (173)$$

then

$$d\bar{E}_m(P_s) = \bar{L}_m(Q', Q) \left[ \frac{\rho_c}{s(\rho_c + s)} \right]^{1/2} e^{-jks} + O[m^{-2}, m^{-3}, \dots] \quad (174)$$

Since one is dealing with a linear phenomenon,  $\bar{L}_m$  can be related to the source strength  $d\bar{P}_m$  at  $Q'$  by

$$\bar{L}_m(Q', Q) = d\bar{P}_m(Q', Q) \cdot \bar{T}_m(Q', Q) \quad (175)$$

where  $\bar{T}_m(Q', Q)$  is given by [9]

$$\begin{aligned} \bar{T}_m(Q', Q) = & \frac{-jk}{4\pi} [\hat{b}' \hat{n} T_1(Q') H + \hat{t}' \hat{b} T_2(Q') S + \hat{b}' \hat{b} T_3(Q') S \\ & + \hat{t}' \hat{n} T_4(Q') H] e^{-jkt} \times \left[ \frac{d\psi_0}{dn(Q)} \right]^{1/2} \left[ \frac{\rho_d(Q)}{\rho_g(Q')} \right]^{1/6} \end{aligned} \quad (176)$$

$$\begin{aligned} \bar{T}_e(Q', Q) = & \frac{-jkZ_0}{4\pi} [\hat{n}' \hat{n} T_5(Q') H + \hat{n}' \hat{b} T_6(Q') S] e^{-jkt} \times \\ & \left[ \frac{d\psi_0}{dn(Q)} \right]^{1/2} \left[ \frac{\rho_d(Q)}{\rho_g(Q')} \right]^{1/6} \end{aligned} \quad (177)$$

As illustrated in Figure 19a, there is an orthonormal basis at each point on the surface. Note that  $(\hat{t}', \hat{n}', \hat{b}')$  and  $(\hat{t}, \hat{n}, \hat{b})$  are the tangent, normal and binormal unit vectors to the surface at the source point  $(Q')$  and diffraction point  $(Q)$ , respectively. The components of the two orthonormal sets are related by

$$\hat{t} \times \hat{n} = \hat{b} \quad \hat{t}' \times \hat{n}' = \hat{b}' \quad (178)$$

The quantities  $T_1(Q')$ ,  $T_2(Q')$ , ...,  $T_6(Q')$  in Equations (176) and (177) are the torsion factors and are given in Table III.

TABLE III  
Shadow Region

TYPE OF CONVEX SURFACE	SLOT OR $d\bar{p}_m$ CASE				MONOPOLE OR $d\bar{p}_0$ CASE		SURFACE RAY TORSION $T(Q')$	SURFACE RADIUS OF CURVATURE IN $\hat{t}_1$ DIRECTION $\rho_0(Q')$	SURFACE DIFFRACTED RAY CAUSTIC DISTANCE $\rho_c$
	$T_1(Q')$	$T_2(Q')$	$T_3(Q')$	$T_4(Q')$	$T_5(Q')$	$T_6(Q')$			
SPHERE	1	1	0	0	1	0	0	a	$a \tan\left(\frac{\pi}{2}\right)$
CIRCULAR CYLINDER	1	1	$\frac{\sin 2\alpha'}{2a} + \frac{0}{\sin^2 \alpha'}$	0	1	$\frac{\sin 2\alpha'}{2a} + \frac{0}{\sin^2 \alpha'}$	$\frac{\sin 2\alpha'}{2a}$	$\frac{0}{\sin^2 \alpha'}$	1
ARBITRARY CONVEX SURFACE	1	1	$T_1(Q')\rho_0(Q')$	0	1	$T_1(Q')\rho_0(Q')$	$\frac{\sin 2\alpha'}{2} \left( \frac{1}{R_1(Q')} - \frac{1}{R_2(Q')} \right)$ WITH $R_1(Q') \geq R_2(Q')$	$\left( \frac{\cos^2 \alpha'}{R_1(Q')} + \frac{\sin^2 \alpha'}{R_2(Q')} \right)^{-1}$	$\frac{2\sqrt{E} \cdot 0}{\partial \theta / \partial \theta'}$

- NOTE: 1.  $\alpha'$  is defined by  $\hat{t}_1 \cdot \hat{t}' = \cos \alpha'$  where  $\hat{t}_1$  is the principal direction unit vector associated with  $R_1(Q')$ .
2. The quantities E and G denote two of the three coefficients E, F, G that appear in the "first fundamental form" of Differential Geometry.

ORIGINAL PAGE  
OF POOR QUALITY

Further,

$$H = g(\xi) \quad \text{and} \quad (179)$$

$$S = \frac{-j}{m(Q')} \hat{g}(\xi) \quad (180)$$

The Fock parameter  $\xi$  for the shadow region is given in [17] as

$$\xi = \int_{Q'}^Q \frac{m(t')}{\rho_g(t')} dt' \quad (181)$$

where  $t$  is the geodesic arc length from  $Q'$  to  $Q$ . The width of the surface ray tube at  $Q, dn(Q)$  is given by

$$dn(Q) = \rho_c d\psi \quad (182)$$

Combining Equations (174)-(177) one obtains for the  $d\bar{P}_m(Q')$  case

$$dE_m^n(P_S) = \frac{-jk}{4\pi} (d\bar{P}_m(Q') \cdot \hat{b}') H e^{-jkt} \left[ \frac{\rho_g(Q')}{\rho_g(Q)} \right]^{-1/6} \left[ \frac{d\psi_0}{d\psi} \right]^{1/2} \times$$

$$\left[ \frac{1}{s(s+\rho_c)} \right]^{1/2} e^{-jks} + O[m^{-2}, m^{-3}, \dots] \quad (183)$$

$$dE_m^b(P_S) = \frac{-jk}{4\pi} \left[ (d\bar{P}_m(Q') \cdot \hat{b}') T_0 S + (d\bar{P}_m(Q') \cdot \hat{t}') S \right] e^{-jkt} \times$$

$$\left[ \frac{\rho_g(Q')}{\rho_g(Q)} \right]^{-1/6} \left[ \frac{d\psi_0}{d\psi} \right]^{1/2} \times \left[ \frac{1}{s(\rho_c+s)} \right]^{1/2} e^{-jks} +$$

$$O[m^{-2}, m^{-3}, \dots] \quad (184)$$

and for the  $d\bar{P}_e(Q')$  case

$$dE_e^n(P_S) = \frac{-jkZ_0}{4\pi} dP_e(Q') H e^{-jkt} \left[ \frac{\rho_g(Q')}{\rho_g(Q)} \right]^{-1/6} \left[ \frac{d\psi_0}{d\psi} \right]^{1/2} \times$$

$$\left[ \frac{1}{s(s+\rho_c)} \right]^{1/2} e^{-jks} + O[m^{-2}, m^{-3}, \dots]$$

$$dE_e^b(P_S) = \frac{-jkZ_0}{4\pi} dP_e(Q') T_0 S e^{-jkt} \left[ \frac{\rho_g(Q')}{\rho_g(Q)} \right]^{-1/6} \left[ \frac{d\psi_0}{d\psi} \right]^{1/2} \times$$

$$\left[ \frac{1}{s(s+\rho_c)} \right]^{1/2} e^{-jks} + O[m^{-2}, m^{-3}, \dots] \quad , \quad (185)$$

where

$$T_0 = T(Q') \rho_g(Q') \quad (186)$$

with  $T(Q')$  being the surface torsion at the source location. Expressions for  $T(Q')$  are given in Table III.

The formulas given for surfaces rays are of interest, because of the many practical problems where the fields radiated from antennas mounted on convex surfaces need to be calculated.

Of particular interest is the prolate spheroid, because this shape is used to model objects like the fuselage of an aircraft, the mast of a ship, etc. Because the solution in the lit region is straightforward, the most critical aspect of this kind of problem, is the calculation of the geodesic paths associated with the UTD solution in the shadow region. In [10] efficient numerical algorithms are examined, where the spheroid is simulated by a perturbed cone or cylinder model depending on the location of the source. When the source is at the center of the spheroid, a cylinder model is used, and when the source is off the center, a cone model is used.

Because the cone and cylinder are developed surfaces, it is easy to find the geodesic path for a given radiation direction  $(\theta_t, \phi_t)$ . Assuming that a new radiation direction does not differ much from the previous direction, this method uses the properties of the surface, and the previous geodesic path to find the new diffraction point. This approach decreases the amount of computer time needed to calculate the diffraction points, and geodesic paths, making it a very efficient and accurate solution for the radiation problem.

## CHAPTER VI

### RADIATION PATTERN OF AN ANTENNA MOUNTED ON A CONVEX BODY IN THE PRESENCE OF A DIELECTRIC SLAB

Many structures such as aircraft, ships, etc., can be modeled using flat plates and some kind of convex body such as a cylinder, sphere, spheroid, etc. The radiating system shown in Figure 1 is a good starting point in solving more complicated structures in that it makes use of all the results given up to this point.

As illustrated in Figure 1, consider the antenna mounted on a perfectly conducting convex surface in the presence of an  $n$ -sided finite flat dielectric slab, which in general can have some loss. In order to avoid some geometric complications, let us assume that the dielectric slab is not attached to the convex surface.

The total field at point( $p$ ), which has to be at least a wavelength away from any diffraction point is equal to the superposition of the following field components as depicted in Figure 22.

- (1) direct field from the source
- (2) reflected fields from the finite dielectric slab
- (3) transmitted fields through the finite dielectric slab
- (4) curved surface diffracted fields from the convex surface
- (5) diffracted fields from the edges of the slab
- (6) vertex diffraction from each of the slab corners.

It is convenient to first examine the radiation from the antenna without the presence of the slab. According to Geometrical Optics, the region external to the convex surface is divided into lit and shadow regions by a plane tangent to the surface at  $Q'$ . This plane is referred to as the shadow boundary, and the region adjacent to this plane is known as the transition region.

Consider two types of antennas: slots and monopoles on a convex surface. The expressions for  $dE_{\theta}$  that were given in Chapter V are valid for infinitesimal slot and monopole antennas mounted on an arbitrary perfectly conducting convex surface. They were obtained by generalizing the solutions for a circular cylinder. That is justified on the basis of the locality of the high-frequency propagation which is one of Keller's postulates. The generalization is necessary and very useful in analyzing complicated structures.



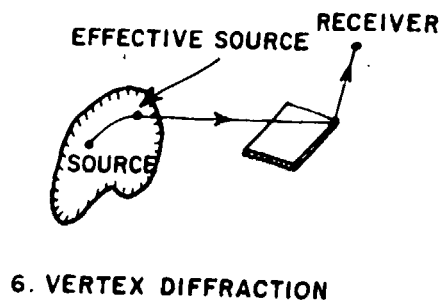
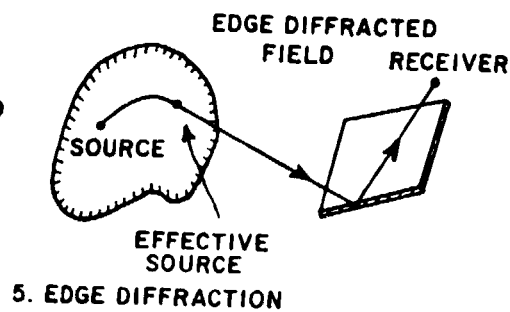
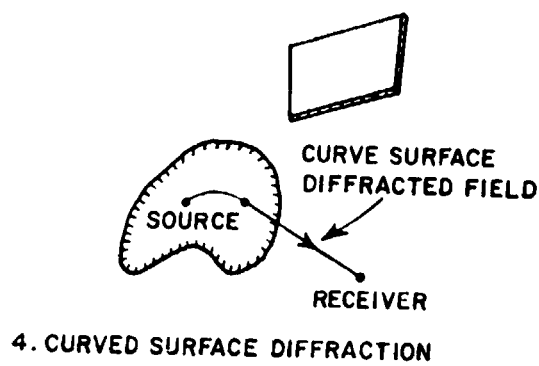
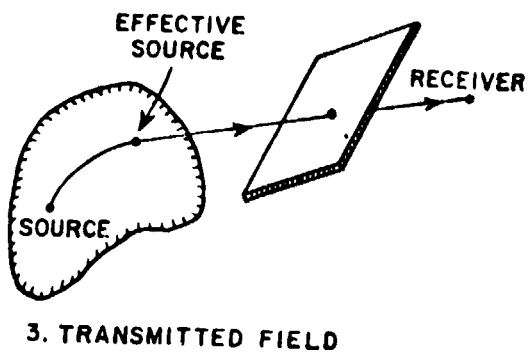
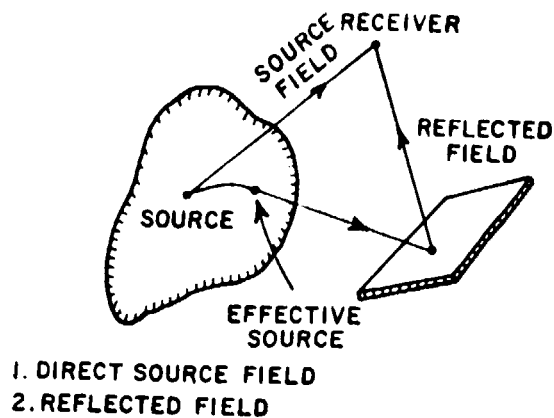


Figure 22. Various terms used in calculating the total high-frequency field.

### A. Pattern Factors

There are several ways of extending the expressions of Chapter V to cases where the slots are not infinitesimal. One approach is to integrate the short-slot solutions over the source distribution if it's known. This is based on the superposition theorem, and one can approximate the source distribution by an array of short magnetic dipoles on the conducting surface.

A more efficient approach is to modify the short-slot solutions as indicated in [12] and [13], where the results for the aperture problem are obtained by multiplying the short-slot solution by an appropriate pattern factor. The solution for the monopole antenna can be found using the reciprocity theorem and the equation of continuity for the slot case, as shown in [12] and [13].

The pattern factors were obtained by assuming that the slot aperture on the convex surface could be approximated by a slot on a flat plate. This implies that the dimensions of the slot have to be very small in relation to the radii of curvature of the convex surface. The pattern factors for an arbitrary convex surface are [10]

(a) for the shadow region

$$\bar{P}_m^s = P_m \frac{2B}{\pi} \left[ \frac{\cos(\frac{kB}{2}(\hat{P}_m \cdot \hat{t}'))}{1 - (\frac{kB}{\pi}(\hat{P}_m \cdot \hat{t}'))^2} \right] \left[ \frac{\sin(\frac{kA}{2}(\hat{P}_m \cdot \hat{b}'))}{\frac{kA}{2} \hat{P}_m \cdot \hat{b}'} \right] \quad (187)$$

$$\bar{P}_e^s = \hat{n}' [1 - \cos(kL)] \quad (188)$$

(b) for the lit region

$$\bar{P}_m^l = \hat{P}_m \frac{2B}{\pi} \left[ \frac{\cos(\frac{kB}{2} \sin \theta^i (\hat{P}_m \cdot \hat{t}'))}{1 - (\frac{kB}{\pi} \sin \theta^i (\hat{P}_m \cdot \hat{t}'))^2} \right] \left[ \frac{\sin(\frac{kA}{2} \sin \theta^i (\hat{P}_m \cdot \hat{b}'))}{\frac{kA}{2} \sin \theta^i (\hat{P}_m \cdot \hat{b}')} \right] \quad (189)$$

$$\bar{P}_e^l = \hat{n}' \frac{\cos(kL \hat{n}' \cdot \hat{s}) - \cos(kL)}{1 - (\hat{n}' \cdot \hat{s})^2} \quad (190)$$

$\hat{P}_m$  = unit vector in the direction of magnetic current moment

A, B = length of the short and long sides of the slot, respectively.

It is assumed that a cosine distribution exists along the B dimension and a uniform distribution along the A dimension.

$L$  = length of the monopole, which is not to exceed a quarter wavelength. All the other variables were defined before.

Thus, by replacing  $d\vec{P}_e$  in Equations (159)-(162) and (183)-(185) in Chapter V by the pattern factors just given, one obtains expressions for the fields due to aperture and monopole antennas on a convex surface:

#### Lit Region

(a)  $\vec{P}_m^L$  (slot)

$$E_m^n(P_L) = \frac{-jk}{4\pi} \left[ (\vec{P}_m^L \cdot \hat{b}') (H^L + T_0^2 F \cos \theta^i) + (\vec{P}_m^L \cdot \hat{t}') T_0 F \cos \theta^i \right] \frac{e^{-jks}}{s} + O[m_\lambda^{-2}, m_\lambda^{-3}, \dots] \quad (191)$$

$$E_m^b(P_L) = \frac{-jk}{4\pi} \left[ (\vec{P}_m^L \cdot \hat{b}') T_0 F + (\vec{P}_m^L \cdot \hat{t}') (S^L - T_0^2 F \cos^2 \theta^i) \right] \frac{e^{-jks}}{s} + O[m_\lambda^{-2}, m_\lambda^{-3}, \dots] \quad (192)$$

(b)  $\vec{P}_e^L$  (monopole)

$$E_e^n(P_L) = \frac{-jkZ_0}{4\pi} \left[ (\vec{P}_e^L \cdot \hat{n}') \sin \theta^i (H^L + T_0^2 F \cos \theta^i) \right] \frac{e^{-jks}}{s} + O[m_\lambda^{-2}, m_\lambda^{-3}, \dots] \quad (193)$$

$$E_e^b(P_L) = \frac{-jkZ_0}{4\pi} (\vec{P}_e^L \cdot \hat{n}') \sin \theta^i T_0 F \frac{e^{-jks}}{s} + O[m_\lambda^{-2}, m_\lambda^{-3}, \dots] \quad (194)$$

#### Shadow Region

(a)  $\vec{P}_m^S$  (slot)

$$E_m^n(P_S) = \frac{-jk}{4\pi} (\vec{P}_m^S \cdot \hat{b}') H e^{-jkt} \left[ \frac{\rho_g(Q')}{\rho_g(Q)} \right]^{-1/6} \left[ \frac{d\psi_0}{d\psi} \right]^{1/2} \times \left[ \frac{1}{s(\rho_c + s)} \right]^{1/2} e^{-jks} + O[m^{-2}, m^{-3}, \dots] \quad (195)$$

$$E_m^b(p_s) = \frac{-jk}{4\pi} \left[ (\bar{p}_m^s \cdot \hat{b}') T_0 S + (\bar{p}_m^s \cdot \hat{t}') S \right] e^{-jkt} \left[ \frac{\rho_g(Q')}{\rho_g(Q)} \right]^{-1/6} \times \\ \left[ \frac{d\psi_0}{d\psi} \right]^{1/2} \left[ \frac{1}{s(\rho_c + s)} \right]^{1/2} e^{-jks} + O[m^{-2}, m^{-3}, \dots] \quad (196)$$

(b)  $\bar{p}_e^s$  (monopole)

$$E_e^h(p_s) = \frac{-jkZ_0}{4\pi} (\bar{p}_e^s \cdot \hat{n}') H e^{-jkt} \left[ \frac{\rho_g(Q')}{\rho_g(Q)} \right]^{-1/6} \left[ \frac{d\psi_0}{d\psi} \right]^{1/2} \times \\ \left[ \frac{1}{s(\rho_c + s)} \right]^{1/2} e^{-jks} + O[m^{-2}, m^{-3}, \dots] \quad (197)$$

$$E_e^b(p_s) = \frac{-jkZ_0}{4\pi} (\bar{p}_e^s \cdot \hat{n}') T_0 S e^{-jkt} \left[ \frac{\rho_g(Q')}{\rho_g(Q)} \right]^{-1/6} \left[ \frac{d\psi_0}{d\psi} \right]^{1/2} \times \\ \left[ \frac{1}{s(\rho_c + s)} \right]^{1/2} e^{-jks} + O[m^{-2}, m^{-3}, \dots] \quad (198)$$

The first step in the solution of each term of the total GTD field is to determine the ray path using the law of reflection or/and diffraction. Assuming the ray path is determined, one must then examine the total ray path, to see whether or not it intersected an obstacle. If the ray path is not interrupted, the field value is computed and superimposed with other terms. On the other hand, if the path is interrupted, one can still compute the field at the receiver location, and then multiply it by some factor to take into account the transmission through the obstacle. Of course, if there is not transmission, the transmission coefficient is zero and therefore the field is, also, zero.

### B. Source Field

The direct and curved surface diffracted fields are computed using the results given in Equation (191) through (198). Both fields are referred to as the source fields in this chapter. Obviously, when the field point is in the lit region, the lit region solution is used, and the shadow region solution is used if the field point is in the shadow region.

### C. Reflected Field

In order to determine the path of the reflected field from the finite dielectric slab, the law of reflection is used. To begin the solution, the receiver image position is found as illustrated in Figure 23.

The source solution is then used to compute the  $\vec{E}^S$  field at the image position. The second step is to check if the ray path from the effective source to the image position intersects the slab. If it does intersect, the reflected field  $\vec{E}^r$  is computed as follows:

$$\begin{bmatrix} E_x^r \\ E_y^r \\ E_z^r \end{bmatrix} = \begin{bmatrix} T_{xx} & T_{xy} & T_{xz} \\ T_{yx} & T_{yy} & T_{yz} \\ T_{zx} & T_{zy} & T_{zz} \end{bmatrix} \begin{bmatrix} E_x^S \\ E_y^S \\ E_z^S \end{bmatrix} \quad (199)$$

If the ray path from the source to the receiver image position does intersect the slab, then the reflected field is computed. The T-matrix in Equation (199) represents the reflected field polarization transformation matrix. It is determined from the equations [13]

$$\vec{E}^r = (\hat{n} \cdot \vec{E}^S) \hat{n} - (\hat{t} \cdot \vec{E}^S) \hat{t} \quad (200)$$

$$(\hat{t} \cdot \vec{E}^S) \hat{t} = \vec{E}^S - (\vec{E}^S \cdot \hat{n}) \hat{n} \quad (201)$$

$$\vec{E}^r = 2(\hat{n} \cdot \vec{E}^S) \hat{n} - \vec{E}^S \quad (202)$$

or

$$T_{xx} \hat{x} + T_{yx} \hat{y} + T_{zx} \hat{z} = 2(\hat{n} \cdot \hat{x}) \hat{n} - \hat{x} \quad (203)$$

$$T_{xy} \hat{x} + T_{yy} \hat{y} + T_{zy} \hat{z} = 2(\hat{n} \cdot \hat{y}) \hat{n} - \hat{y} \quad (204)$$

$$T_{xz} \hat{x} + T_{yz} \hat{y} + T_{zz} \hat{z} = 2(\hat{n} \cdot \hat{z}) \hat{n} - \hat{z} \quad (205)$$

where  $\hat{n}$  and  $\hat{t}$  are the normal and tangent unit vectors to the dielectric slab, respectively. Note that the T-matrix is independent of the receiver location, so in order to improve the efficiency of the numerical solution, it can be stored in memory.

### D. Edge-Diffracted Field

The diffracted fields from the edges of the slab are obtained using the diffraction coefficients presented in Chapters III and IV. Assuming that one has determined the ray paths for these fields, the diffracted fields are given by



$$\rho_1^d = s ; \quad (207)$$

whereas, the other radius of curvature is given by

$$\rho_2^d = \rho_c + \rho_1^d \quad (208)$$

such that for an arbitrary convex surface

$$\rho_c = \frac{2\sqrt{E} G}{\partial G / \partial t} . \quad (209)$$

Note that  $E$  and  $G$  are defined in Table III, and  $t$  as before, is the arc length along the ray path on the convex surface.

Recall that the edge diffraction coefficients are based on the diffraction from infinite straight edges, and since the plate is finite, there will be a discontinuity in the edge diffracted fields due to the corners of the slab. To compensate for this discontinuity, a diffraction coefficient associated with the corners of the slab is needed. Expressions for the corner diffracted fields associated with one corner and one edge are given in [14], but they are not considered here. It is enough to mention, that this coefficient in its present form predicts accurately the corner effect of various plate structures.

Probably the most difficult part in computing the edge diffraction field, is to determine the ray path. As depicted in Figure 25, the law of diffraction ( $\hat{s}' \cdot \hat{e} = \hat{s} \cdot \hat{e}$ ) is used to find the point of diffraction ( $x_d, y_d, z_d$ ).

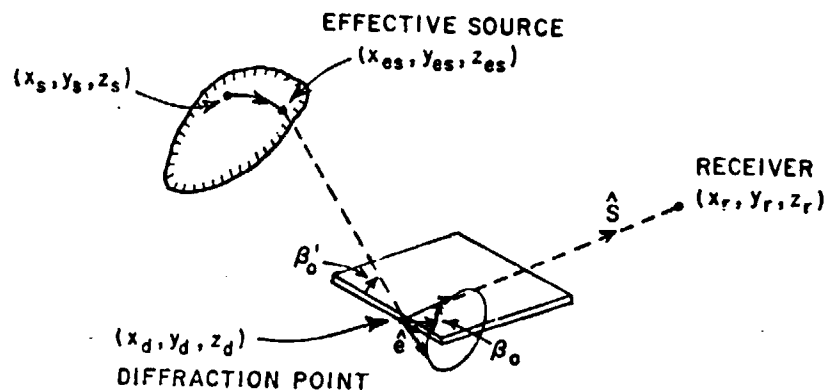


Figure 25. Geometry depicting diffraction from straight edge of finite plate.

For any particular source, plate edge, and receiver location, the diffracted ray path is unique. The key in finding this unique path is to determine the diffraction point along a given edge of the plate. Efficient algorithms to calculate the diffraction point have been developed at the ElectroScience Laboratory. These algorithms can calculate the diffraction point for any edge, including the junction edge (the edge formed by the junction of the plate and convex surface). The junction edge need not be straight, which complicates the solution. For a complete description of these algorithms refer to Reference [13] or [15].



## CHAPTER VII

### RESULTS

The final and probably most critical task is to ascertain the validity of the solutions given in the previous chapters. This is done here by comparing various calculated conical patterns with measured results.

The geometry used to test the validity of the analytical solutions is illustrated in Figure 26, where the source is mounted on a  $2\lambda \times 4\lambda$  prolate spheroid. The source is a quarter-inch monopole or a slot placed at  $\theta_s = 90^\circ$ , which means that the cylinder perturbation solution [10] is used to calculate the various geodesic paths.

It is necessary to define two coordinate systems to examine various conical pattern cuts. One of them is the cartesian coordinate system  $(\hat{x}', \hat{y}', \hat{z}')$  which defines the spheroid geometry as shown in Figure 26. This system is then rotated into what is referred to as the  $(\hat{x}, \hat{y}, \hat{z})$  system as illustrated in Figure 27. Note that the new cartesian coordinates are found by first rotating about the  $z'$ -axis the angle  $\phi_c$ , and then about the  $y$ -axis the angle  $\theta_c$ . The pattern is then taken in the  $(x, y, z)$  coordinate system with  $\theta$  fixed and varying  $\phi$  from 0 to 360.

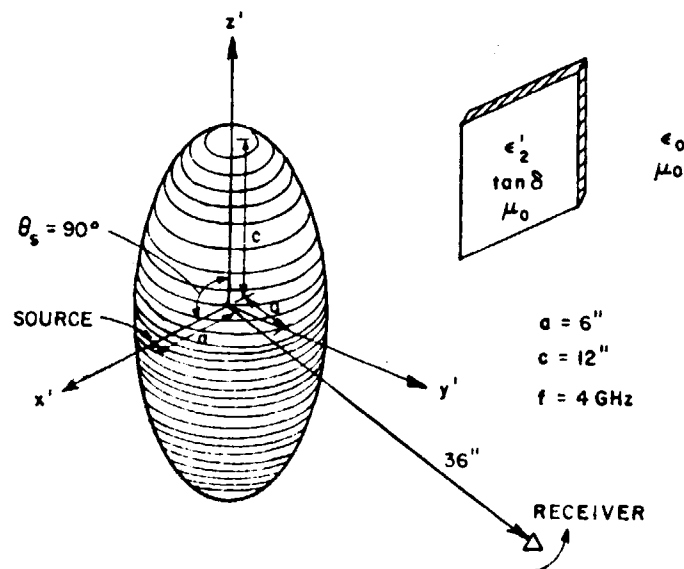


Figure 26. Geometry used to test computed results.

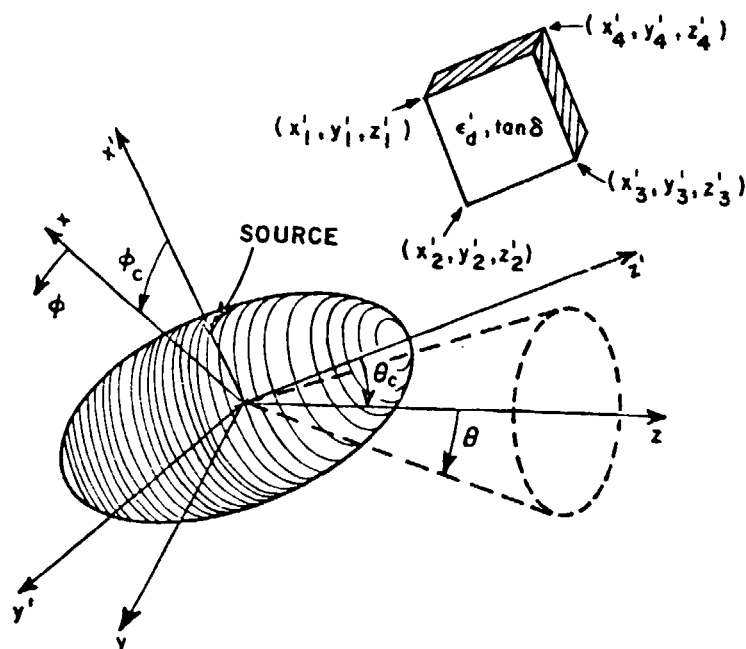


Figure 27. Definition of pattern axis.

It is appropriate at this point to describe in some detail the criteria used in deciding how many surface diffracted rays need to be used for a particular radiation direction. In the shadow region as indicated in Chapter V, the energy propagates outward from the source along the geodesic paths. This is illustrated in Figure 28 for a  $2\lambda \times 4\lambda$  prolate spheroid. As the energy flows around the surface, it is continuously diffracted along the geodesic tangent toward the field point, and thus decreasing in magnitude in relation to be maximum field strength. This implies that the region on the surface around the source point has the greatest effect on the radiated field in the shadow region. The region on the spheroid where the magnitude of the surface ray is not below a certain level of the maximum field strength is depicted in Figure 29. Thus, knowing the region of greatest energy flow, one can decide which and how many rays to use for a given radiation direction.

Calculated and measured roll-plane patterns ( $\theta = 0, \phi = 0, \theta = 90$ ) are shown in Figure 30 for a quarter-inch monopole antenna radiating without the presence of the slab. Both results agree very well except in the region from  $\phi = 144^\circ$  to  $\phi = 216^\circ$ , where the calculated results are a few decibels below the measured results. This is due to the fact that only rays 1 and 2 shown in Figure 31 are used. Because of the dimensions of the spheroid, i.e.,  $c = 4\lambda$  is only twice as long as  $a = 2\lambda$ , the contributions of rays 3 and 4 are important and if included, the

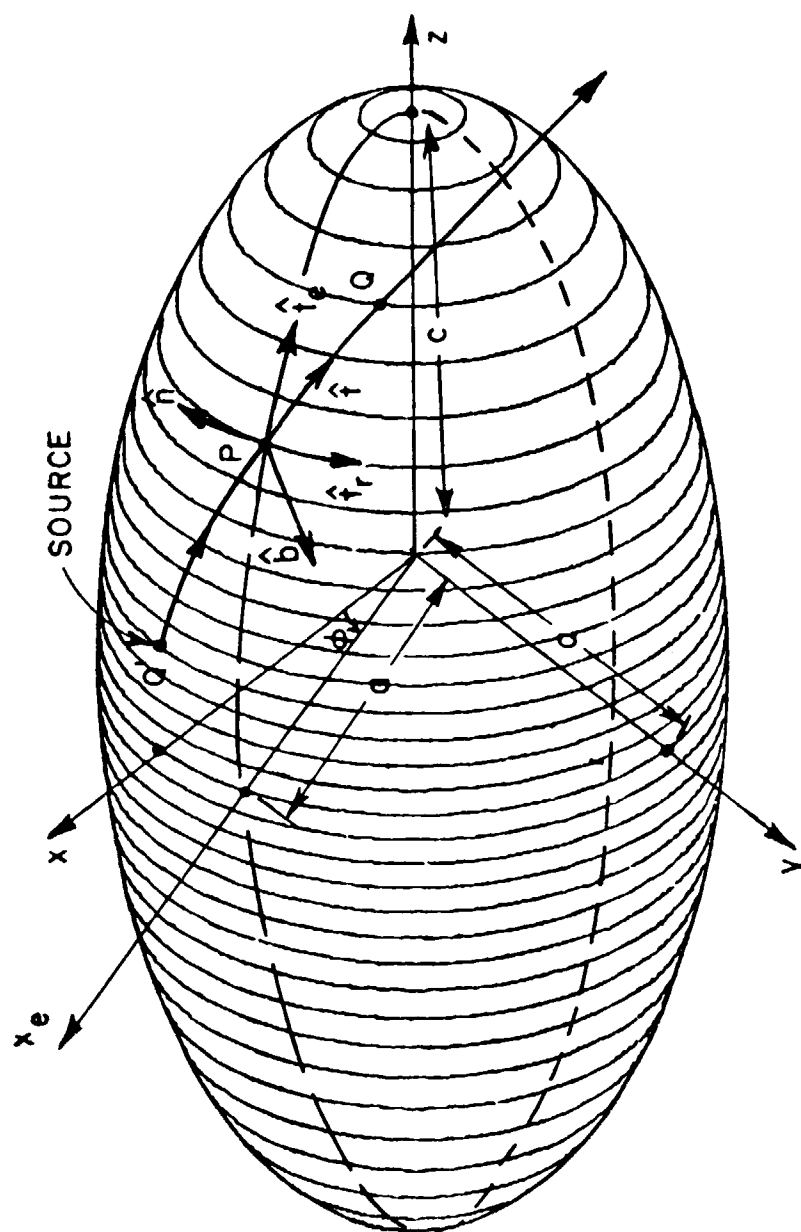


Figure 28. Geodesic path on a spheroid.

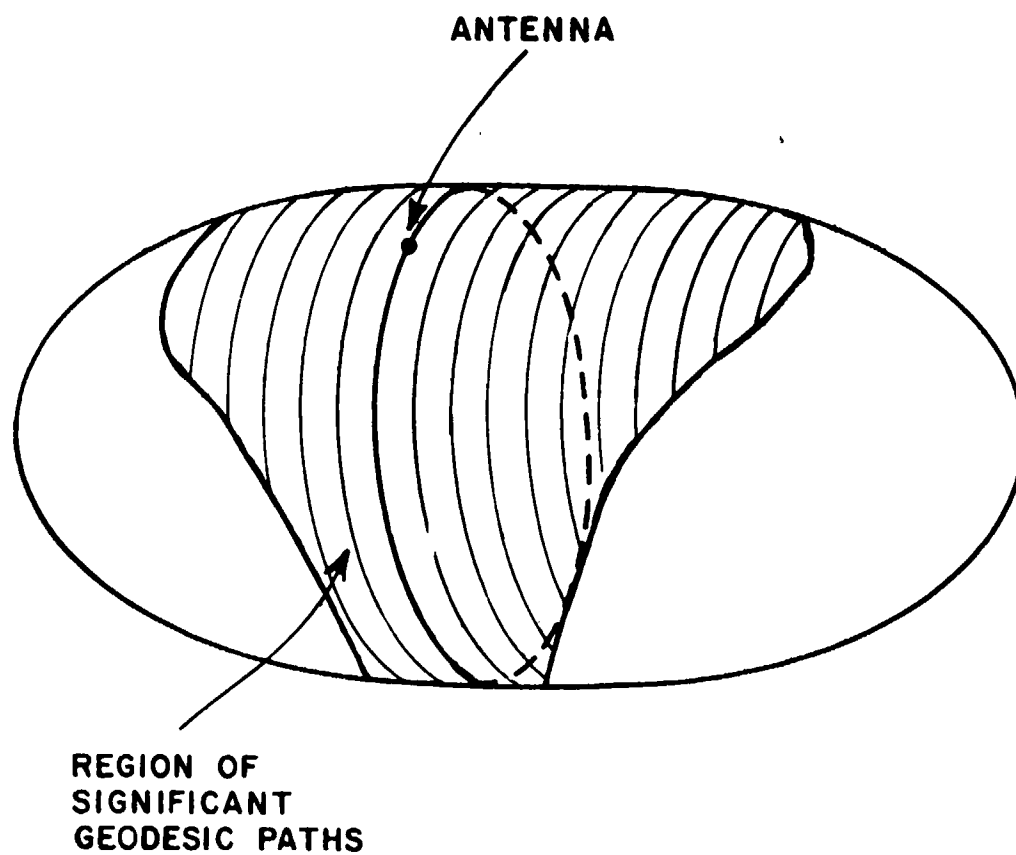


Figure 29. Region where the magnitude of the surface rays is significant in relation to the pattern maximum, i.e., 40 dB below.

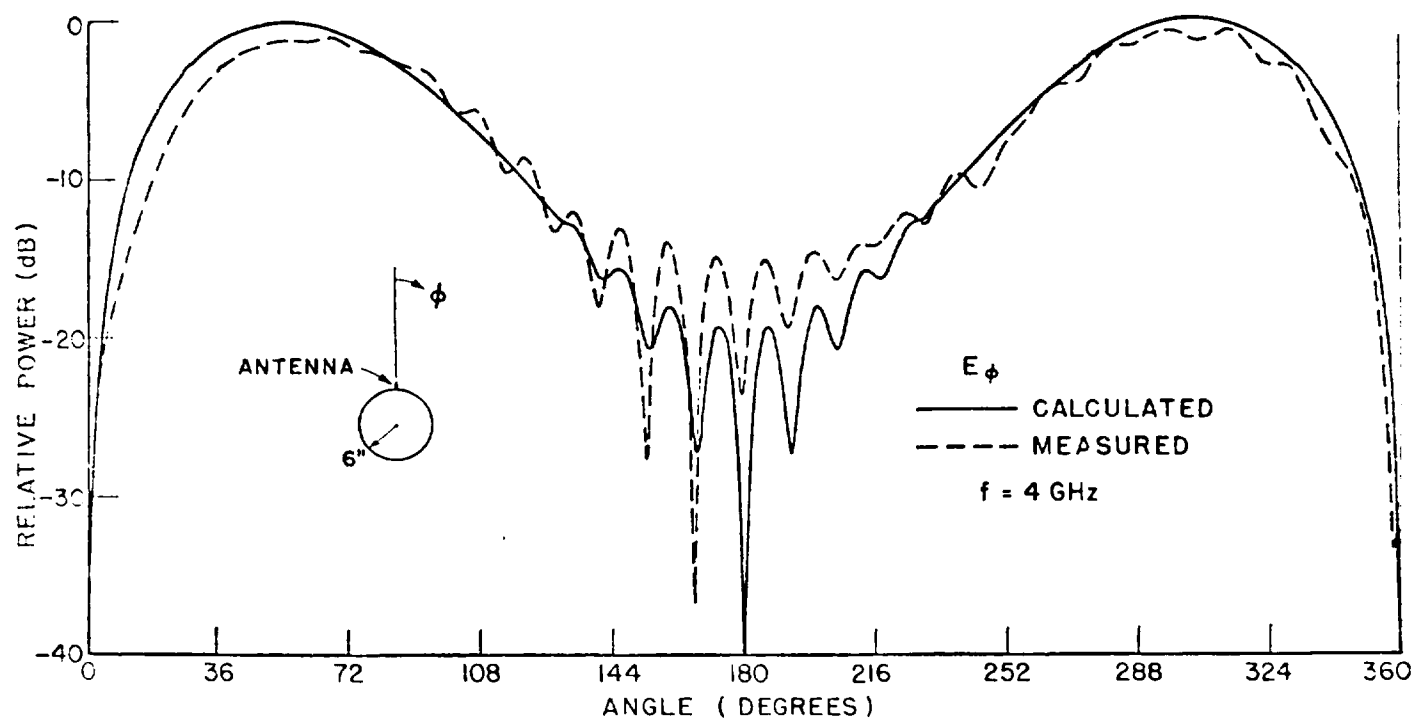


Figure 30. Roll plane ( $\theta=0$ ,  $\phi=0$ ,  $\theta=90$ ) patterns for a 0.25" monopole mounted at  $\theta_s=90$ . Only rays 1 and 2 are included (see Figure 31).

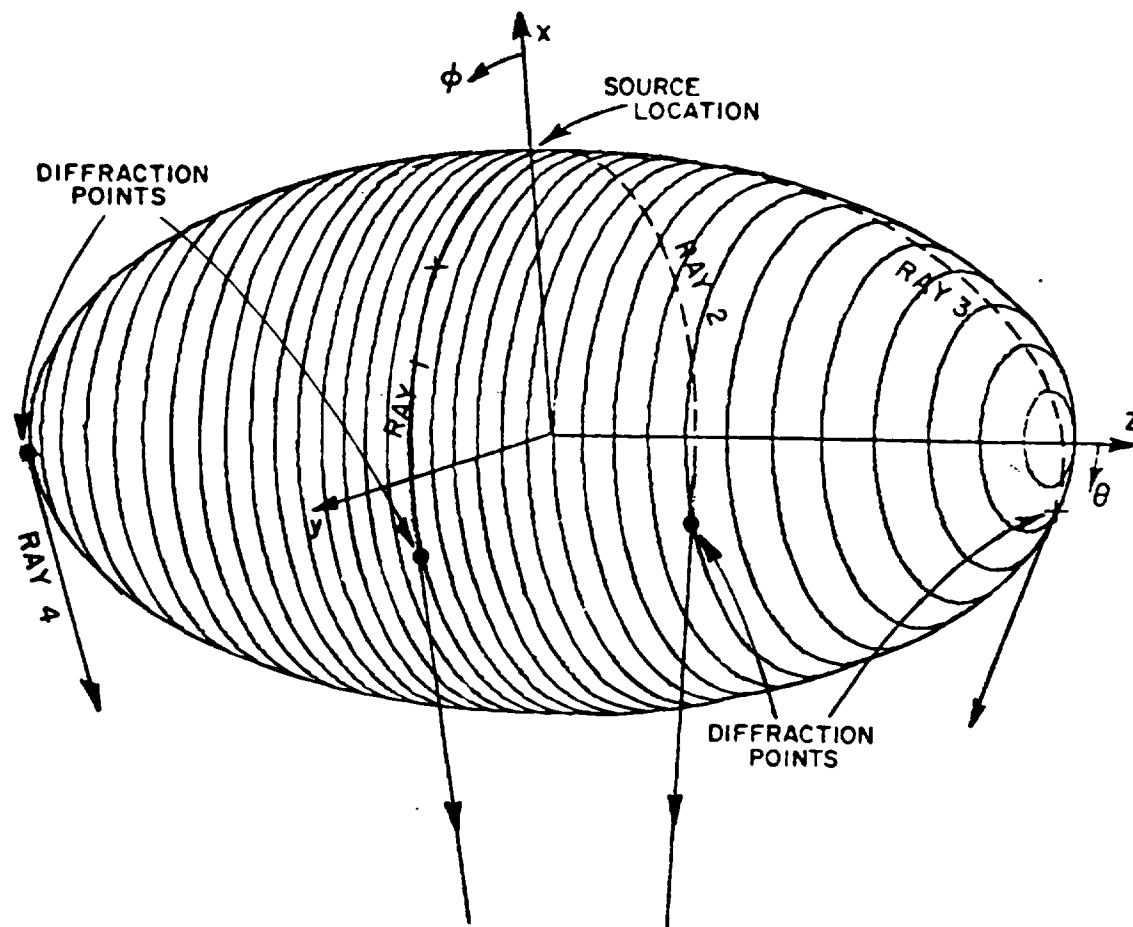


Figure 31. The four dominant GTD terms that radiate at  $(\theta=90^\circ, \phi=190^\circ)$ .

calculated pattern would resemble more closely the measured pattern in that region.

In most practical applications, the ratio of the major and minor axis is much greater than two, which implies that rays 3 and 4 are not significant in the roll plane cut. In all the calculated roll-plane patterns ( $\theta_c=0., \phi_c=0., \theta=90.$ ) that are shown here, only rays 1 and 2 are included.

The results shown in this thesis are divided into two sets according to the position of the dielectric and/or metal plate(s). The first set includes calculated and measured conical patterns for the geometry depicted in Figure 32.

Figures 33-39 show roll plane patterns for a quarter-inch monopole located at  $\theta_s=90$  (see Figure 26) radiating in the presence of metal or dielectric plates of different thickness and dielectric constants. There is very good agreement between the calculated and measured patterns even though in making the measurements, it was very difficult to position the plate at the exact desired location due to the lack of a reference coordinate system. Note that from now on, if it is not specified, it is assumed that the source is a quarter-inch monopole located at  $\theta_s=90^\circ$ .

It was indicated that the GTD solution is equal to the sum of several terms. Figures 40-41 show the individual terms of the solution for a roll-plane cut ( $\theta_c=0=\phi_c, \theta=90$ ), i.e., source, reflected and diffracted fields, for a 10" x 10" dielectric slab of  $\epsilon_r=10.0$  and  $d=0.25$ ". Figure 42 shows the total field for the dielectric slab and for a metal backed dielectric.

Figure 44 shows the effect of the dielectric constant on the total field for four different dielectric constants. All the patterns are roll-plane cuts. Figure 45 shows the same results except the dielectric slab is metal backed.

Even though corner diffraction was not discussed in detail, Figure 46 shows, the effect of adding the corner diffracted term to the total solution and it is clear that the discontinuity around  $\phi=70$  is removed when the corner diffracted term is added. The conical patterns are for  $\theta_c=0., \phi_c=0., \theta=75.1^\circ$ .

More calculated examples are shown in Figures 47-48 for conical patterns other than roll-plane cuts where both polarizations ( $E_\theta, E_\phi$ ) are significant. Another common source besides the monopole is a slot antenna. Figure 49 shows patterns for axial and circumferential 0.4" x 0.8" slots located at  $\theta_s=90^\circ$ . It is assumed a cosine distribution exists along the longer side and an uniform distribution along the shorter side of the slot.

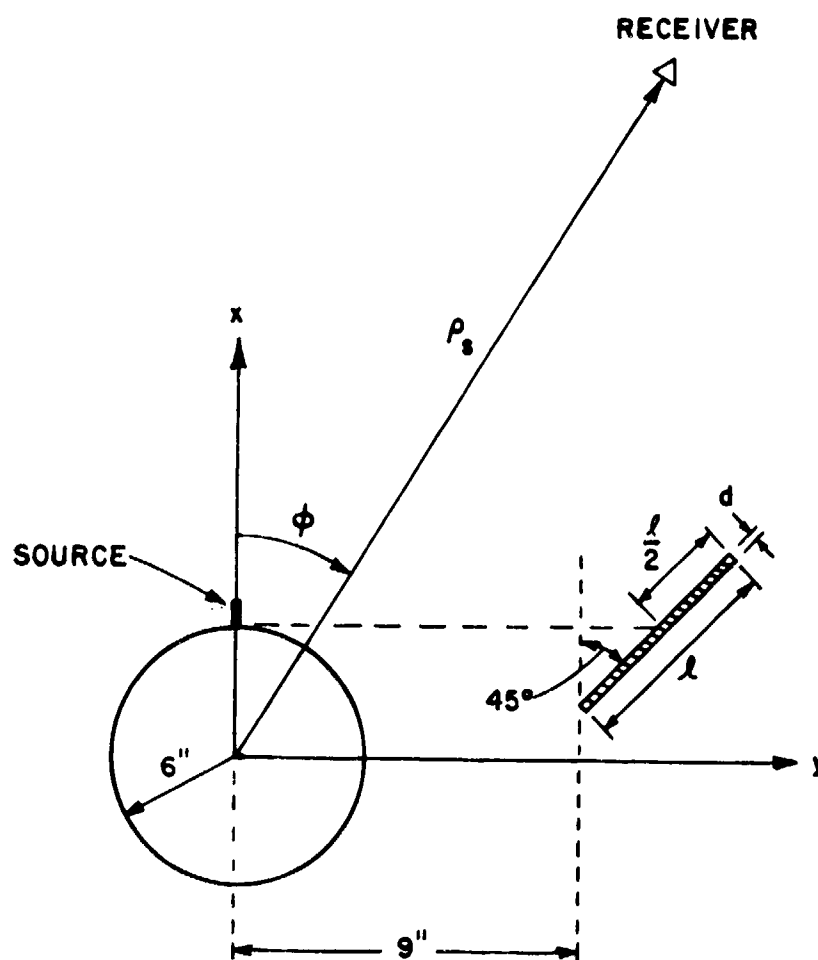


Figure 32. End view of the geometry used to calculate and measure the conical patterns depicted in Figures 33-49.



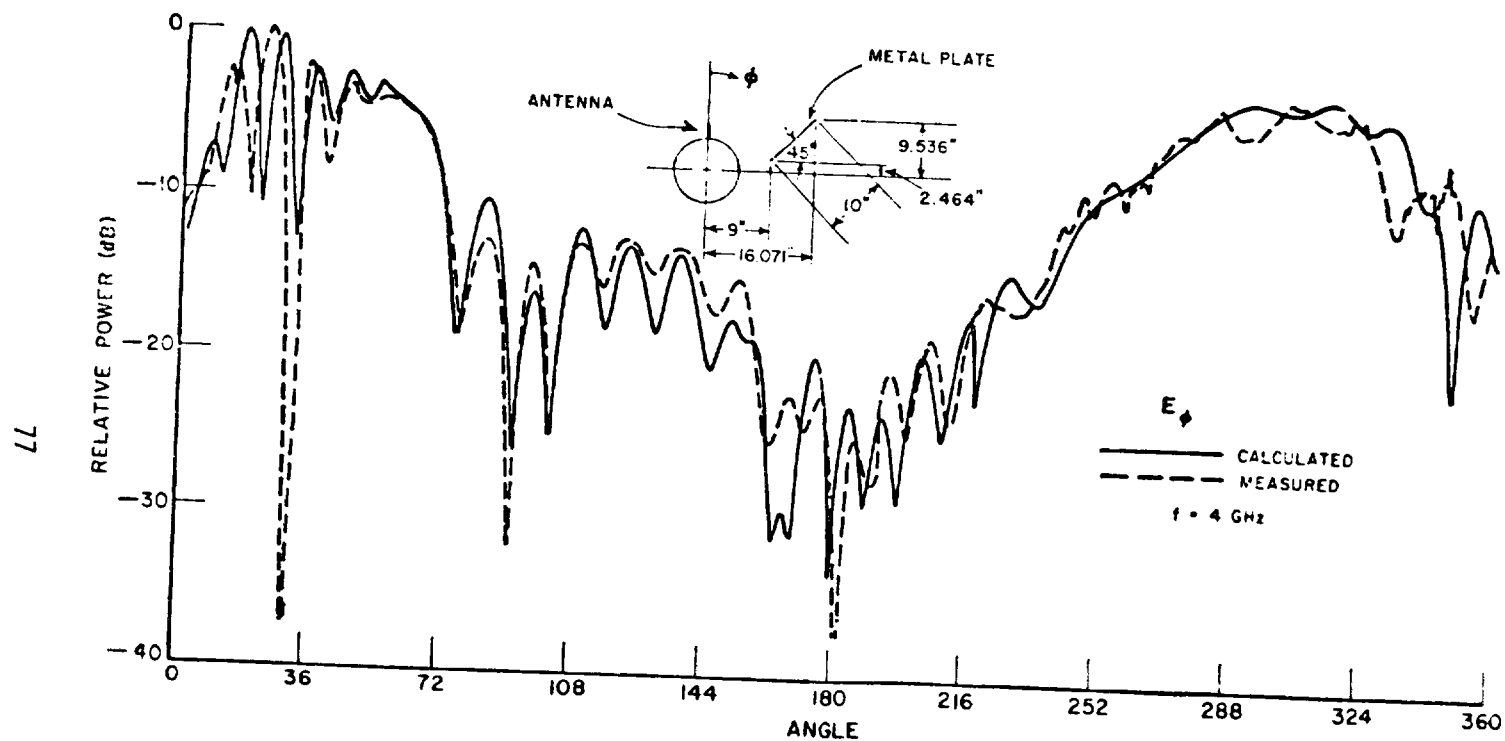


Figure 33. Roll plane ( $\theta_c = 0^\circ, \phi_c = 0^\circ, \theta = 90^\circ$ ) patterns for a 0.25" monopole mounted at  $\theta_s = 45^\circ$  on a  $2\lambda \times 4\lambda$  spheroid.

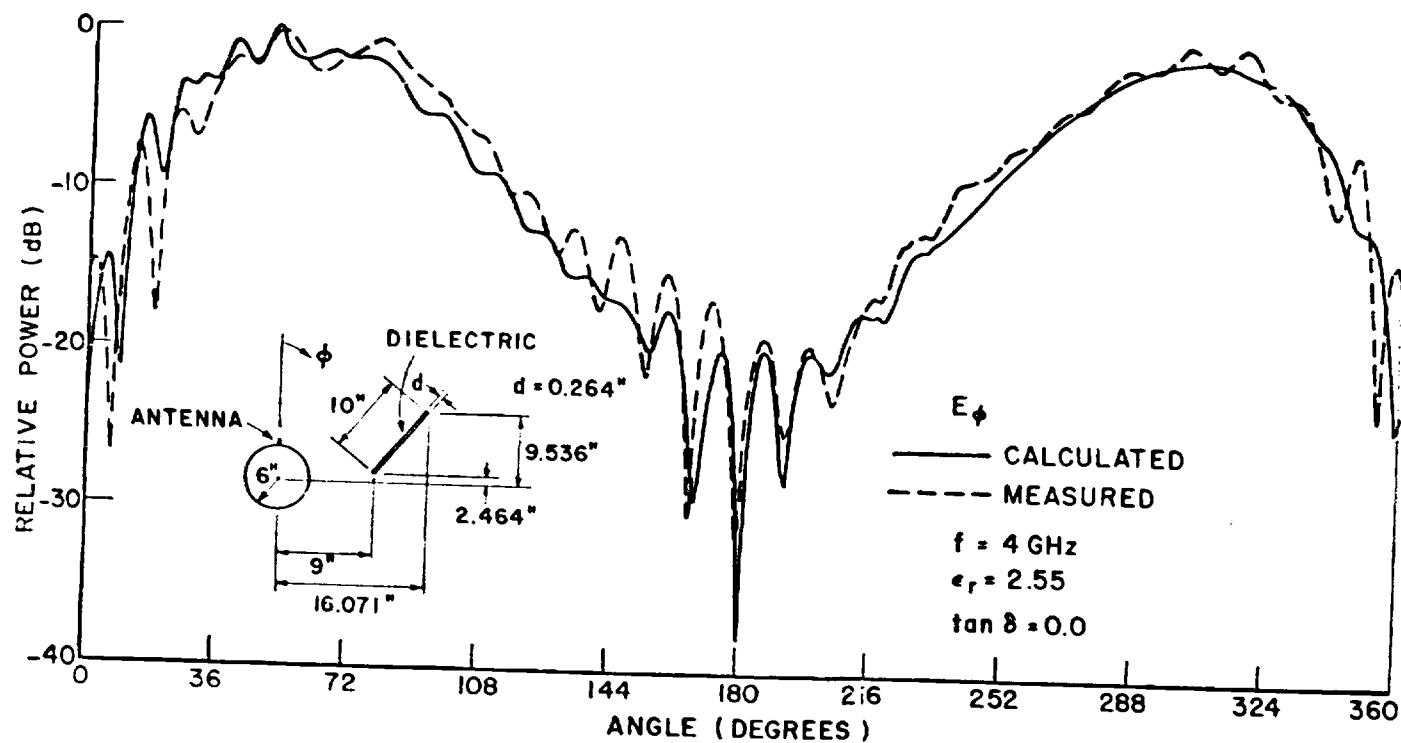


Figure 34. Roll plane ( $\theta = 0^\circ, \phi = 0^\circ, \theta = 90^\circ$ ) patterns for a 0.25" monopole mounted at  $\theta_s = 90^\circ$  on a  $2\lambda \times 4\lambda$  spheroid.

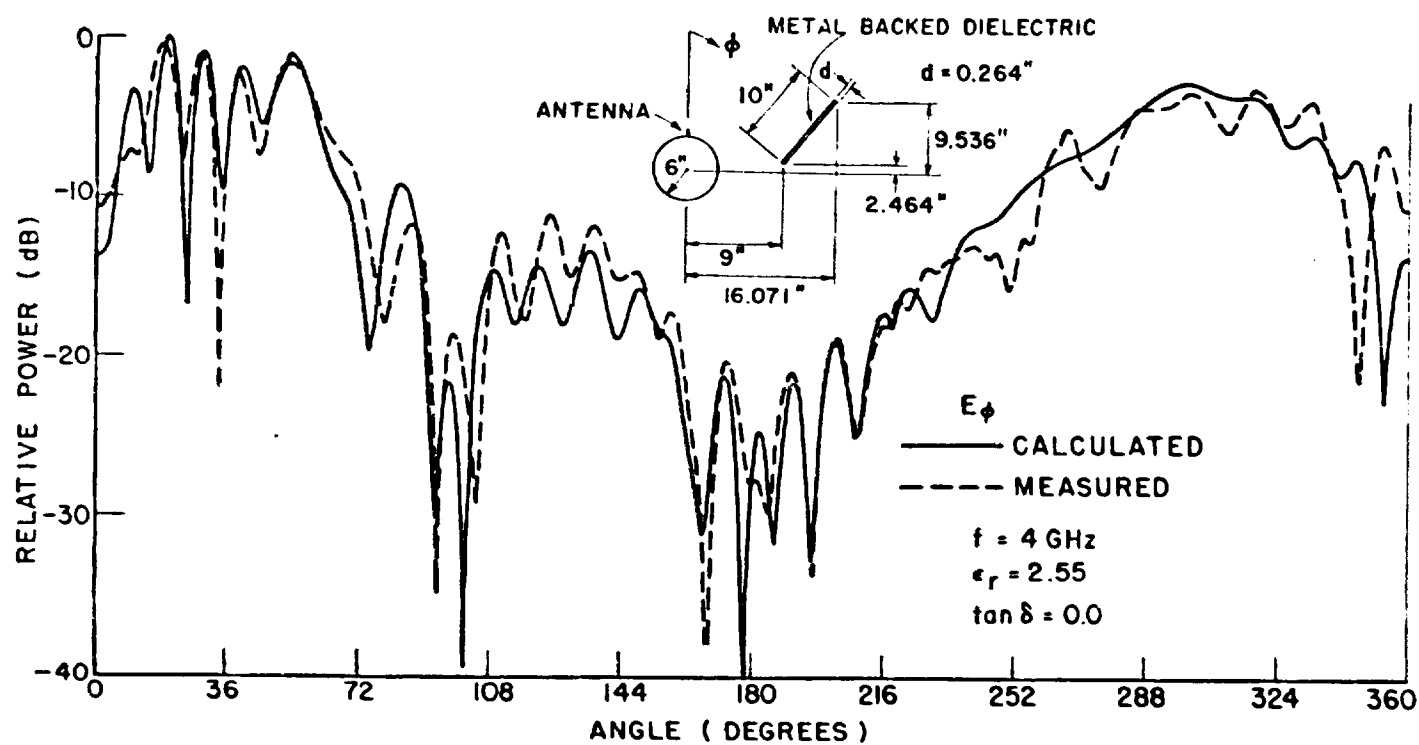


Figure 35. Roll plane ( $\theta = 0^\circ, \phi = 0^\circ, \psi = 90^\circ$ ) patterns for a 0.25" monopole mounted at  $\theta_s = 90^\circ$  on a  $2\lambda \times 4\lambda$  spheroid.

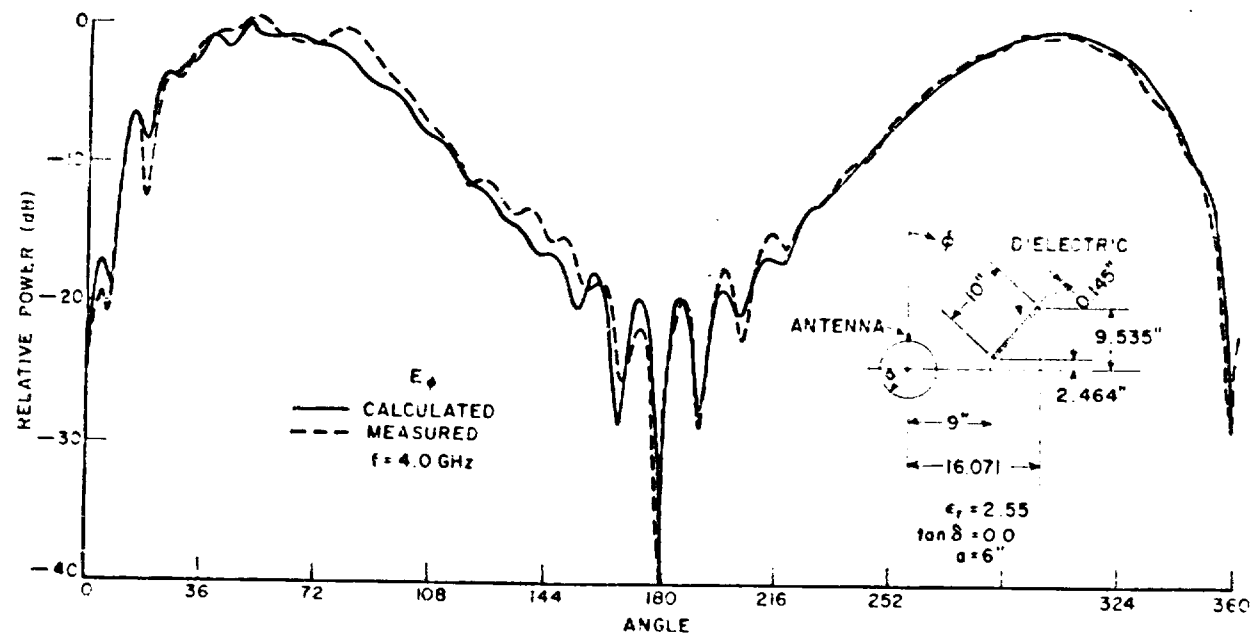


Figure 36. Roll plane ( $\theta = 0^\circ, \phi = 0^\circ, \theta = 90^\circ$ ) patterns for a 0.25" monopole mounted at  $\theta_s = 90^\circ$  on a  $2\lambda \times 4\lambda$  spheroid.

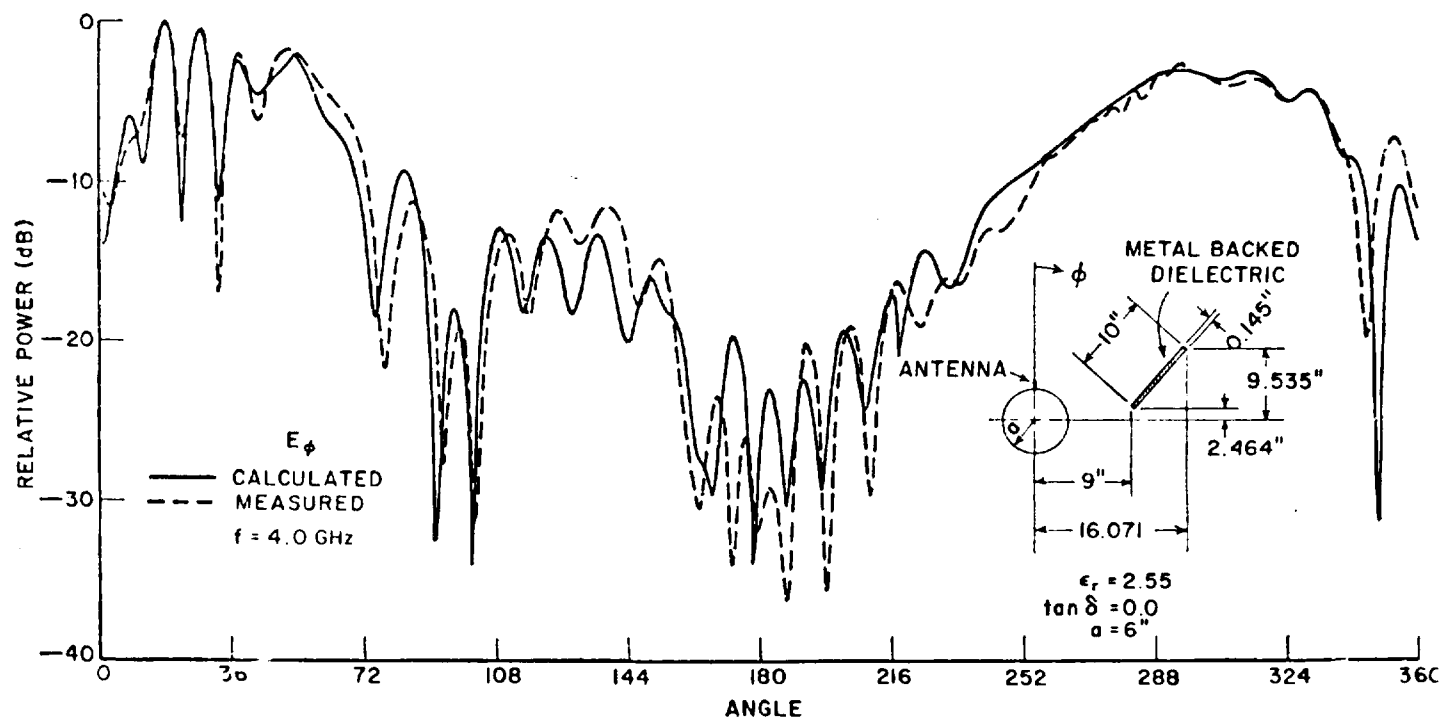


Figure 37. Roll plane ( $\theta = 0^\circ, \phi = 0^\circ, \theta = 90^\circ$ ) patterns for a 0.25" monopole mounted at  $\theta_c = 90^\circ$  on a  $2\lambda \times 4\lambda$  sphere of d.

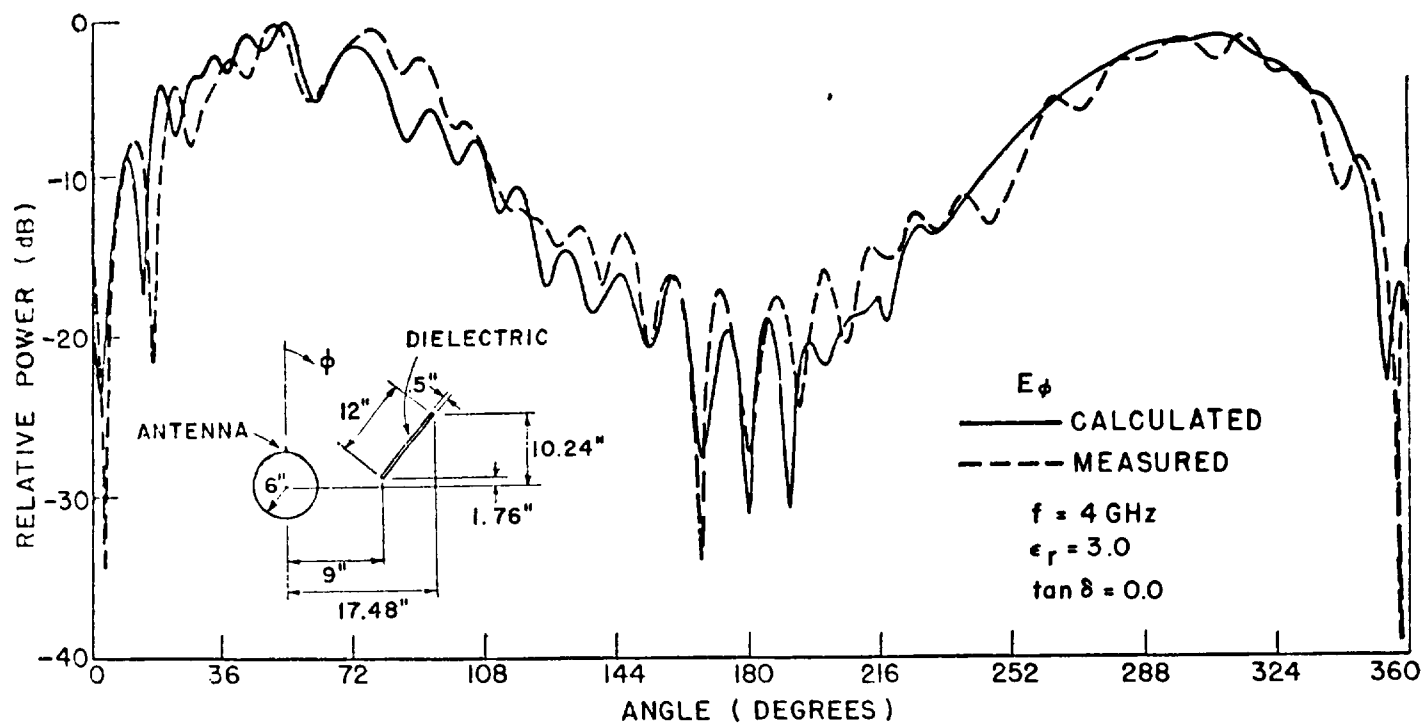


Figure 38. Roll plane ( $\theta = 0^\circ, \phi = 0^\circ, \theta = 90^\circ$ ) patterns for a 0.25" monopole mounted at  $\theta_s = 90^\circ$  on a  $2\lambda \times 4\lambda$  spheroid.

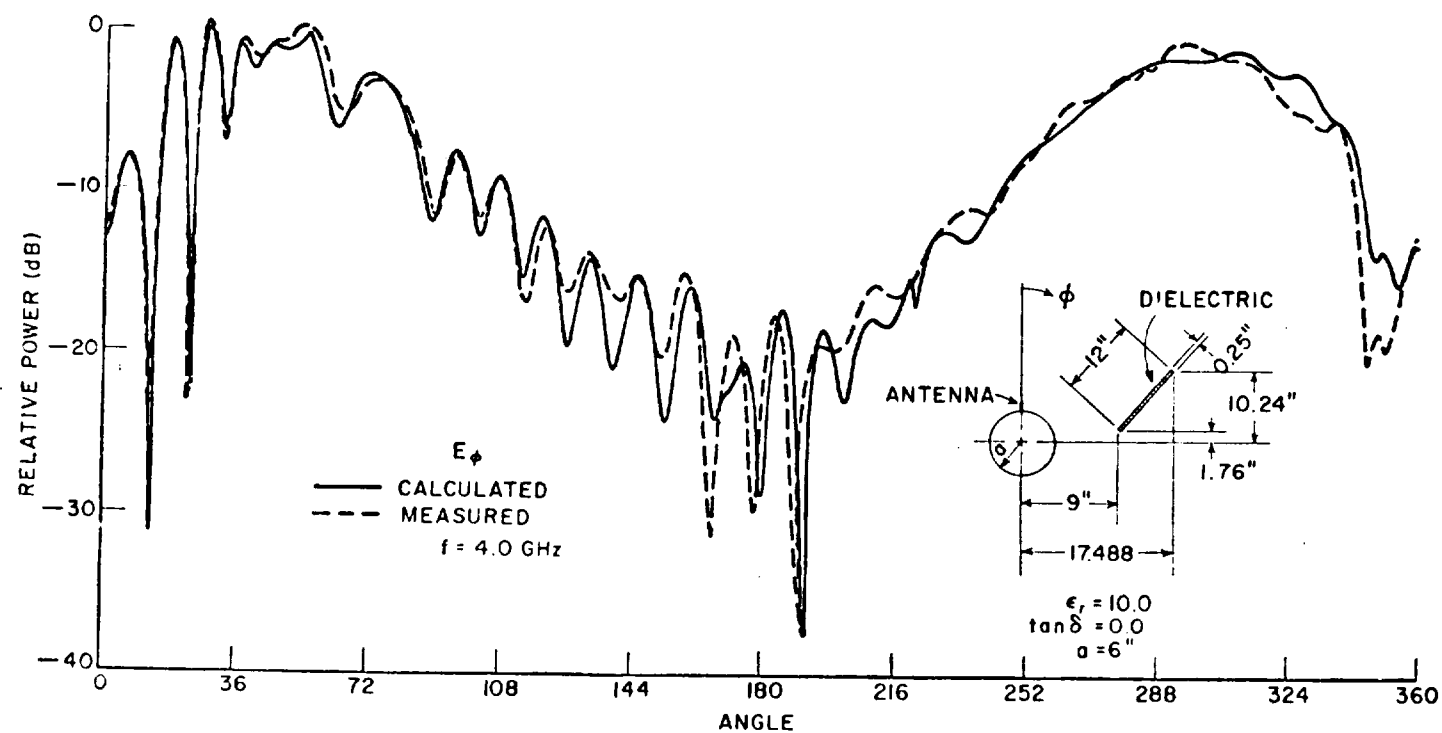


Figure 39. Roll plane ( $\theta = 0^\circ, \phi = 0^\circ, \theta = 90^\circ$ ) patterns for a 0.25" monopole mounted at  $\theta_s = 90^\circ$  on a  $2\lambda \times 4\lambda$  spheroid.

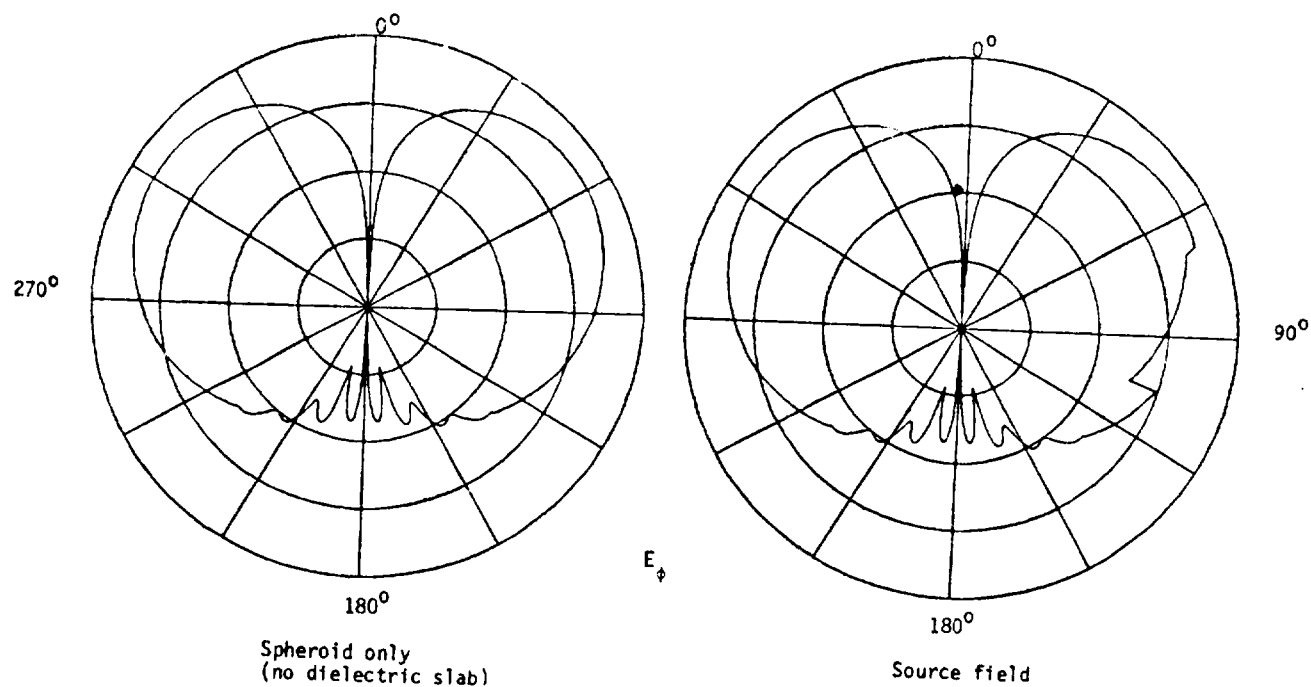


Figure 40. Calculated radiation patterns ( $\theta_c = 0^\circ$ ,  $\phi_c = 0^\circ$ ,  $e = 90^\circ$ ) for a 0.25" monopole mounted at  $\theta_s = 90^\circ$ . The dielectric slab is a 10" x 10" square,  $\epsilon_r = 10.$ ,  $d = 0.264$ ",  $\tan \delta = 0.0$  (See Figure 32),  $\rho_s = 36$ ".



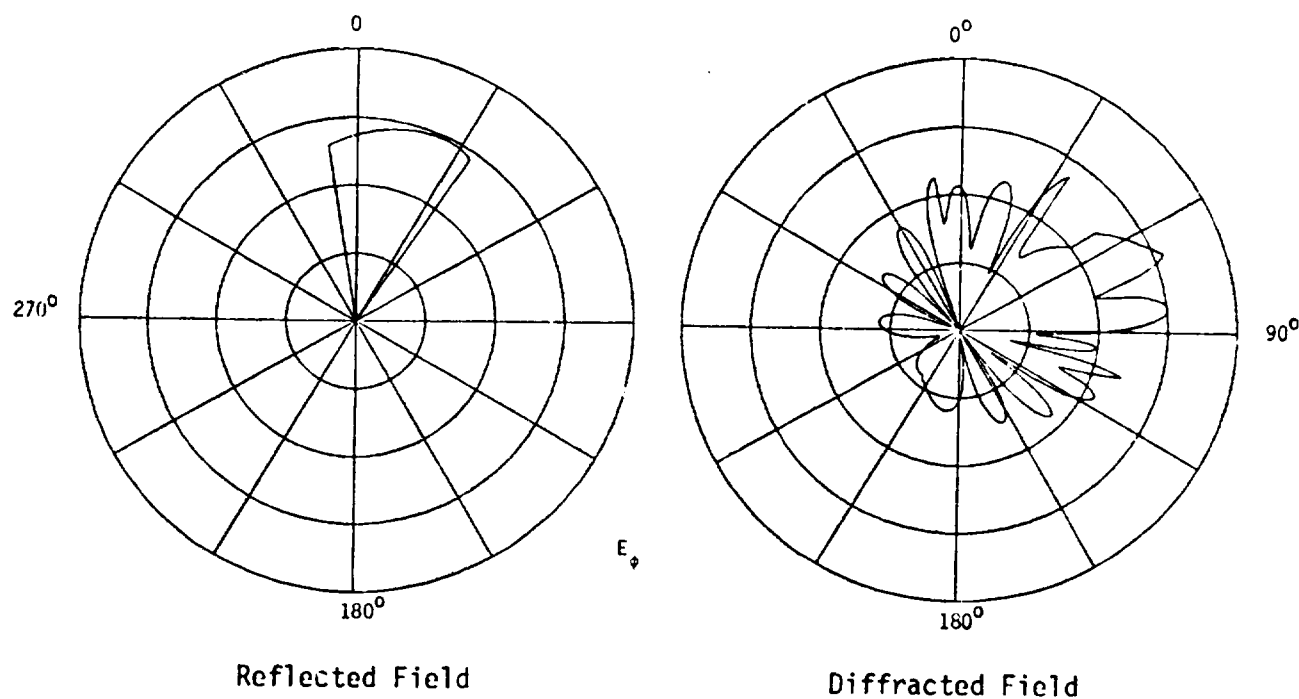
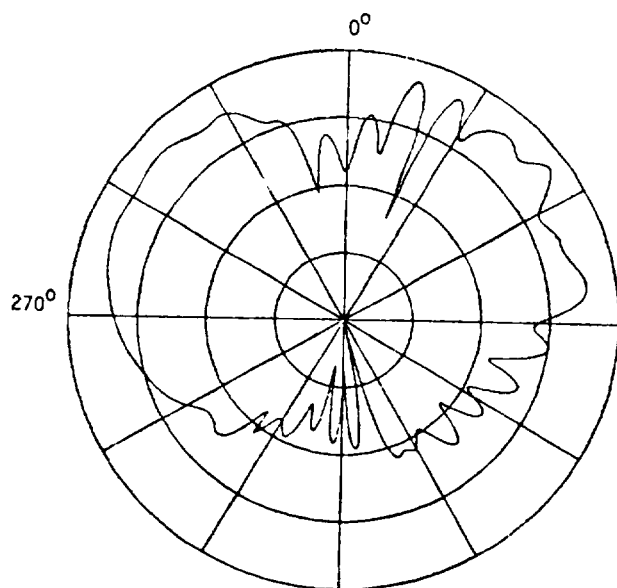
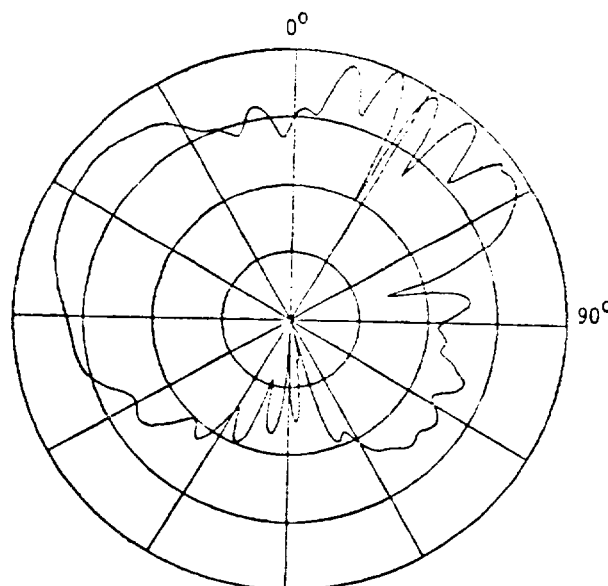


Figure 41. Calculated radiation patterns ( $\theta_c = 0^\circ$ ,  $\phi_c = 0^\circ$ ,  $\theta = 90^\circ$ ) for a 0.25" monopole mounted at  $\theta_s = 90^\circ$ . The dielectric slab is a 10" x 10" square,  $\epsilon_r = 10.$ ,  $d = 0.264$ "  $\tan \delta = 0.0$  (See Figure 32),  $\rho_s = 36$ ".



Total field for dielectric plate only

 $E_\phi$ 

Total field for a metal-backed dielectric plate

Figure 42. Calculated radiation patterns ( $\theta = 0^\circ$ ,  $\phi = 0^\circ$ ,  $\theta = 90^\circ$ ) for a 0.25" monopole mounted at  $\theta_s = 90^\circ$ . The dielectric slab is a 10" x 10" square,  $\epsilon_r = 10$ ,  $d = 0.264$ ",  $\tan \delta = 0.0$ , (See Figure 32),  $\rho_s = 36$ ".

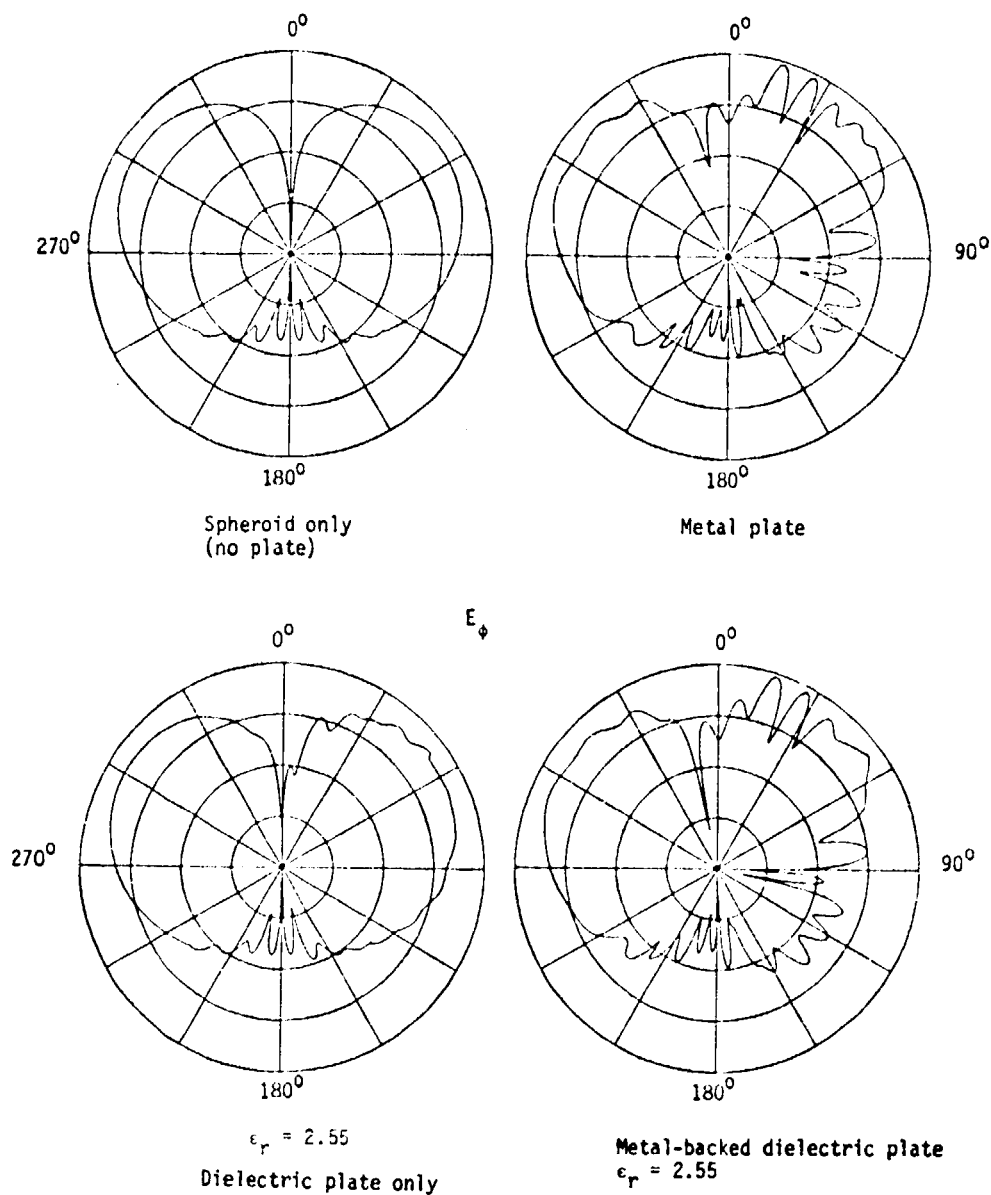


Figure 43. Calculated roll-plane ( $\theta_c = 0^\circ$ ,  $\phi_c = 0^\circ$ ,  $\theta = 90^\circ$ ) patterns for a 0.25" monopole mounted at  $\theta_c = 90^\circ$ . The dielectric slab is a 10" x 10" square, of thickness  $d = 0.145$ ",  $\tan \delta = 0.0$  (See Figure 32),  $\rho_s = 36$ ".

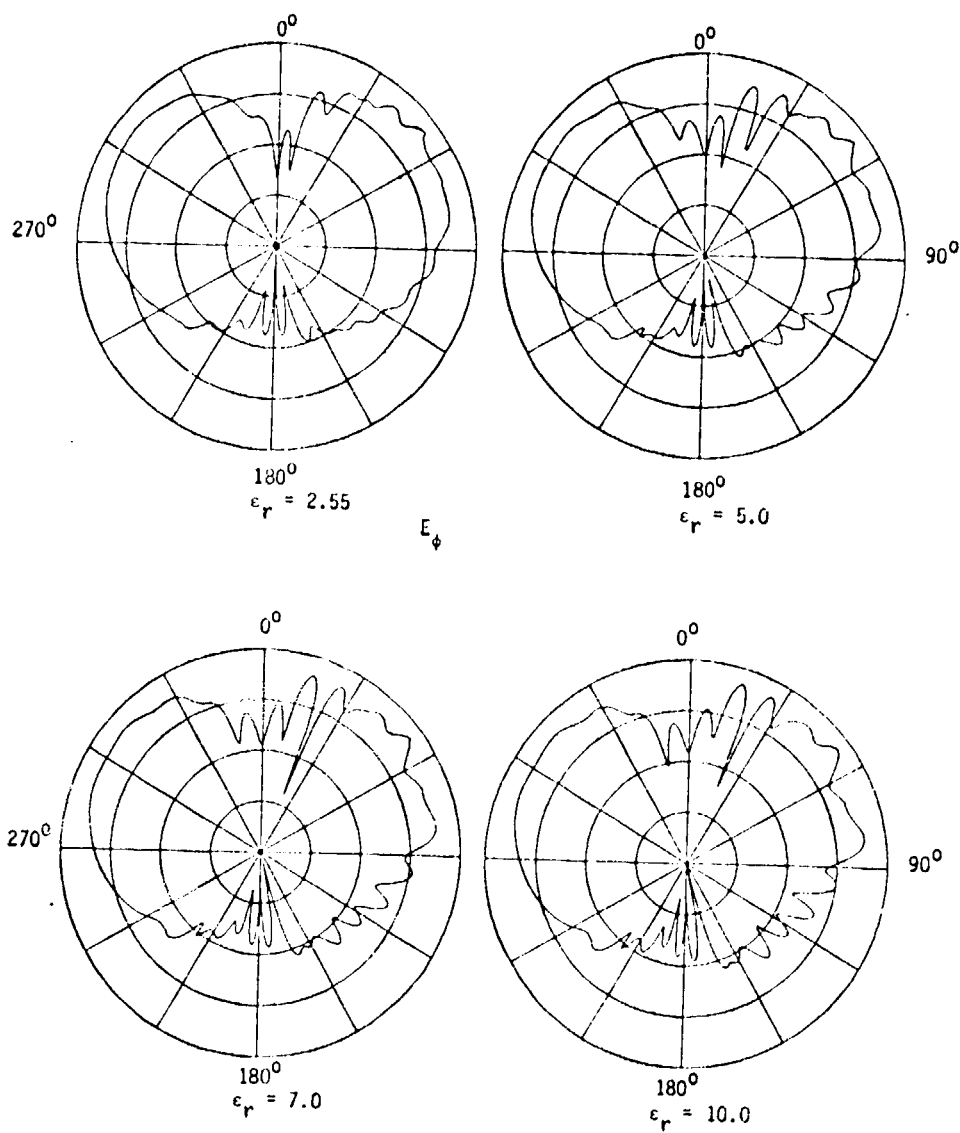


Figure 44. Calculated roll-plane ( $\theta_c = 0^\circ$ ,  $\phi_c = 0^\circ$ ,  $\theta = 90^\circ$ ) patterns for a 0.25" monopole located at  $\theta_c = 90^\circ$ . The dielectric plate is a 10" x 10" square of thickness  $d = 0.264$ ",  $\tan \delta = 0.0$ , (See Figure 32),  $\rho_s = 36$ ".

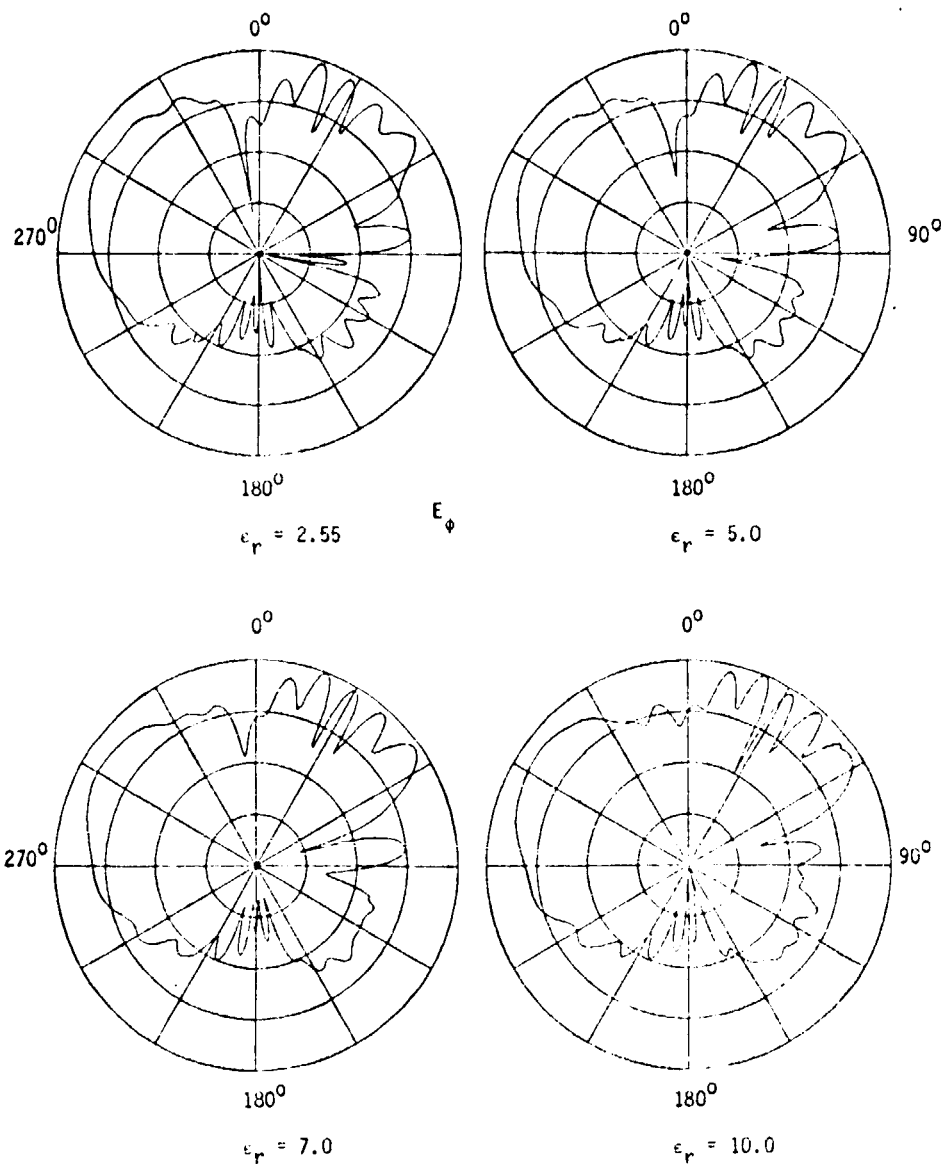


Figure 45. Calculated roll-plane ( $\theta_c = 0^\circ$ ,  $\phi_c = 0^\circ$ ,  $u = 90^\circ$ ) patterns for a 0.25" monopole mounted at  $\theta_c = 90^\circ$ . The plate is a 10" x 10" metal-backed dielectric<sup>s</sup> plate of thickness  $d = 0.264$ ",  $\tan \delta = 0.0$  (See Figure 32),  $\rho_s = 36$ ".

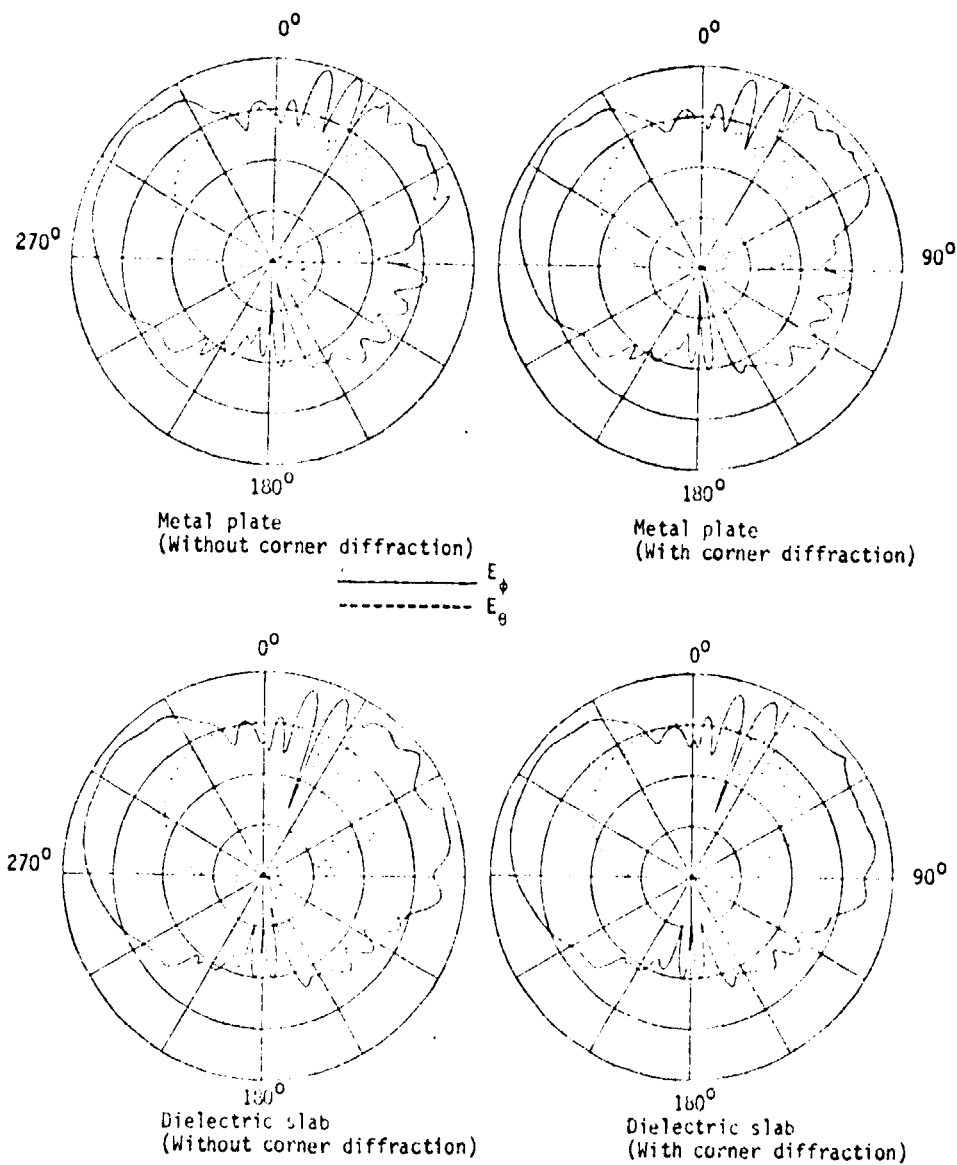


Figure 46. Calculated patterns ( $\theta_c = 0^\circ$ ,  $\phi_c = 0^\circ$ ,  $\theta = 75.10^\circ$ ) for a 0.25" monopole located at  $\theta = 90^\circ$ . The plate (metal or dielectric) is a 10" x 10" square. The dielectric plate has a thickness of  $d = 0.264$ ",  $\epsilon_r = 10.$ ,  $\tan \delta = 0.$  (See Figure 32)  $\rho_s = 36$ ".

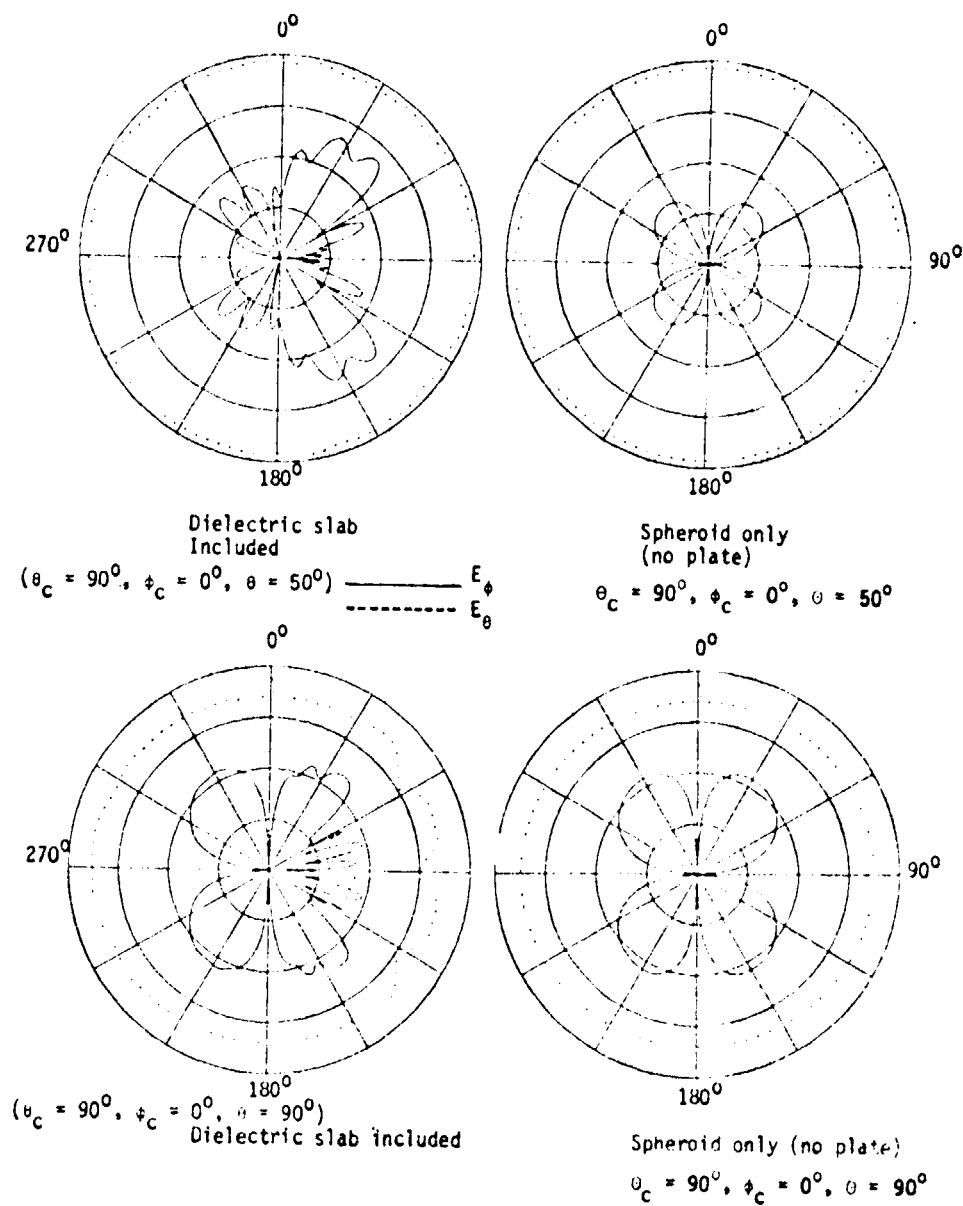


Figure 47. Calculated conical patterns for a 0.25" monopole located at  $\theta_c = 90^\circ$ . The dielectric plate is a 12" x 12" square of thickness  $d = 0.25$ ",  $\epsilon_r = 10.$ ,  $\tan \delta = 0.0$  (See Figure 32)

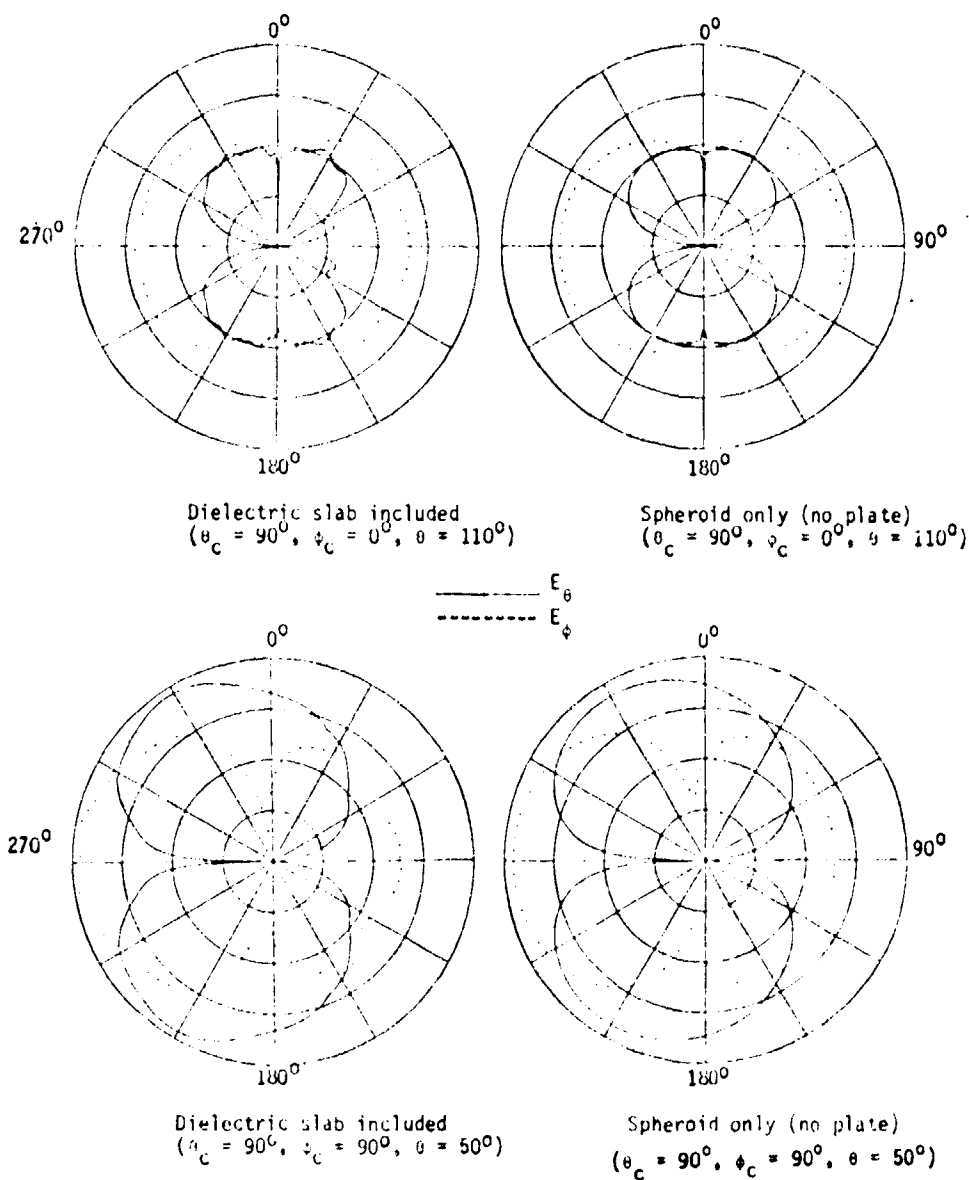


Figure 48. Calculated conical patterns for a 0.25" monopole mounted at  $\theta_c = 90^\circ$ . The dielectric plate is a 12" x 12" square at thickness  $d = 0.25$ ",  $\epsilon_r = 10.$ ,  $\tan \delta = 0.0$  (See Figure 32)



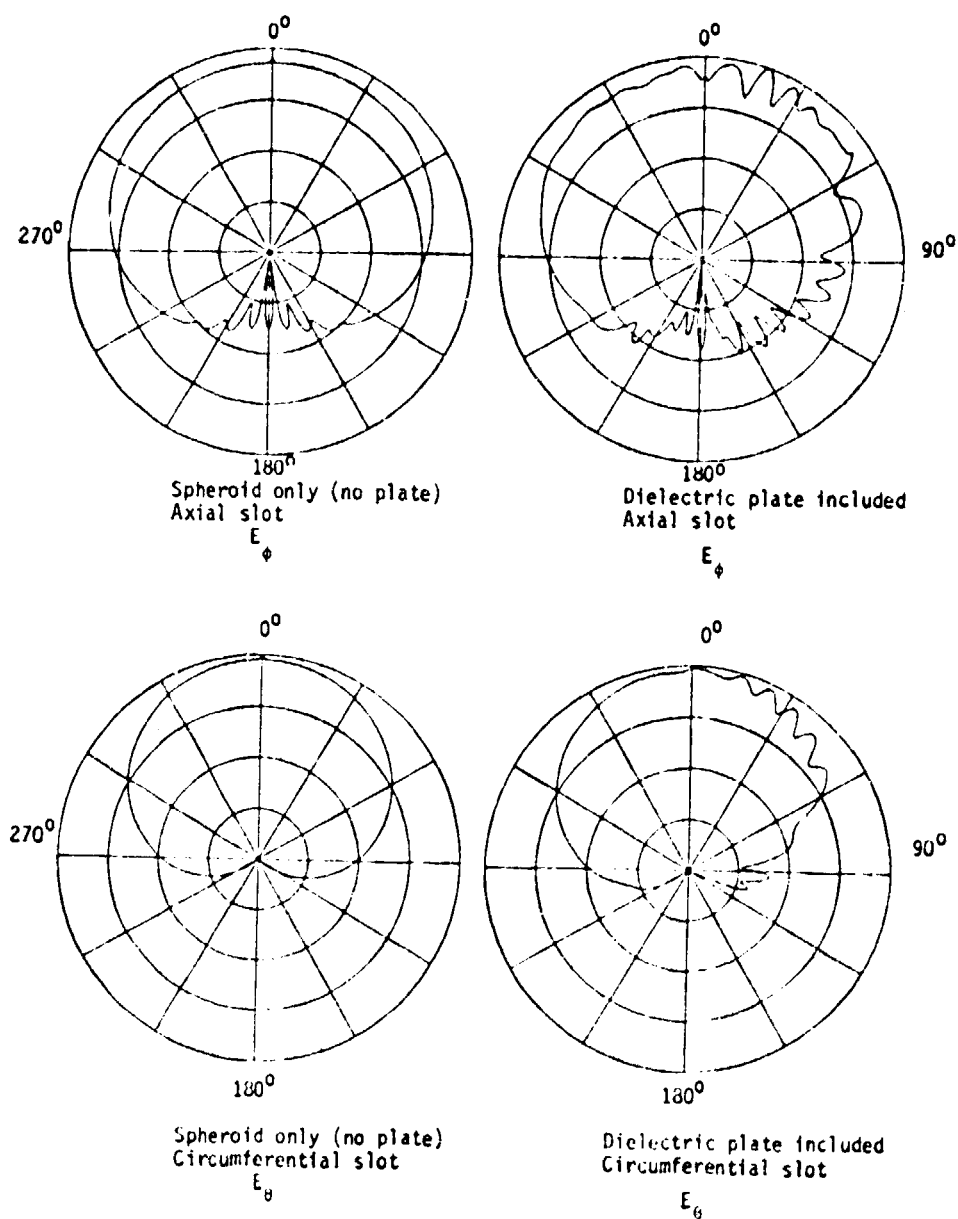


Figure 49. Calculated roll-plane ( $\theta_c = 0^\circ$ ,  $\phi_c = 0^\circ$ ,  $\theta = 90^\circ$ ) patterns for a  $0.4'' \times 0.8''$  slot located at  $\theta_s = 90^\circ$ . The dielectric plate is a  $12'' \times 12''$  square of thickness  $d = 0.25''$ ,  $\epsilon_r = 10.$ ,  $\tan \delta = 0.0$  (See Figure 32)  $\rho_s = 36''$ .

In the geometry for the first set of results (see Figure 32), the plate is located in both the lit and shadow regions. That is, the incident field along the slab is composed of the direct source field and the surface diffracted field. The second set of conical patterns is for the geometry depicted in Figure 50. In this case the slab is located entirely in the shadow region, so the fields illuminating the plate are surface diffracted rays only. Figures 51-56 show calculated and measured roll-plane patterns for a quarter-inch monopole located at  $\theta_s = 90^\circ$ . Again, the results are seen to agree very well. Note that there is a discontinuity in the calculated patterns for the dielectric slab case around  $\phi = 90^\circ$ , which implies that some extra term should be added to the total field. In this case that term is the double-diffracted field which was not included in the total field. This illustrates a very important property of GTD, which is the fact that if any term that is significant in the total solution is not included, it shows up in the calculated pattern in the form of a jump or kink. Thus, one has a self-correcting mechanism by which one can gauge the impact of the missing term and add higher order terms to the solution until one obtains a continuous pattern.

The individual terms that make up the total field for the geometry of Figure 50 are shown in Figures 57-58 for a 12" x 12" dielectric slab of thickness  $d=0.25"$  and  $\epsilon_r=10$ . Figure 58 also shows the total field for the dielectric slab and for a metal-backed dielectric.

Finally, Figures 59-61 show the effect of the dielectric constant on the total field for three different dielectric constants.

It is important to emphasize that all the results presented here were obtained for a very stringent case due to the dimensions of the spheroid which is approaching a sphere. To actually model a missile or aircraft fuselage, the electric dimensions of the spheroid would be much larger than the ones chosen here, i.e.,  $2\lambda \times 4\lambda$ . Since GTD is based on the assumptions of the locality of the diffraction phenomenon, the larger the electric dimensions of the spheroid, one would expect to obtain more accurate calculated patterns.

C-2

95

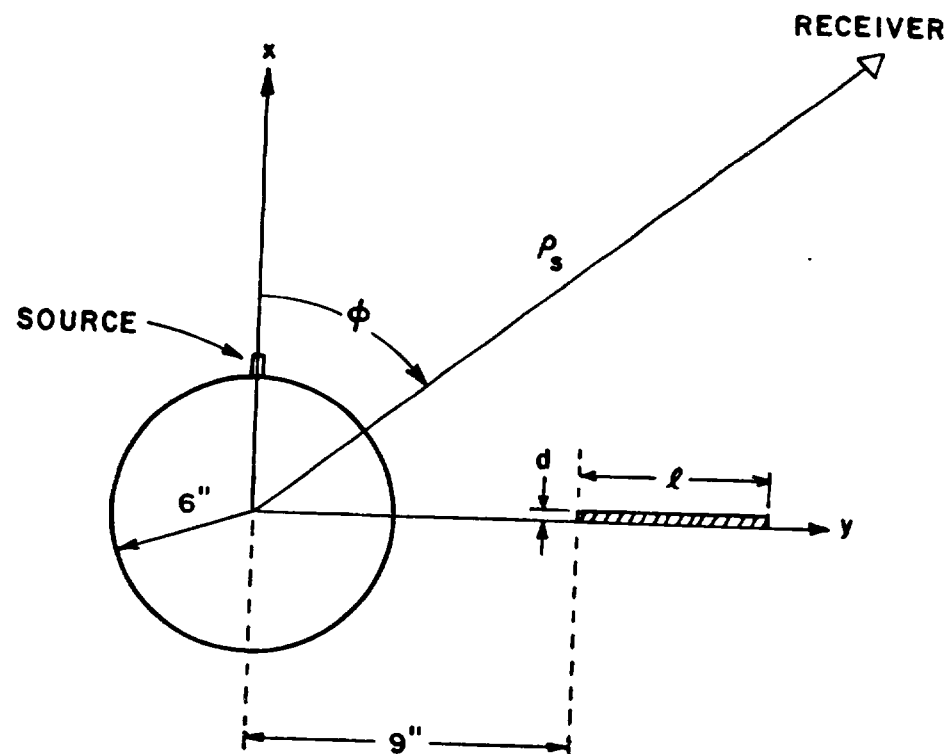


Figure 50. End view of the geometry used to calculate and measure the conical patterns depicted in Figures 51-61.

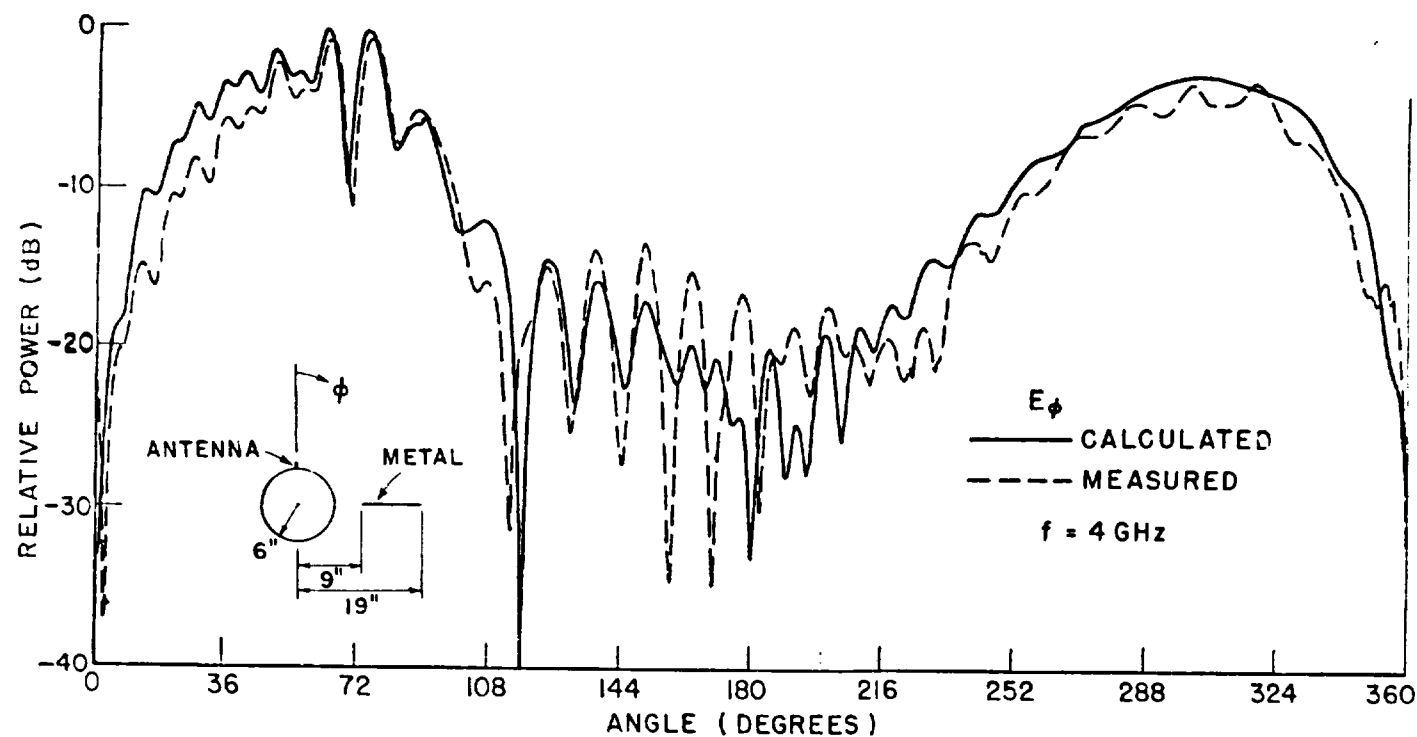


Figure 51. Roll plane ( $\theta_c = 0^\circ$ ,  $\phi_c = 0^\circ$ ,  $\theta = 90^\circ$ ) patterns for a 0.25" monopole mounted at  $\phi_s = 90^\circ$  on a  $2\lambda \times 4\lambda$  spheroid.

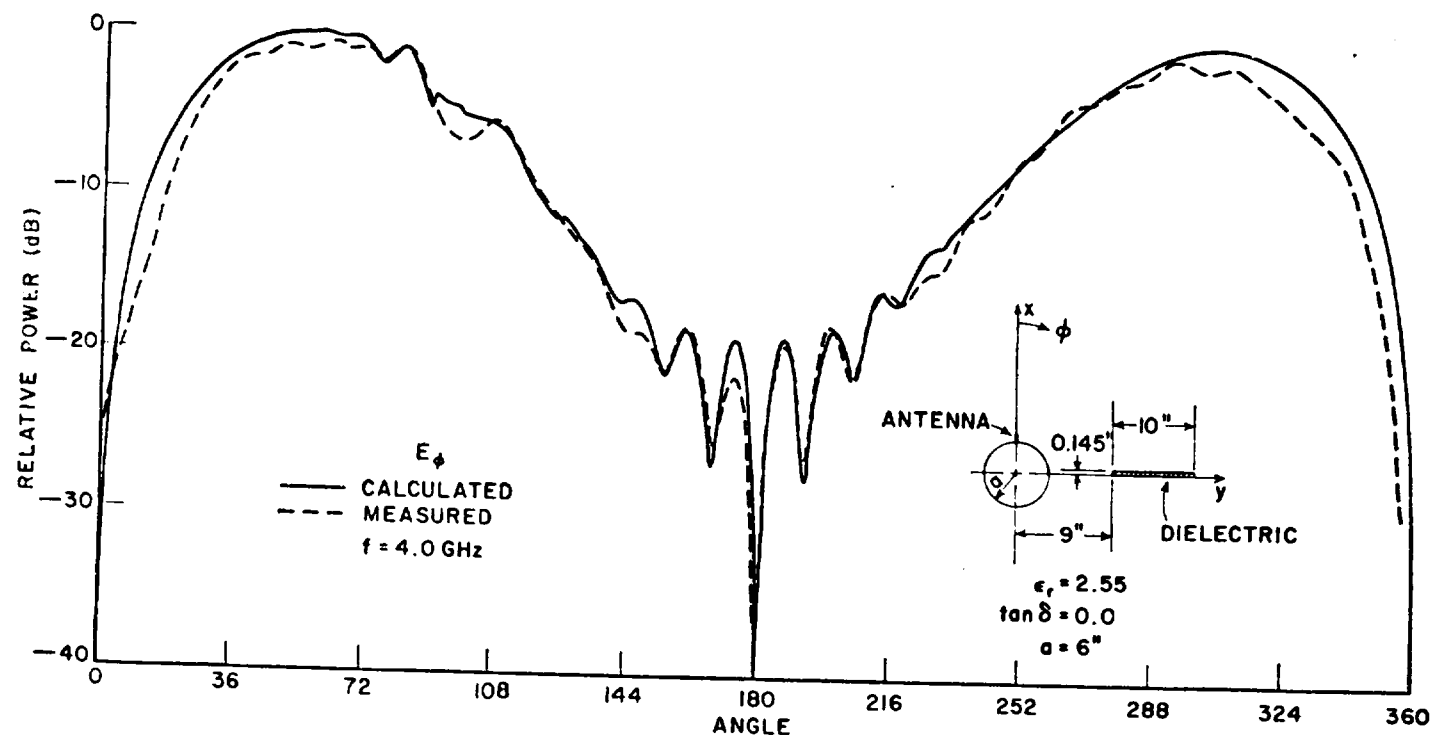


Figure 52. Roll plane ( $\theta_s = 0^\circ$ ,  $\phi_s = 0^\circ$ ,  $\theta = 90^\circ$ ) patterns for a 0.25" monopole mounted at  $\theta_s = 90^\circ$  on a  $2\lambda \times 4\lambda$  spheroid.

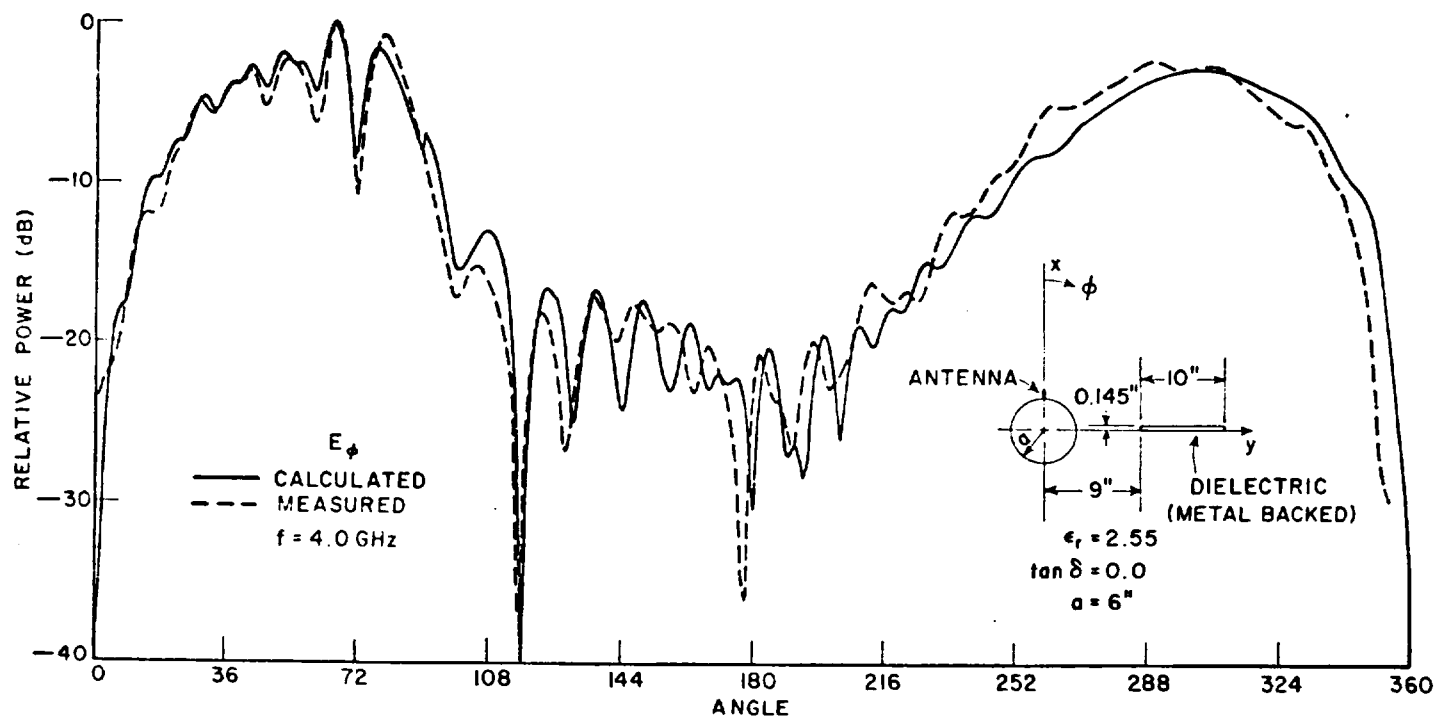


Figure 53. Roll plane ( $\theta_s = 0^\circ$ ,  $\phi_s = 0^\circ$ ,  $\theta = 90^\circ$ ) patterns for a 0.25" monopole mounted at  $\theta_s = 90^\circ$  on a  $2\lambda \times 4\lambda$  spheroid.

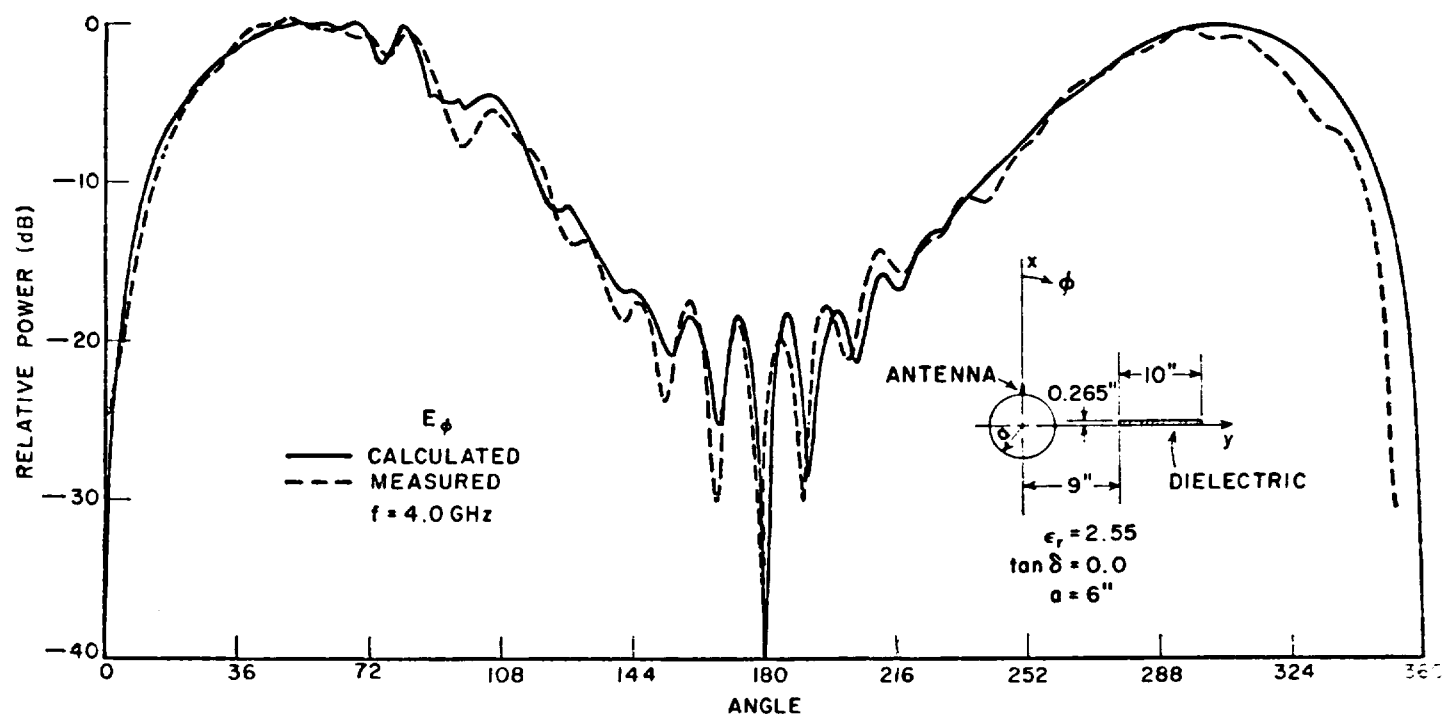


Figure 54. Roll plane ( $\theta_c = 0^\circ$ ,  $\phi_c = 0^\circ$ ,  $\theta = 90^\circ$ ) patterns for a 0.25" monopole mounted at  $\theta_s = 90^\circ$  on a  $2\lambda \times 4\lambda$  spheroid.

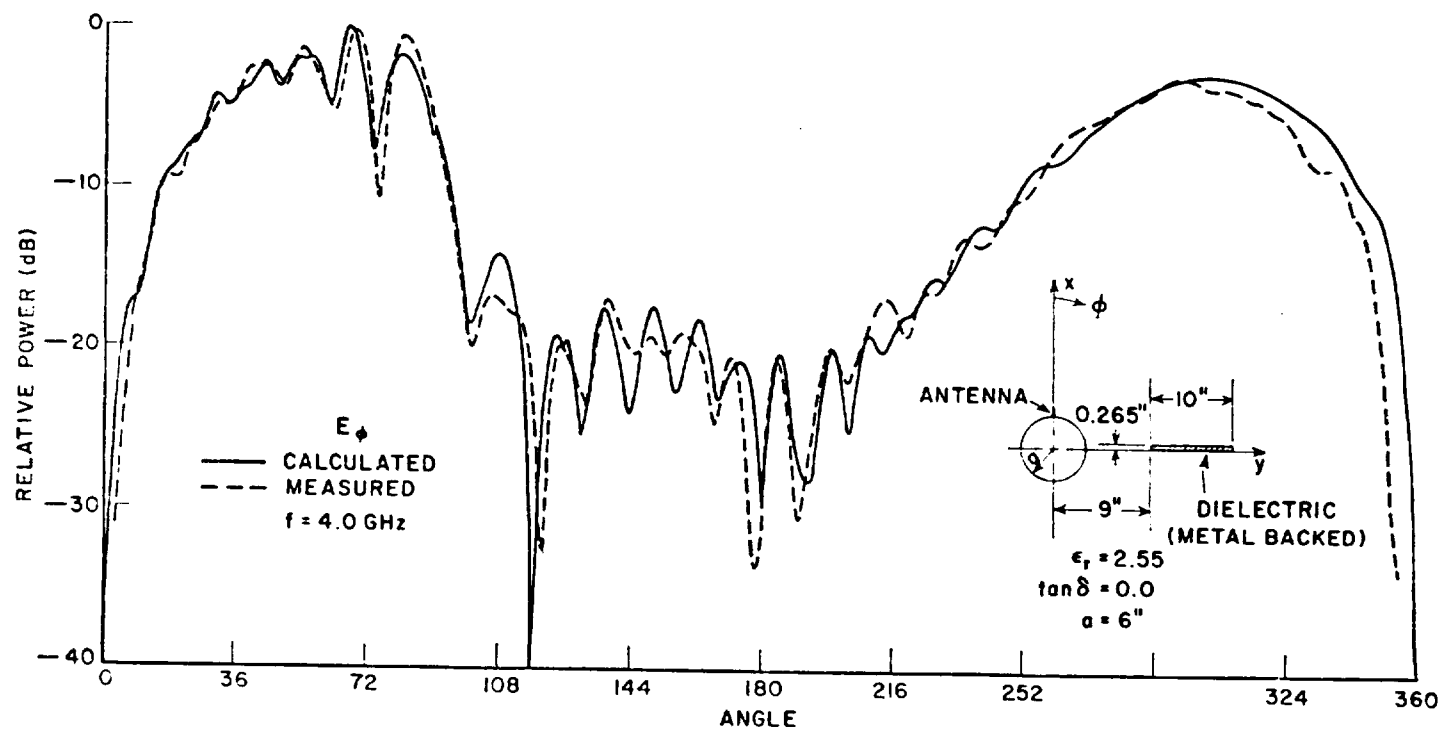


Figure 55. Roll plane ( $\theta_c = 0^\circ$ ,  $\phi_c = 0^\circ$ ,  $\theta = 90^\circ$ ) patterns for a 0.25" monopole mounted at  $\theta_s = 90^\circ$  on a  $C_{2\lambda} \times 4\lambda$  Spheroid.



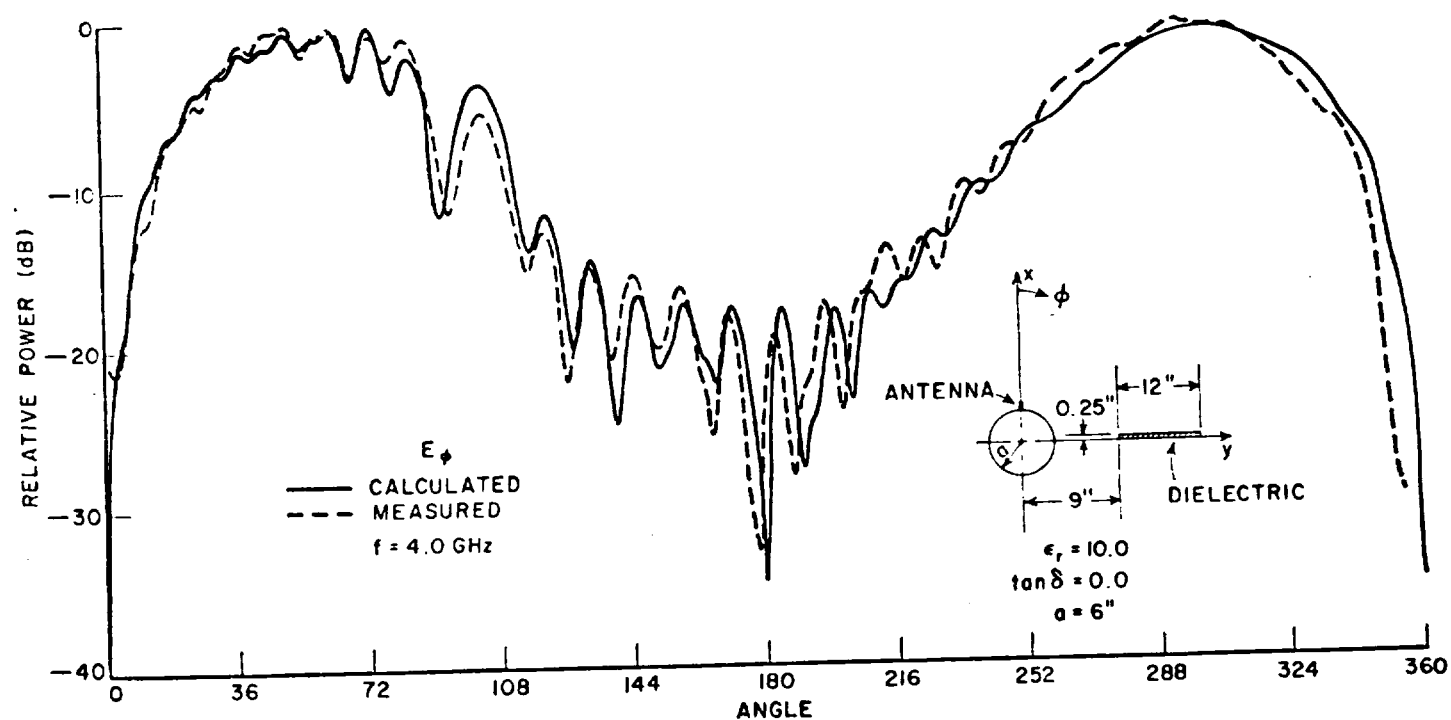


Figure 56. Roll plane ( $\theta_s = 0^\circ$ ,  $\phi_s = 0^\circ$ ,  $\theta = 90^\circ$ ) patterns for a 0.25" monopole mounted at  $\theta_s = 90^\circ$  on a  $2\lambda \times 4\lambda$  spheroid.

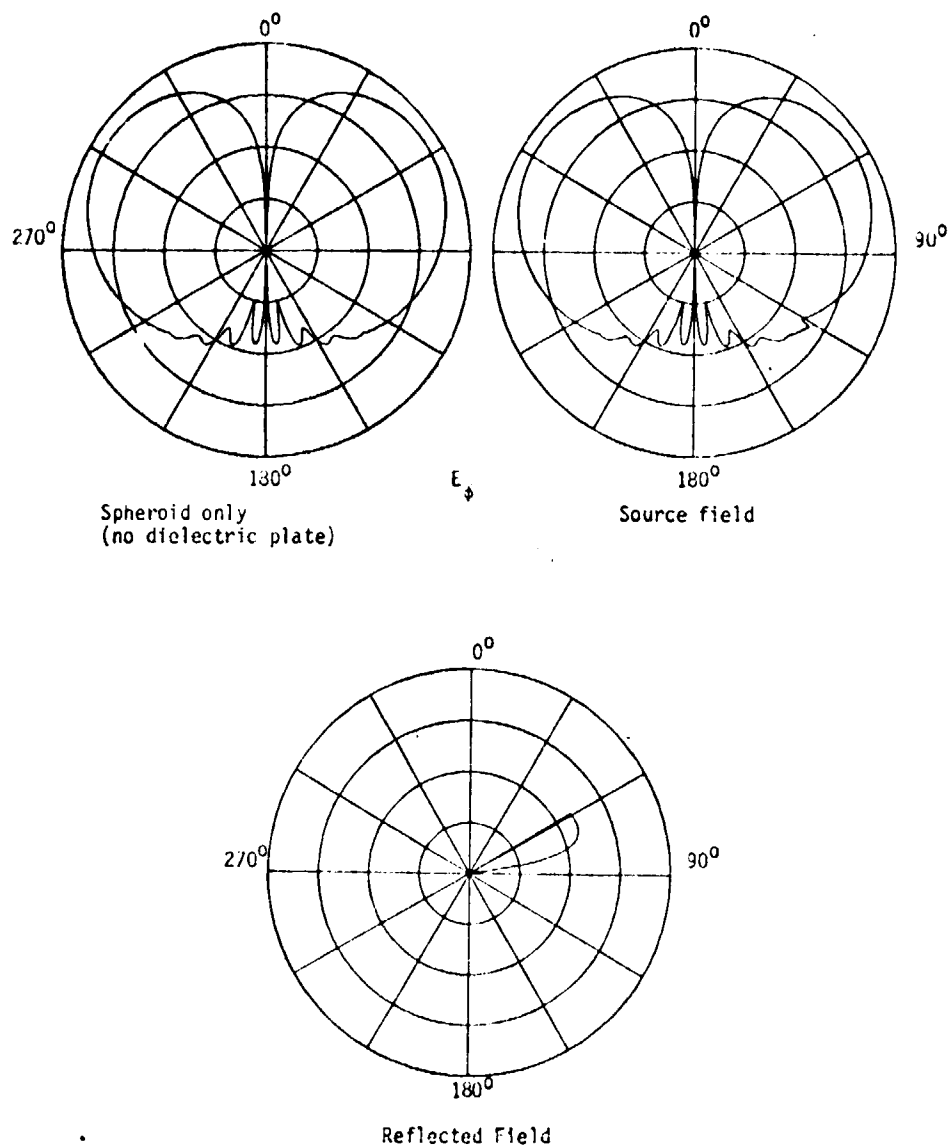


Figure 57. Calculated radiation patterns ( $\theta = 0^\circ$ ,  $\phi = 0^\circ$ ,  $\theta = 90^\circ$ ) for a 0.25" monopole mounted at  $\theta = 90^\circ$ . The dielectric slab is a 12" x 12" square of thickness  $d = 0.25$ ",  $\epsilon_r = 10$ ,  $\tan \delta = 0.0$  (See Figure 50)  $\rho_s = 36$ ".

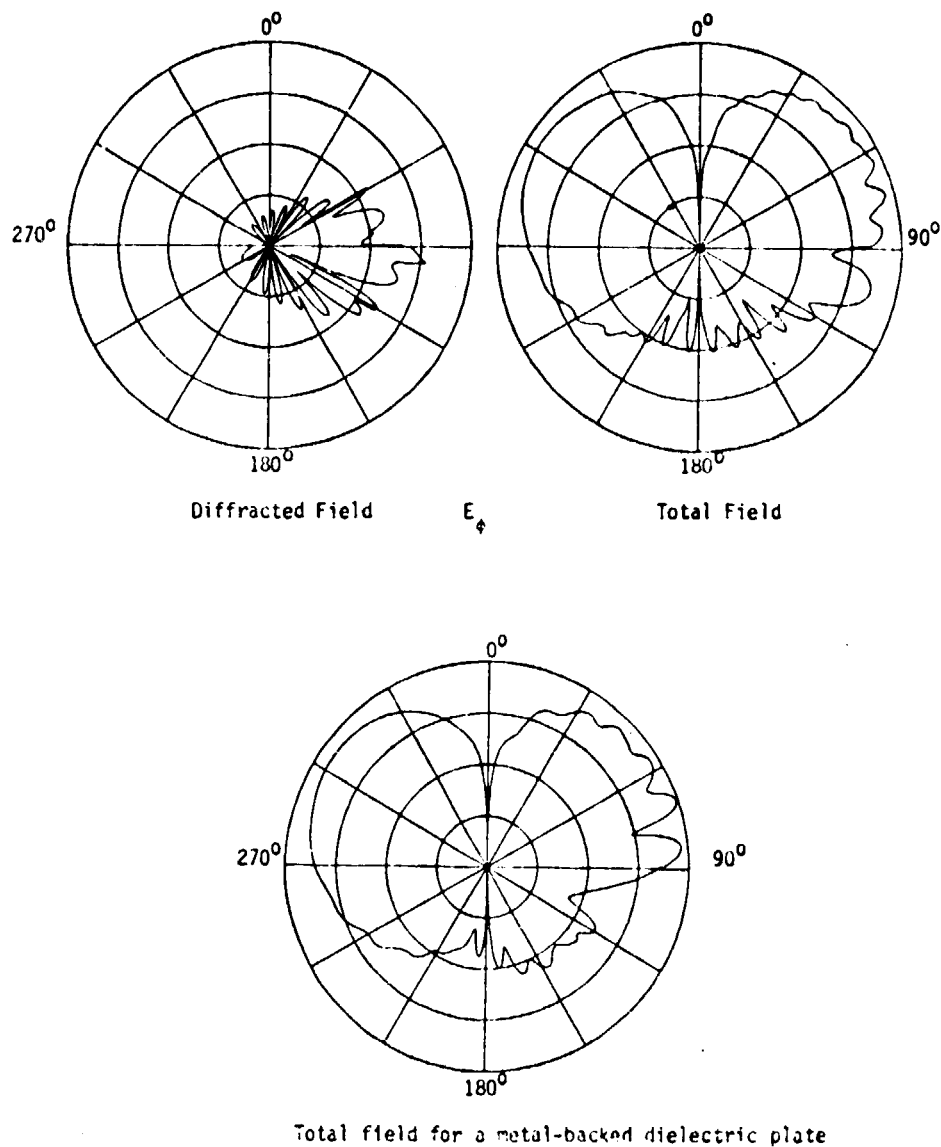


Figure 58. Calculated radiation patterns ( $\theta = 0^\circ$ ,  $\phi = 0^\circ$ ,  $\theta = 90^\circ$ ) for a 0.25" monopole mounted at  $\theta_s = 90^\circ$ . The dielectric slab is a 12" x 12" square of thickness  $d = 0.25$ ",  $\epsilon_r = 10$ ,  $\tan \delta = 0.0$  (See Figure 50)  $\rho_s = 36$ ".

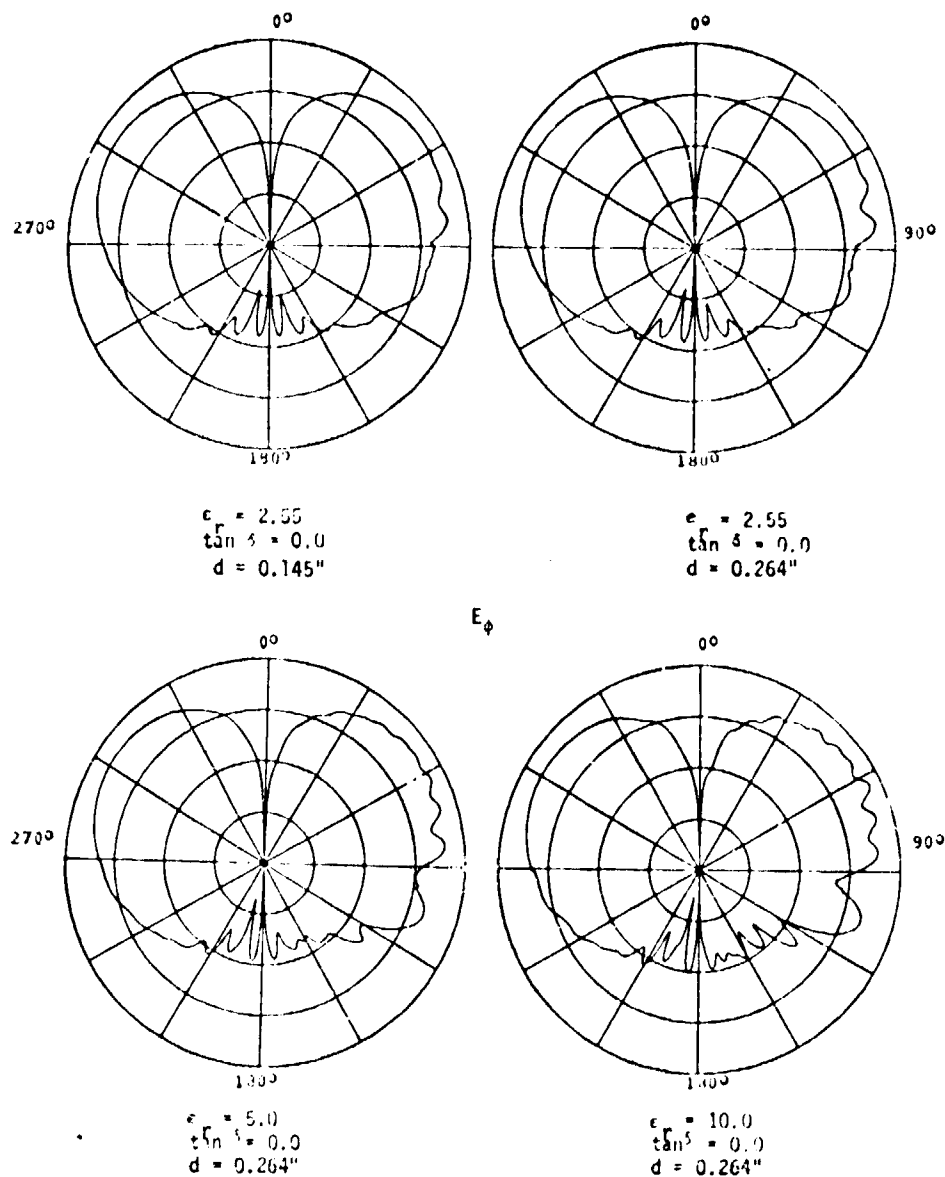


Figure 59. Calculated radiation patterns ( $\theta = 0^\circ$ ,  $\phi = 0^\circ$ ,  $\theta = 90^\circ$ ) for a 0.25" monopole mounted at  $h = 90^\circ$ . The dielectric plate is a 10" x 10" square. (See Figure 50)  $\rho_s = 36''$ .

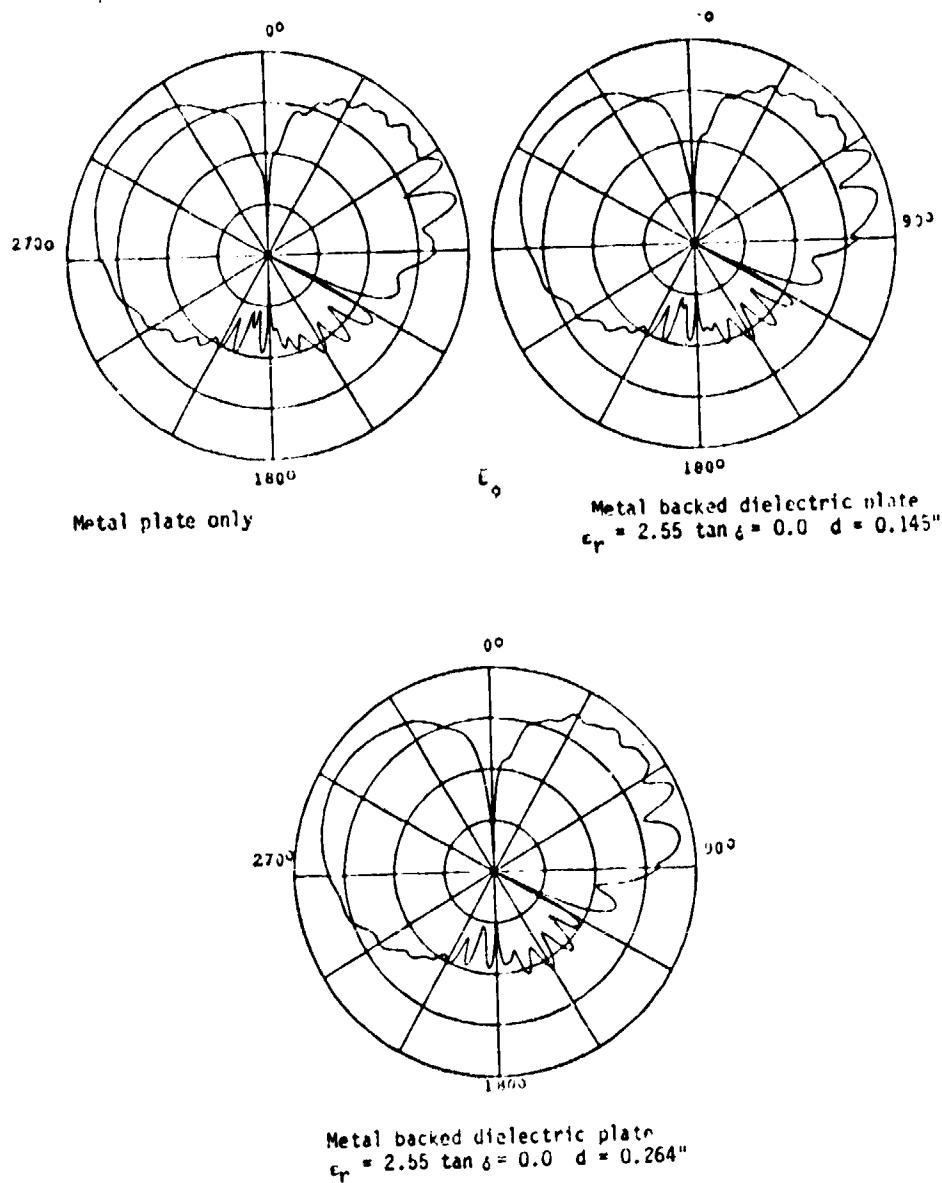
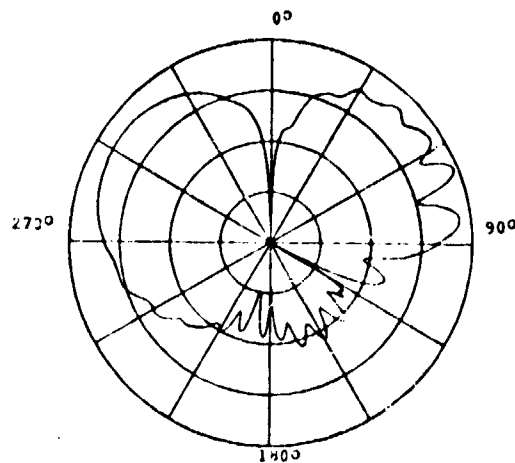
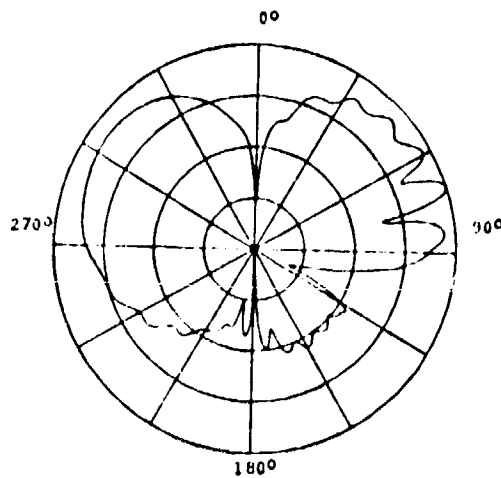


Figure 60. Calculated radiation patterns ( $\theta = 0^\circ$ ,  $\phi = 0^\circ$ ,  $\theta = 90^\circ$ ) for a 0.25" monopole mounted at  $h = 90^\circ$ . The plate (metal and/or dielectric) is a  $10^6 \times 10^6$  square. (See Figure 50)  $\rho_s = 36''$ .



Metal backed dielectric plate  
 $\epsilon_r = 5.0 \quad \tan \delta = 0.0$



Metal-backed dielectric plate  
 $\epsilon_r = 10., \tan \delta = 0.0.$

Figure 61. Calculated roll-plane ( $\theta_c = 0^\circ$ ,  $\phi_c = 0^\circ$ ,  $\theta = 90^\circ$ ) patterns for a 0.25" monopole mounted at  $\theta_c = 90^\circ$ . The plate is a 10" x 10" square of thickness  $d^S = 0.264$ " (See Figure 50)  $\mu_s = 36$ ".

## CHAPTER VIII

### SUMMARY AND CONCLUSIONS

The object of this thesis has been to calculate the high frequency radiation pattern of an antenna mounted on a arbitrary convex surface radiating in the presence of a dielectric or metal plate. The Geometrical Theory of Diffraction was applied and extended here to include diffraction by flat dielectric slabs. Chapter VI discussed a systematic way of obtaining the total high-frequency field by superimposing the individual source, reflected, transmitted, edge diffracted and when needed the corner diffracted fields.

The geometrical optics field, the reflection, and transmission coefficients for a lossy flat dielectric slab were discussed in Chapter II. The modified edge diffraction coefficients valid for wedges whose walls are lossy or lossless dielectric or perfectly-conducting plates were developed in Chapters III and IV. The interior angle of the wedge is assumed to be close to  $0^\circ$  or  $180^\circ$ . Otherwise, the diffraction coefficients are not valid. Although the present theory is valid for thin dielectric plates whose width cannot exceed a quarter of a wavelength in free space, it can be modified to treat the problem of diffraction by thick dielectric layers. It is possible to obtain diffraction coefficients for curved plates by adding two terms to the diffraction coefficients; however, the transmission and reflections coefficients would, also, have to be generalized to include curved slabs. Since expressions for surface diffracted rays are needed in the shadow region, Chapter V presented surface diffraction coefficients for an arbitrary convex surface.

The measured and calculated conical patterns for the two basic geometries presented in Chapter VII are seen to agree very well. An important property of GTD was demonstrated when the corner diffracted term was added to correct the discontinuity in the calculated pattern. That is, when a higher order term is important but not included in the final solution, a jump or kink will appear in the calculated pattern. Thus, one has a self-correcting mechanism by which one can gauge the impact of the missing terms and add higher order terms to the solution until a continuous pattern is obtained.

The most immediate application of the results presented here is in the modelling of structures such as aircraft which are composed of non-metallic parts that play a significant role in the radiation

pattern. As a result of this study, an existing computer code was modified which calculates the near-field radiation pattern of antennas mounted on an aircraft, which may have non-metallic parts. The electric dimensions of the spheroid used to model structures such as the fuselage of an aircraft or missile are much larger than the ones used here. Thus, more accurate results should be obtained due to the locality of the high-frequency diffraction phenomenon when the spheroid is larger in terms of wavelengths.



# REFERENCES

- [ 1 ] J.B. Keller, "The Geometric Optics Theory of Diffraction," presented at the 1953 McGill Symposium Microwave Optics, A.F. Cambridge Res. Center, Report TR-59-118 (II), pp. 207-210.
- [ 2 ] J.B. Keller, "A Geometrical Theory of Diffraction," in Calculus of Variations and its Applications, L.M. Graves, Ed., New York: McGraw-Hill, 1958, pp. 27-52.
- [ 3 ] J.B. Keller, "Geometrical Theory of Diffraction," J. Opt. Soc. Amer., Vol. 52, pp. 116-130, 1962.
- [ 4 ] R.G. Kouyoumjian, P.H. Pathak, and W.D. Burnside, "A Uniform GTD for the Diffraction by Edges, Vertices, and Convex Surfaces," Acoustic, Electromagnetic and Elastic Wave Scattering-Focus on the T-Matrix Approach, V.K. Varadan, V.V. Varadan, Eds., New York: Pergamon Press, 1980, pp. 373-397.
- [ 5 ] R.G. Kouyoumjian, "Asymptotic High Frequency Methods," Proc. IEEE, Vol. 53, pp. 864-876, August 1965.
- [ 6 ] R.G. Kouyoumjian, and P.H. Pathak, "A Uniform Geometrical Theory of Diffraction for an Edge in a Perfectly Conducting Surface," Proc. IEEE, Vol. 62, pp. 1448-1461, 1975.
- [ 7 ] G.A. Deschamps, "Ray Techniques in Electromagnetics," Proc. IEEE, Vol. 60, pp. 1022-1035, Sept. 1972.
- [ 8 ] R.G. Kouyoumjian, and P.H. Pathak, "The Dyadic Diffraction Coefficient for a Curved Edge," The Ohio State University ElectroScience Laboratory, Department of Electrical Engineering; prepared under Grant No. NGR36-008-144 for National Aeronautics and Space Administration, Annual Report 3001-3, August 1973.
- [ 9 ] P.H. Pathak, N. Wang, W.D. Burnside, and R.G. Kouyoumjian, "A Uniform GTD Solution for the Radiation from Sources on a Convex Surface," The Ohio State University ElectroScience Laboratory, Department of Electrical Engineering; prepared under Contract N00019-78-C-0524 for the Dept. of the Navy, Naval Air Systems Command, Report 71305, February 1980.
- [ 10 ] C.C. Huang, N. Wang, and W.D. Burnside, "The High Frequency Radiation Patterns of a Spheroid-Mounted Antenna," The Ohio State University ElectroScience Laboratory, Department of Electrical Engineering; prepared under Contract N00019-80-C-0050 for Naval Air Systems Command, Report 712527-1, March 1980.

- [11] K.W. Burgener, "High Frequency Scattering from a Thin Lossless Dielectric Slab," The Ohio State University ElectroScience Laboratory, Dept. of Electrical Engineering; prepared under Grant NSC-1498 for National Aeronautics and Space Administration, Langley Research Center, Thesis, 1979.
- [12] N. Wang, "Near Field Solutions for Antennas on Elliptic Cylinder," The Ohio State University ElectroScience Laboratory, Dept. of Electrical Engineering; prepared under Contract N00019-77-C-0299 for the Naval Air Systems Command, Report 784685-1, July 1977.
- [13] W.D. Burnside, N. Wang, and E.L. Pelton, "Near Field Pattern Computations for Airborne Antennas," IEEE Trans., Vol. AP-28, pp. 318-327, May 1980.
- [14] W.D. Burnside and P.H. Pathak, "A Corner Diffraction Coefficient," to be published.
- [15] E.L. Pelton, and W.D. Burnside, "Edge Diffraction Point Analysis used in Near-Field On-Aircraft Antenna Studies," The Ohio State University ElectroScience Laboratory, Dept. of Electrical Engineering; prepared under Contract N00019-77-C-0299 for the Naval Air Systems Command, Report 784685-2, October 1977.